

EFFECTS OF HEAT INPUT AND THERMAL CYCLES TO THE FRACTURE  
TOUGHNESS OF API 5L GRADE X70M STEEL WELDED BY GAS METAL  
ARC WELDING

A THESIS SUBMITTED TO  
THE GRADUATE SCHOOL OF NATURAL AND APPLIED SCIENCES  
OF  
MIDDLE EAST TECHNICAL UNIVERSITY

BY

EREN EROL

IN PARTIAL FULFILLMENT OF THE REQUIREMENTS  
FOR  
THE DEGREE OF MASTER OF SCIENCE  
IN  
METALLURGICAL AND MATERIALS ENGINEERING

DECEMBER 2019



Approval of the thesis:

**EFFECTS OF HEAT INPUT AND THERMAL CYCLES TO THE  
FRACTURE TOUGHNESS OF API 5L GRADE X70M STEEL WELDED BY  
GAS METAL ARC WELDING**

submitted by **EREN EROL** in partial fulfillment of the requirements for the degree  
of **Master of Science in Metallurgical and Materials Engineering Department,**  
**Middle East Technical University** by,

Prof. Dr. Halil Kalıpçılar  
Dean, Graduate School of **Natural and Applied Sciences**

\_\_\_\_\_

Prof. Dr. C. Hakan Gür  
Head of Department, **Met. and Mat. Eng.**

\_\_\_\_\_

Prof. Dr. C. Hakan Gür  
Supervisor, **Met. and Mat. Eng., METU**

\_\_\_\_\_

Dr. Koray Yurtışık  
Co-Supervisor, **Weld. Tech. and NDT Res./App. C., METU**

\_\_\_\_\_

**Examining Committee Members:**

Prof. Dr. Bilgehan Ögel  
Met. and Mat. Eng., METU

\_\_\_\_\_

Prof. Dr. C. Hakan Gür  
Met. and Mat. Eng., METU

\_\_\_\_\_

Prof. Dr. Cevdet Kaynak  
Met. and Mat. Eng., METU

\_\_\_\_\_

Prof. Dr. Rıza Gürbüz  
Met. and Mat. Eng., METU

\_\_\_\_\_

Assist. Prof. Dr. Kemal Davut  
Met. and Mat. Eng., Atılım University

\_\_\_\_\_

Date: 09.12.2019

**I hereby declare that all information in this document has been obtained and presented in accordance with academic rules and ethical conduct. I also declare that, as required by these rules and conduct, I have fully cited and referenced all material and results that are not original to this work.**

Name, Surname: Eren Erol

Signature:

## **ABSTRACT**

### **EFFECTS OF HEAT INPUT AND THERMAL CYCLES TO THE FRACTURE TOUGHNESS OF API 5L GRADE X70M STEEL WELDED BY GAS METAL ARC WELDING**

Erol, Eren

Master of Science, Metallurgical and Materials Engineering

Supervisor: Prof. Dr. C. Hakan Gür

Co-Supervisor: Dr. Koray Yurtışık

December 2019, 112 pages

High strength low alloy steels are widely used in line pipe applications since they have reasonably high strength and toughness due to their micro-alloying elements and production via thermomechanically controlled process. During welding of these steels, microstructures of the fusion zone and the heat affected zone consisting globular and acicular ferrite alter due to induced heat and thermal cycles. Consequently, changes in the microstructure affects the mechanical properties such as fracture toughness. Gas metal arc welding used in line pipe applications has several advantages such as high quality welds in short time, simplicity, no extra flux is needed, and no slag. The primary aim of this work to understand the effects of heat input and number of thermal cycles in gas metal arc welding on the fracture toughness of API 5L X70M steel. Effects of heat input and thermal cycles originating from weld passes on formation of local brittle zones and effect of local brittle zones on general fracture mechanism were investigated. Particular emphasis has been placed on the coarse grained heat affected zone.

Keywords: Gas Metal Arc Welding, Heat Input, High Strength Low Alloy Steel,  
Microstructure, Crack Tip Opening Displacement

## ÖZ

### **ISI GİRDİSİ VE ISIL DÖNGÜLERİN GAZ ALTI KAYNAK YÖNTEMİ İLE KAYNAKLANMIŞ API 5L X70M ÇELİĞİNİN KIRILMA TOKLUĞUNA ETKİSİ**

Erol, Eren

Yüksek Lisans, Metalurji ve Malzeme Mühendisliği

Tez Danışmanı: Prof. Dr. C. Hakan Gür

Ortak Tez Danışmanı: Dr. Öğr. Üyesi Koray Yurtışık

Aralık 2019, 112 sayfa

Yüksek dayançlı düşük alaşımlı çelikler, içerdikleri mikro alaşım elementleri ve termomekanik haddeme üretim metodunun sonucu olarak oldukça iyi mukavemet ve tokluğa sahiptir. Mekanik özelliklerindeki avantajlar nedeniyle boru hatlarında kullanımları oldukça fazladır. Boruların kaynaklanması sırasında ısı girdisi ve ısı döngüleri etkisiyle malzemede oluşan ergime bölgesinin ve ısıdan etkilenen bölgenin mikroyapıları değişmekte ve bu durum malzemenin kırılma tokluğu gibi birçok özelliğini etkilemektedir. Gazaltı kaynak yöntemi kısa zamanda nispeten kaliteli bir kaynak elde edilmesi, basit olması ve bir cüruf oluşturucuya ve cüruf temizlemeye ihtiyaç olmaması gibi avantajlara sahiptir. Bu çalışmada kaynaklanmış API 5L X70M boru hattı çeliklerinin kırılma tokluğu davranışı incelenmiştir. Uygulanan kaynak pası sayısına dayanan ısı girdisi ve ısı döngülerinin yerel gevrek bölge oluşumuna ve kırılma davranışı üzerine etkileri araştırılmıştır. Çalışmalarda özellikle iri taneli ısıdan etkilenen bölgeye odaklanılmıştır.

Anahtar Kelimeler: Gaz Metal Ark Kaynağı, Isı Girdisi, Yüksek Dayançlı Düşük Alaşımlı Çelik, İçyapı, Çatlak Ucu Açılım Deplasmanı Deneyi



in memory of my dearest uncle who passed away from this world all too soon

## ACKNOWLEDGEMENTS

I sincerely thank my supervisor Prof. Dr. C. Hakan Gür and co supervisor Dr. Koray Yurtışık for their guidance, advice, criticism, encouragements and insight throughout the research

I deeply appreciate Dr. Süha Tirkeş for his motivation, guidance and support.

I sincerely appreciate M. Tolga Ertürk, Burcu Anık and Uygur Tosun whose help and advices were invaluable.

I would like to thank my friend Mehmet Çağırıcı for his support from overseas throughout this work.

Baran Tunç, Kaan Uslu, Alper Topbaş, Yağmur Akbulut, Orhan Aydın, Arif Atalay Özdemir, Cemal Yanardağ, Yücel Ateş, Mevlüt Bağcı and Serkan Bilgi were very supportive and altruistic during fabrication and testing processes.

Additionally I would like to thank my friends Baybora Tunahan Matur, Nil Akdede, Yunuscan Oktav, İbrahim İyce, Pınar Tuncer, Sercan Yegin, Erkin Barış Güngör, Bekir Gürel Dimez, Erdi Kandemir, İpek Kandemir, Ali Emre Tanrısevdi, Mine Tanrısevdi, Oğuz Peker, İsmet Morkoç, Hakan Ersan, Cem Zeyrek and Mert Paçacıoğlu for all their support and entertainment.

I would like to thank Turkish Aerospace and my colleagues for their support and understanding.

I want to extend my deep appreciation to my family; my mother Pembe Erol, my father İrfan Erol and my sister Selin Erol for their infinite support, their faith in me, to all my friends and to whomever eased the load on me walking this path.

Lastly, I want to express my great gratitude to my love Ulaş Can for her understanding, endless support and unconditional love. Without her companion, patience and help I would not have succeeded.

## TABLE OF CONTENTS

ABSTRACT .....	v
ÖZ .....	vii
ACKNOWLEDGEMENTS .....	x
TABLE OF CONTENTS .....	xi
LIST OF TABLES .....	xiii
LIST OF FIGURES .....	xiv
LIST OF ABBREVIATIONS .....	xviii
LIST OF SYMBOLS .....	xxi
CHAPTERS .....	1
1. INTRODUCTION .....	1
1.1. Motivation .....	1
1.2. Scope .....	3
2. THEORY .....	5
2.1. General.....	5
2.2. Parent Material .....	5
2.3. Girth Welding of Line Pipes.....	15
2.4. Welding Metallurgy of HSLA steels .....	26
2.5. Fitness-for-Service .....	35
2.6. Fracture Mechanics.....	36
3. EXPERIMENTAL.....	41
3.1. Parent and Filler Metals.....	41
3.2. Welding Procedures.....	42

3.3. Elemental Analysis.....	46
3.4. Confirming the Integrity of Weldment .....	47
3.5. Microstructural Characterization .....	48
3.6. Mechanical Characterization.....	53
3.7. Post-Test Metallography and Fractography .....	57
3.8. $\delta$ (CTOD) Parameter Calculations .....	59
4. RESULTS AND DISCUSSION .....	63
4.1. Parent and Filler Metal Characteristics .....	66
4.2. The Microstructure of HAZ .....	69
4.3. The Local Brittle Zones .....	87
4.4. M-A Formation .....	91
4.5. Fracture Toughness of CGHAZ.....	96
4.6. Effect of M-A Constituents on the Crack Extension Resistance .....	98
5. CONCLUSIONS .....	103
REFERENCES .....	105

## LIST OF TABLES

Table 2.1. Mechanical properties of API 5L X70M grade pipeline steels [2] .....	7
Table 2.2. Chemical composition limitations of API 5L X70M grade pipeline [2] ....	7
Table 2.3. Alloying elements frequently used in HSLA steels [4] .....	9
Table 2.4. Tensile Properties and Impact Absorbed Energies of Different Microstructured API X70 Steels [9] .....	14
Table 2.5. Arc welding methods .....	17
Table 2.6. Efficiencies of different welding techniques [16].....	26
Table 3.1. Welding parameters for the high heat input.....	45
Table 3.2. Welding parameters for the low heat input.....	45
Table 3.3. Welding parameters simulating the heat input of 1.4 kJ/mm .....	46
Table 3.4. Welding parameters simulating the heat input of 1.15 kJ/mm .....	46
Table 3.5. Welding parameters simulating the heat input of 0.65 kJ/mm .....	46
Table 3.6. $g_1 \left( \frac{a_0}{W} \right)$ values for three-point bend specimens .....	60
Table 4.1. API 5L X70M composition.....	66
Table 4.2. Filler material composition .....	66
Table 4.3. Tensile test results of base material and weldments .....	68
Table 4.4. Primary austenite grain sizes (PAGS) in CGHAZ region of welds having different heat inputs.....	75
Table 4.5. Cooling rates with respect to weld heat input (obtained from bead-on plate studies' temperature measurements) .....	77
Table 4.6. Heat input and cooling rates in literature .....	77
Table 4.7. Minimum Single $\delta$ (CTOD) values.....	96

## LIST OF FIGURES

Figure 2.1. Schematic representation of rolling schedules of traditional rolling and normalizing (upper) and thermomechanical processing (lower) [5] .....	11
Figure 2.2. Light Optical Microscopy (LOM) micrograph of the API X70M steel. (AF: acicular ferrite, PF: polygonal ferrite, P: pearlite). 1500X [8] .....	12
Figure 2.3. Scanning Electron Microscope (SEM) micrograph of the base metal. (AF: acicular ferrite, PF: polygonal ferrite). [8].....	13
Figure 2.4. SEM Micrographs of API X70 Steel produced with Different Rolling Process Routes. (a) Steel A, (b) Steel B, (c) Steel C, (d) Steel D [9] .....	14
Figure 2.5. Temperature distribution in a welding process [11].....	16
Figure 2.6. Schematic representation of SMAW technique[12].....	18
Figure 2.7. Gas–metal arc welding: (a) overall process; (b) welding area enlarged [13] .....	19
Figure 2.8. Metal transfer during GMAW of steel with Ar–2% O <sub>2</sub> shielding: (a) globular transfer at 180A and 29V shown at every $3 \times 10^{-3}$ s; (b) spray transfer at 320A and 29V shown at every $2.5 \times 10^{-4}$ s. Reprinted from Jones et al.[15]. Courtesy of American Welding Society.....	21
Figure 2.9. Schematic view of flux-cored arc welding (FCAW) (a) overall process (b) welding area enlarged .....	22
Figure 2.10. Different polarities in GTAW (a) DCEN (b) DCEP (c) AC [13] .....	24
Figure 2.11. Typical microstructural features of a single pass welding [17] .....	27
Figure 2.12. HAZ microstructure variations in single and multi-pass welding [18].	28
Figure 2.13. Representation of four proposed initiation mechanisms[25] .....	31
Figure 2.14. Nucleation of a crystal from a liquid on a planar substrate [13] .....	33
Figure 2.15. Fusion boundary microstructures a) Type 409/Monel base and weld metals b) 1080/Monel base and weld metals [27] .....	34
Figure 2.16. Yielding conditions based on LEFM and EPFM [30].....	37
Figure 3.1. DBTT behavior of base metal API 5L X70M [8] .....	42

Figure 3.2. CRC- Evans P-625 Computerized welding machine [37].....	43
Figure 3.3. Welding robot setup for the GMAW and HPAW technique used in the thesis.....	44
Figure 3.3. Schematic representation of hardness indentations [39] .....	49
Figure 3.4. A representative load displacement curve of a nano-indentation process [48].....	51
Figure 3.5. Berkovich nano-indenter trace after nano-indentation [49].....	52
Figure 3.6. Nano indentations on specimen and load-indentation depth diagram [36] .....	52
Figure 3.7. Crack plane orientation for fracture toughness specimens for weld metal [51].....	54
Figure 3.8. Integral knife-edged notch geometry.....	55
Figure 3.9. Three-point bending test setup [52].....	56
Figure 3.10. Experimental set-up for fracture toughness test .....	57
Figure 3.11. Schematic view of the specimen surface and measurements of crack lengths on specimens [51].....	58
Figure 3.12. Different types of Force vs CMOD recordings [52].....	59
Figure 3.13. Definition of $V_p$ (for determination of $\delta$ ) [52] .....	61
Figure 4.1. Radiographic inspection of welded joints .....	63
Figure 4.2. Macrograph of the weldment (1.1kJ/mm heat input) .....	65
Figure 4.3. Macrograph of the weldment (0.65 kJ/mm heat input) .....	65
Figure 4.4. Macrograph of the weldment (1.4 kJ/mm heat input) .....	65
Figure 4.5. Banded structure of the base metal (2% Nital etched) .....	67
Figure 4.7. An overview to different zones formed during one pass welding .....	71
Figure 4.7. The HAZ regions of a welded joint, corresponding temperature ranges and relevant parts of Fe-C phase diagram.....	72
Figure 4.8. Different weld zone micrographs of 1.4kJ/mm heat input weld in 1000x magnification (etched by 2% nital) (a) Coarse grained heat affected zone (CGHAZ) (b) Fine grained heat affected zone (FGHAZ) (c) Intercritical heat affected zone (ICHAZ) (d) Tempered zone (TZ).....	73

Figure 4.10. Cooling curves of different regions of weld obtained with thermocouples (TC) (a) CGHAZ region of one-pass weld (TC 0.2 mm away from FL) (b) FGHAZ region of one-pass weld (TC 1.2 mm away from FL) (c) ICHAZ region of one-pass weld (TC 1.7 mm away from FL).....	74
Figure 4.10. Effect of heat input on cooling rate [61] .....	76
Figure 4.12. Continuous cooling transformation (CCT) diagram of weld having 1.4 kJ/mm heat input.....	78
Figure 4.13. Continuous cooling transformation (CCT) diagram of weld having 1.1 kJ/mm heat input.....	79
Figure 4.14. Continuous cooling transformation (CCT) diagram of weld having 0.65 kJ/mm heat input.....	79
Figure 4.15. An SEM micrograph of CGHAZ .....	80
Figure 4.15. Additional CGHAZ regions formed in multi-pass welding [71] .....	82
Figure 4.16. Hardness variations in multi-pass welding [73].....	83
Figure 4.17. HV0.5 hardness contour map of weld having 0.65kJ/mm heat input ...	84
Figure 4.18. HV0.5 hardness contour map of weld having 1.1 kJ/mm heat input ....	84
Figure 4.19. HV0.5 hardness contour map of weld having 1.4 kJ/mm heat input ....	85
Figure 4.20. Micrograph of the CGHAZ region of 1.4 kJ/mm weldment (etched by LePera, 1000x).....	89
Figure 4.21. Micrograph of the IRCGHAZ region of 1.1 kJ/mm weldment (etched by LePera, 1000x).....	89
Figure 4.22. Micrograph of the IRCGHAZ region of 0.65 kJ/mm weldment (etched by LePera).....	90
Figure 4.23. Nano indentation hardness distribution.....	91
Figure 4.24. (a) The lattice correspondence for formation of martensite from austenite (b) Tetragonal unit cell outlined in austenite (c) Lattice deformation of formation of martensite with an appropriate c/a ratio [84] .....	91
Figure 4.25. TEM micrographs of the M-A constituent in the IR CGHAZ. (a, c) bright field and (b, d) dark field micrographs [19] .....	92
Figure 4.26. Relationship between number of weld passes and residual strain [94].	95

Figure 4.27. Force vs. CMOD graph of the specimens.....	96
Figure 4.28. Representative fracture surfaces of CTOD tests of .....	97
Figure 4.29. Fracture surface of the CTOD specimen (1.15 kJ/mm weldment).....	100
Figure 4.30. Plateau metallography micrograph of the CTOD specimen (1.15 kJ/mm weldment).....	100
Figure 4.31. Fracture surface of the CTOD specimen (0.65 kJ/mm weldment).....	101

## LIST OF ABBREVIATIONS

API	American Petroleum Institute
ASME	The American Society of Mechanical Engineers
ASTM	American Society for Testing and Materials
AWS	American Welding Society
BCC	Body Centered Cubic (lattice structure)
CCT	Continuous Cooling Transformation (diagram)
CE	Carbon Equivalent
CGHAZ	Coarse Grained Heat Affected Zone
CN	Carbonitride
CTOD	Crack Tip Opening Displacement
DIN	Deutsches Institut für Normung
ECA	Engineering Critical Assessment
EDS	Energy Dispersive Spectral Analysis
EPFM	Elastic Plastic Fracture Mechanics
FCAW	Flux Cored Arc Welding
FCG	Fatigue Crack Growth
FCC	Face Centred Cubic (lattice structure)
FGHAZ	Fine Grained Heat Affected Zone
FZ	Fusion Zone (weld metal)
GMAW	Gas Metal Arc Welding
GTAW	Gas Tungsten Arc Welding

HAZ	Heat Affected Zone
HI	Heat Input
HPAW	Hybrid Plasma-Gas Metal Arc Welding
HSLA	High Strength Low Alloy Steel
HV	Vickers Hardness
HVIT	Vickers Hardness Indentation Toughness
IIW	International Institute of Welding
IRCGHAZ	Intercritically Reheated Coarse Grain Heat Affected Zone
ISO	International Organization for Standardization
LBZ	Local Brittle Zone
LEFM	Linear Elastic Fracture Mechanics
LWS	Linear Welding Speed
MAG	Metal Active Gas Welding
MIG	Metal Inert Gas Welding
PAG	Prior Austenite Grain
PAW	Plasma Arc Welding
SEM	Scanning Electron Microscope
SCCGHAZ	Sub-critically reheated coarse-grain
SCHAZ	Sub-critical heat affected zone
SCRCGHAZ	Super-critically reheated coarse-grain heat affected zone
SCRFGHAZ	Super-critically reheated fine-grain heat affected zone
TANAP	Trans Anatolian Natural Gas Pipeline

TMCP	Thermomechanically Controlled Processes
TIG	Tungsten Inert Gas Welding
TTT	Time-temperature Transformation (diagram)
TZ	Tempered Zone
UTS	Ultimate Tensile Strength
V	Volts
WFS	Wire Feeding Speed

## LIST OF SYMBOLS

A	Elongation
AF	Acicular Ferrite
$\gamma$	Austenite
$\gamma_{LC}$	Surface Energy
$\delta$	CTOD Value
GB	Granular Bainite
$\Delta H_m$	Latent Heat of Melting
MA	Martensite-austenite islands
PF	Polygonal Ferrite
$R_{p0.2}$	0.2% offset yield stress (proof stress)
$R_m$	Ultimate tensile strength



# CHAPTER 1

## INTRODUCTION

### 1.1. Motivation

Energy is essential and has a great importance for human well-being. It is a key factor for national economies and it is important to establish dominance on energy resources since it is indispensable for industry and daily life. Clean and renewable energy demand increases more and more. Despite the fact that there are many researches and developments in renewable energy sources, it is inevitable to use fossil fuels. The transportation of these fossil fuels is advancing and getting easier with understanding the materials and the techniques used in manufacturing and developments in equipment. When economy and safety concerns are taken into account, pipelines are the best way for fossil fuel transportation.

The construction of the pipelines requires the joining of the line pipes with girth welding, i.e. circumferential welding. Seamless or spiral and line welded pipes can be used and different welding methods can be employed. The construction of the pipelines needs engineering of welding and it is a meticulous process. During structural integrity assessments of pipelines, welding joints deserve a special concern due to non-uniform nature of the process. A strong mismatch exists between the base metal, weld metal and the fusion zone. Strength and the fracture toughness parameters of the joints give the necessary data for engineering critical assessment (ECA), a method of structural integrity assessment.

Welding process is a rate limiting step in construction of pipelines. Introducing the obtained testing data to ECA shows that the tolerable flaw sizes are larger than the flaw size criteria coming from conventional workmanship. Consequently, quite low repair rates and quite high production rates have been achieved.

Trans-Anatolian Natural Gas Pipeline Project (TANAP) which launched in mid-2018 delivers natural gas developed from Azerbaijan Shah Deniz-2 Stage to Turkey and Europe. With its 1850 km of length, TANAP is one of the biggest pipeline projects which constructed under one management agent. Welding Technology and Non-destructive Testing Research / Application Center in Middle East Technical University has contributed to this project in terms of mechanical and microstructural characterization of pre-construction and construction weldments significantly. For instance fracture toughness determination tests have been conducted on more than 1300 SENB and SENT specimens. Conventional mechanical tests such as hardness, tensile and Charpy impact toughness tests have conducted as well.

Combining fracture mechanics analyses with microstructural evaluations is a challenging task. Since the inter-critically reheated coarse grain heat affected zone (IRCGHAZ) in an as-welded high strength low alloy (HSLA) steel presents the worst behavior in terms of toughness, microstructural alteration during welding thermal cycles and consequent effects on toughness is very critical.

## 1.2. Scope

Micro-alloyed or HSLA steel API 5L X70M one of the most widely used steels in pipeline applications, such as TANAP. It has relatively high properties and it is more favorable than other high strength low alloy steels such as X80 and X90 when the production costs are taken into account. The steel's superior properties come from its constituents, in very small amounts micro-alloying elements, and fabrication method, thermomechanically controlled processing. The micro-alloying elements favors acicular and polygonal ferrite formation and yield higher toughness values compared with carbon steels. By using proper welding techniques and procedures, deteriorating effects of welding on mechanical properties and microstructure are tried to be minimized.

Heating and cooling sequences, namely thermal cycles, during multi-pass welding, form different regions in base metal and fusion zone. In intercritically reheated coarse grained heat affected zone (IRCGHAZ), formed after reheating the coarse grained heat affected zone (CGHAZ) to austenite/ferrite two phase region by a following thermal cycle, destructive effects of welding can be seen clearly. IRCGHAZ has lower toughness than CGHAZ and it is very suspicious in terms of local brittle zones (LBZs).

In the scope of this thesis, LBZs, martensite-austenite (M-A) constituents including high carbon content and retained austenite, which decrease the toughness of the HAZ significantly and gives the lowest toughness values were examined. M-A formation which are correlated with prior austenite grains (PAG) and PAG size, M-A transformation and its Carbon content, formation types, and the size of M-A constituents was studied in HSLA steel API 5L X70M with respect to weld heat input and cooling rates with the aid of fracture toughness parameter, CTOD ( $\delta$ ), with single edge notched bend specimens.



## **CHAPTER 2**

### **THEORY**

#### **2.1. General**

This is composed of five sections. First, the properties of API 5L X70M steel, its properties and its manufacturing method are given. Secondly, a brief information about girth welding of line pipes is given. Thirdly, welding metallurgy of HSLA steel is described in detail. Fourthly, fitness-for-service analysis of line pipe is discussed briefly. Lastly, the main concern of this thesis, fracture mechanics is described in detail in accordance with the current welding codes and standards and in historical perspective as well.

#### **2.2. Parent Material**

Pipelines are the most common and widely used transfer method for the fossil energy sources. Different line pipe materials are produced in diverse methods and according to different standards such as API, ASME and ISO. In steel pipe industry, API standards are the most commonly used one and API specification 5L [API 5L] which specifies the requirements for production of seamless and welded steel pipes for use in oil and gas industries is the most popular one in this industry. This specification has a wide range of line pipe steel grades with two different kind of product specification level (PSL), namely PSL-1 and PSL-2.

PSL-1 and PSL-2 pipes are differ mainly in terms of chemical properties, mechanical properties and delivery condition. PSL-1 limits the C, S, P contents of the steels

differently with respect to the grades while PSL-2 gives maximum values of these elements same in every grade. For PSL-1 steels, it is sufficient to meet minimum requirements whereas PSL-2 limits the yield and ultimate tensile strength of the pipes. Furthermore, PSL-1 pipes can be delivered with belled-end, threaded-end and plain-end however PSL-2 pipes can only be delivered with plain-end condition.

The steel grades in PSL 1 are designated by letters or alphanumeric characters, the steel grade is the same with the pipe grade and designation, which associated with steel's chemical composition, indicates the strength level of the steel. In addition to these PSL 2 pipes designation includes a single letter suffix depends on the delivery condition. The digits following the L and M letters indicates the specified minimum yield strength in MPa and ksi -which rounded down to the nearest integer-respectively. In PSL 2 type steels, suffices indicates delivery conditions and R means as-rolled, N means normalized, Q means quenched, and M means thermomechanically rolled.

In oil and natural gas transportation, API 5L X42, X52 and X60 (PSL 1) steels are commonly used. Since in pipelines higher strengths are required, API 5L X70M (PSL 2) is widely used with its advantages coming from thermomechanical processing, its price/performance ratio and its availability over API 5L X65 and X80.

X70M grade steel should have min. 70 ksi (485 MPa) yield strength and thermomechanically formed. The mechanical properties and chemical composition specified by the standard are given in Table 2.1 and Table 2.1 [1].

Table 2.1. Mechanical properties of API 5L X70M grade pipeline steels [2]

Steel Grade	Yield Strength (MPa)		Tensile Strength (MPa)		Elongation (%)
	min	max	min		min
X70M	485	635	570	X70M	485

Table 2.2. Chemical composition limitations of API 5L X70M grade pipeline [2]

Steel Grade	Maximum Mass Fraction (wt.%)									Max. Carbon Equivalent	
	C	Si	Mn	P	S	V	Nb	Ti	Other	CEIIW	CEPcm
X70M	0.12	0.45	1.70	0.25	0.015	a	a	a	b,c	0.43	0.25
a Nb + V + Ti ≤ 0.15% b Cu ≤ 0,50 %; Ni ≤ 0,50 %; Cr ≤ 0,50% and Mo ≤ 0, 50 %. c B ≤ 0,001%.											

Although increasing the carbon content of the steels increases the strength and the hardness, it deteriorates the some other properties such as fracture toughness and weldability. Microalloyed steels, or high-strength low-alloy (HSLA) steels, have been developed to provide better properties (e.g., mechanical and atmospheric corrosion resistance) than conventional carbon steels. HSLA steels have yield strength greater than 275 MPa and they have low C content (0.05% to 0.025%) to optimize formability and weldability, and they have Mn content up to 2.0% [3] .

Microalloying basically increases the strength of the steel via grain refining and precipitation strengthening by adding small amounts of alloying elements, mainly vanadium, niobium, and titanium as well as some other elements such as molybdenum, copper, boron, zirconium, and nitrogen. *Table 2.3* summarizes the review of Vervynckt et al.[4] shows the effects of frequently used microalloying elements. V, Nb, and Ti are very effective when they used as microalloying elements in ferrite-

pearlite steels and have different strengthening mechanisms. Coarse titanium nitrides formed in microalloyed steels are stable at high temperatures and this gives control of the austenite grain size at elevated temperatures such as pre-hot working and welding processes. Low-temperature carbide and carbosulfide precipitates of Ti strengthen the material. The most important role of Niobium in steel is the austenite conditioning by controlling the austenite defect amount which could be possible nucleation sites for ferrite during transformation. It also helps grain refinement by retarding recrystallization of austenite with its carbides and nitrides which are dissolved in austenite at elevated temperatures. Furthermore, the precipitation of Nb(C, N) in ferrite increases the strength around 90 MPa. Although Nb is a ferrite stabilizer, it unexpectedly retards austenite to ferrite transformation even at very low Nb concentrations by exerting a solute drag on the phase boundary. Vanadium does not form precipitates in austenite and it joins precipitation hardening during and after the austenite to ferrite transformation. Depending on the rolling plan and chemical composition, precipitation of Vanadium carbides and nitrides can lead to remarkable strength increases [4]. Unless ferrite or pearlite structures are desired, to enhance the hardenability, Mo is added to hot worked HSLA steels. Despite Mo retards bainite growth with a solute drag concept, its retardation effect on pearlite and ferrite formation is more dominant. Additions of before mentioned alloying elements in very small amounts increases the strength of the standard carbon steels without any further processes by increasing the complete recrystallization temperature and retard austenite recrystallization. Moreover, their precipitation particles inhibit the grain growth of austenite, which will be transformed to ferrite, by solute drag and pinning effects and results in finer microstructure. This gives the opportunity to increase the weldability and toughness of the steel by decreasing carbon content without decreasing the strength [3].

Table 2.3. Alloying elements frequently used in HSLA steels [4]

Element	Amount in HSLA/wt%	Influence
C	<0.25	-Strengthener
Mn	0.5-2	-Delays austenite decomposition during accelerated cooling -Mild solid solution strengthener -Decreases ductile to brittle transition temperature
Si	0.1-0.5	-Deoxidiser in molten steel -Solid solution strengthener
Al	>0.02	-Deoxidiser -Limits grain growth (AlN)
Nb	0.02-0.06	-Very strong ferrite strengthener [Nb(C,N)] -Grain size control -Delays $\gamma$ to $\alpha$ transformation
Ti	0-0.06	-Grain size control (TiN formation) -Strong ferrite strengthener
V	0-0.1	-Strong ferrite strengthener (VN)
N	<0.012	-Forms TiN, VN and AlN
Mo	0-0.3	-Promotes bainite formation
Ni	0-0.5	-Increases fracture toughness
Cu	0-0.55	-Improves corrosion resistance -Ferrite strengthener
Cr	0-1.25	-Improves atmospheric corrosion resistance (when Cu is also added)

In API standard, M letter following the yield strength digits indicates the delivery condition; thermomechanically rolled condition. Along with the microalloying, thermomechanical processing is another efficient way of achieving superior mechanical properties and it has importance in microstructural evolution of many line pipe steel including API 5L X70M.

Thermomechanical Controlled Process (TMCP) was born in a need of an alternative way to obtain finer grain sizes to increase both strength and toughness apart from traditional heat treatment processes. As indicated by Llewellyn [5], in the late 1950s, to increase the impact properties micro-alloyed steels, the normalizing process is applied, however, while this goal is achieved, the strength advantage of the micro-alloyed steel was lost. It is first developed in Japan in the 1980s, adopting lower finishing temperatures than normal finishing temperatures to obtain finer microstructure and better mechanical properties became known as controlled rolling and it evolves to the term thermomechanical processing with time to cover both hot-rolling and accelerated-cooling stages during the course of operation.

As a two-stage process, when TMCP (Figure 2.1) is compared with traditional hot working operations a time delay between roughing and finishing draws the attention. The time delay enables one to carry out the finishing operations at temperatures below recrystallization temperature. This results in the formation of pancaked austenite grains and transformation to a fine-grained acicular ferrite structure. Addition of carbide forming elements, which are discussed before, remarkably facilitate the process. Particularly, it was shown that the addition of about 0.05% Nb causes a marked retardation in recrystallization allowing controlled rolling at significantly higher temperatures [5].

The uniform and very fine acicular ferrite microstructure in TMCP steels yields higher strength and better toughness. Furthermore, TMCP process facilitates lower hardenability, TMCP steels can be used in welding applications where extra high heat input is required and as stated by Kikuta et al. it improves weld cold cracking resistance, especially in the rolling direction [6]. Cuddy reported that to obtain a fine acicular ferritic microstructure in HSLA steels, austenite grains should be flattened and elongated by increasing deformations at lower finishing temperatures [7].

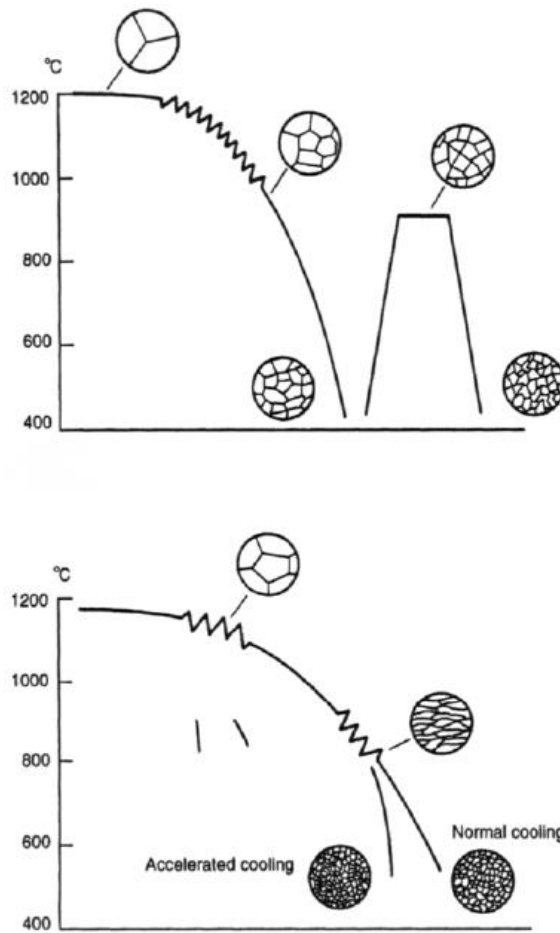


Figure 2.1. Schematic representation of rolling schedules of traditional rolling and normalizing (upper) and thermomechanical processing (lower) [5]

Microalloying increases the strength of the steels significantly through grain refinement and precipitation hardening by adding small amounts of alloying elements. With microalloying and different processing methods, different microstructures are formed such as polygonal ferrite (PF), quasi – polygonal ferrite (QP) or massive ferrite, bainitic or acicular ferrite (BF, AF), granular ferrite (GF) and granular bainite (GB) [8].

Microstructural definitions on API X70M PSL2 is done according to the definitions by Araki et al.[9] and Krauss and Thompson [8] in the light optical microscope and scanning electron microscope in Figure 2.2 and Figure 2.3. PFs are the microstructures which are formed at higher temperatures and slower cooling rates and grows into equiaxed grains. On the other hand, AF is the finer ferritic microstructure which is transformed from austenite in the intermediate temperature ranges [8].

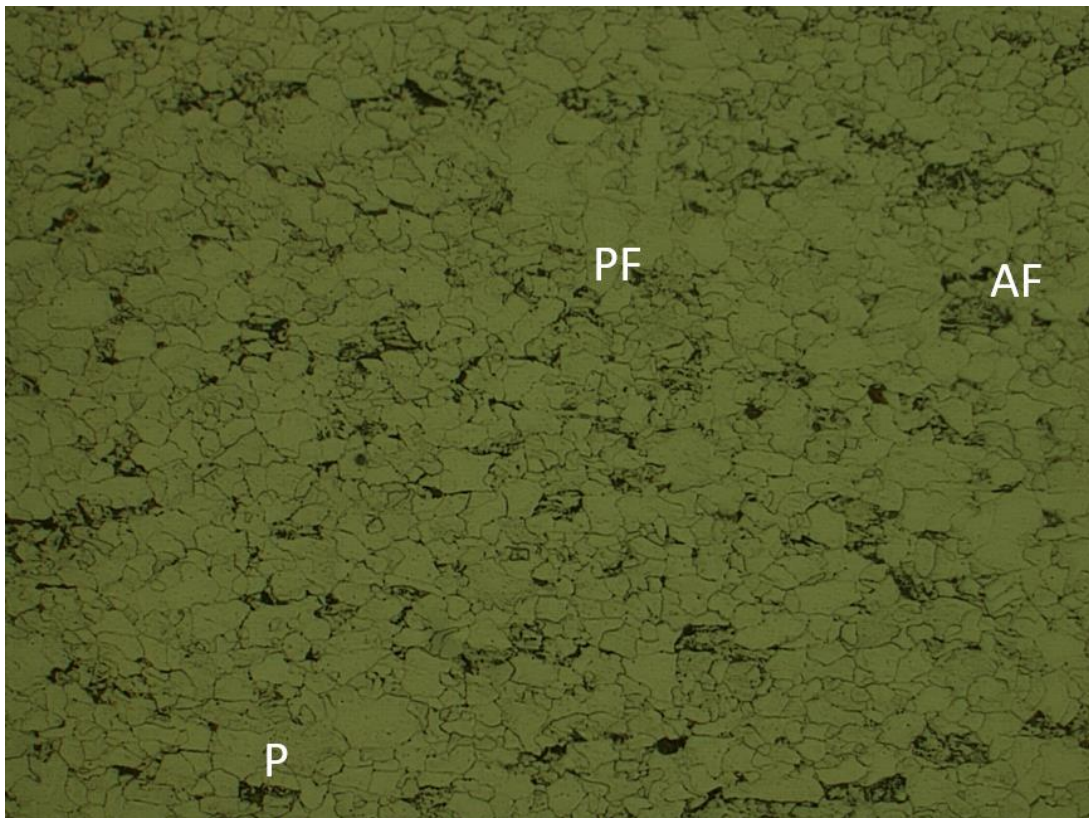


Figure 2.2. Light Optical Microscopy (LOM) micrograph of the API X70M steel. (AF: acicular ferrite, PF: polygonal ferrite, P: pearlite). 1500X [8]

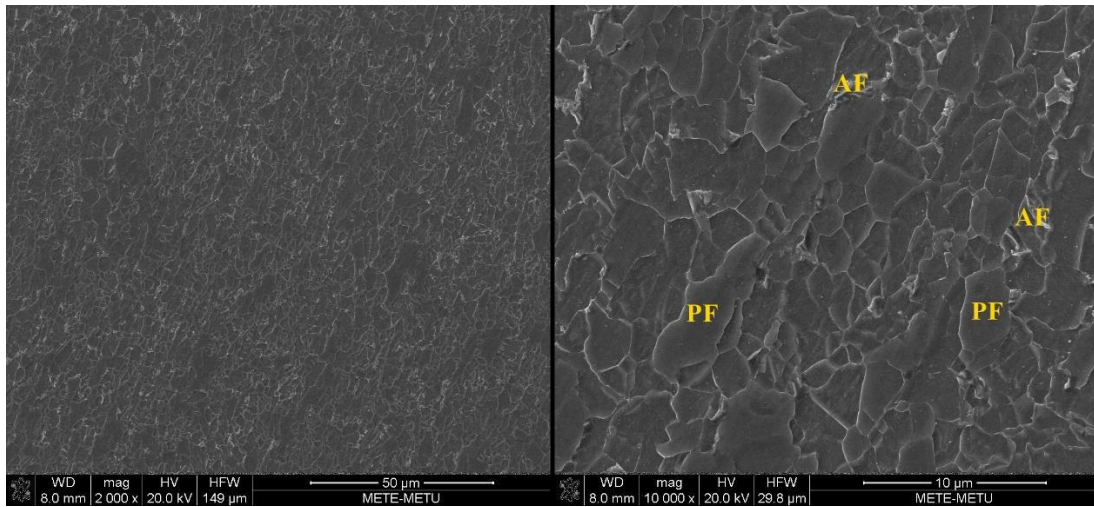


Figure 2.3. Scanning Electron Microscope (SEM) micrograph of the base metal. (AF: acicular ferrite, PF: polygonal ferrite). [8]

Lan et al. have worked on effects of different microstructures on mechanical properties of API X70 steel. When high finish rolling and cooling stop temperatures are applied, microstructures are mainly composed of QF with P and little AF, stated as A and B. On the other hand, lower finish rolling and cooling stop temperatures yield AF as major microstructural constituent together with GF and QF namely C and D. SEM micrographs of these steels are given in the Figure 2.4. Tensile tests and Charpy V-notch impact toughness tests between -10 and -60°C were performed. Results of these tests are summarized in Table 2.4[10].

Table 2.4. Tensile Properties and Impact Absorbed Energies of Different Microstructured API X70 Steels [9]

Steel	Yield Strength (MPa)	Tensile Strength (MPa)	Elongation (%)	Yield Ratio (%)	Absorbed Energy (J)		
					-10°C	-40°C	-60°C
A	485	595	23	0.82	75	55	47
B	490	600	20	0.82	77	65	40
C	545	670	25	0.81	135	145	130
D	580	700	20	0.83	147	160	14

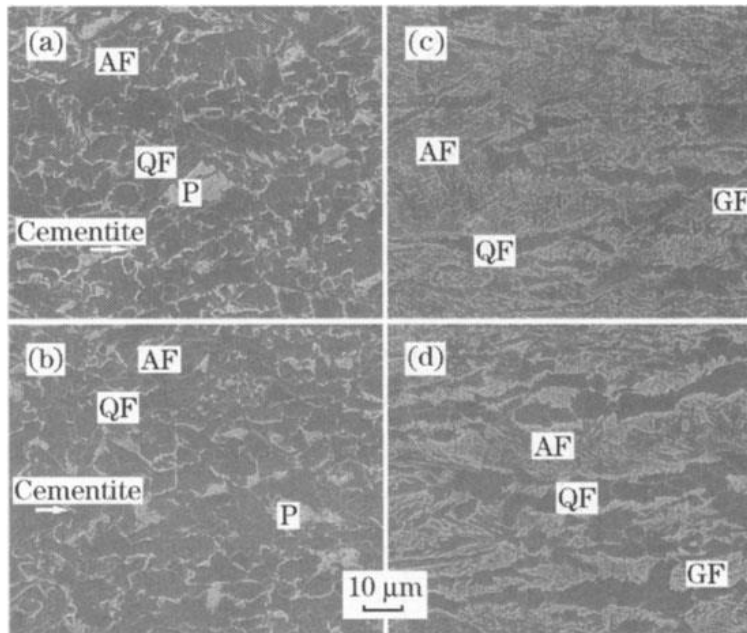


Figure 2.4. SEM Micrographs of API X70 Steel produced with Different Rolling Process Routes. (a) Steel A, (b) Steel B, (c) Steel C, (d) Steel D [9]

Zhao and Palmiere stated that acicular ferrite fraction increases with reduced prior austenite size to some extent, and reducing the austenite grain size refines the microstructure and homogenizes the structure. However, further reduction of prior

austenite size does not affect the acicular ferrite fraction and refinement of the transformed microstructure [11].

### **2.3. Girth Welding of Line Pipes**

For girth welding, arc fusion welding techniques are used. In the mainline pipes, it is done automatically with GMAW technique. For the tie-ins manually GTAW and SMAW techniques and semi-automatically gas-shielded FCAW and MCAW techniques are used.

Fusion welding process joins or fuses materials with or without a filler material by heating them up to their melting points via different heat sources such as electric arc, electrical resistance, gas or plasma.

Temperature gradients in fusion welding techniques are higher than that of casting processes as the heat source, the welding torch, moves and base, and molten metal starts to cool down immediately. Figure 2.5 shows the distributions of temperature in a welding process. While temperature may exceed 1500°C in the center of the weld pool, it drops to 500-600°C in 3-4 mm after the torch has passed.

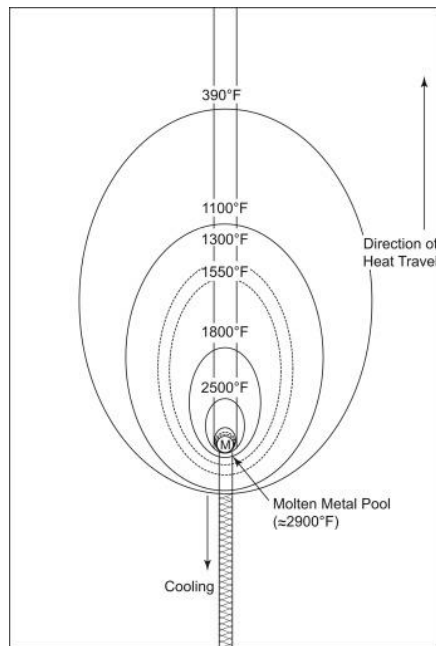


Figure 2.5. Temperature distribution in a welding process [11]

As it is mentioned before, fusion welding can be done with or without filler material. Methods using filler material must be designed carefully with respect to the base metal and the desired microstructure since it can alter the chemical composition of the base metal and consequently the microstructure of the Fusion Zone and Heat Affected Zone. Without a filler material, the main concern is thermal cycles which base metal is experienced. The effect of these thermal cycles on the microstructure of the materials changes with the distance from the Fusion Zone, Heat Input and the heat transfer characteristics of the materials.

Arc welding is one of the fusion welding techniques which uses the heat of an electric arc forming between the base metal and electrode to melt and join materials. Different electrodes are used in arc welding as consumable and non-consumable ones. Consumable electrodes melt and fill the gap between the metals. Therefore, the chemistry of the electrodes should be complementary or compatible with base metal since they become a part of the weld itself. Non – consumable electrodes do not melt

during welding except the very tip of the electrode. They are made of carbon or high melting point metals, alloys or combination of these with oxides such as pure tungsten, tungsten with 1% thorium, and tungsten with a 0.3-0.5% zirconium.

During welding, the molten metal is very sensitive to atmospheric gases such as oxygen, nitrogen, hydrogen, and oxides of carbon. These gases may cause defects and undesirable microstructure and deteriorate the weld structure when they react with molten metal. Weld pool and the fusion zone should be protected to have free of contaminants and sound weld. Fluxes or shielding gases are used to protect the weld from the atmosphere and the classification of the arc welding techniques is based on the way of protection and arc characteristics.

In Table 2.5 basic arc welding methods can be classified in European norms and American codes are given. European standards have numerical designations in addition to alphabetical representation.

Table 2.5. Arc welding methods

<b>AWS / ASME</b>	<b>EN / ISO</b>
Shielded Metal Arc Welding (SMAW)	Manual Metal Arc Welding (MMA), 111
Submerged Arc Welding (SAW)	Submerged Arc Welding (SAW), 12
Gas Metal Arc Welding (GMAW)	Metal-Arc Inert/Active Gas Welding (MIG/MAG), 131/135
Flux Cored Arc Welding (FCAW)	Flux Cored Wire Metal Arc Welding (FCAW), 114
Gas Tungsten Arc Welding (GTAW)	Tungsten Inert Gas Welding (TIG), 14

Shielded metal arc welding (SMAW), also called manual arc welding (MMA), is one of the earliest manual arc welding processes in which consumable coated metal electrodes are used. Consumable metal electrode core is covered with mixtures of substances such as chemicals and minerals. Once the arc is generated, the arc heat melts the core and the flux, thus a protective shield gas environment is formed by ionization of the gas at molten state. The flux is also prevents atmospheric contamination during solidification by forming a slag on the weld metal. Schematic representation of the technique is given in Figure 2.6.

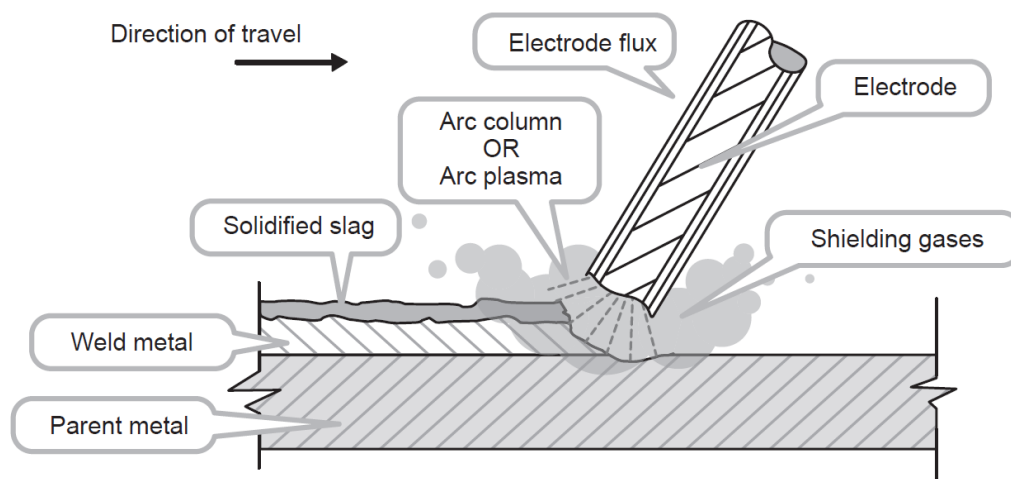


Figure 2.6. Schematic representation of SMAW technique[12]

Gas metal arc welding (GMAW), is also named as metal inert gas (MIG) welding when the shielding gas is inert or metal active gas (MAG) welding when the gas contains an active gas can be seen in Figure 2.7 representatively. An electric arc is created between the workpiece and automatically fed wire and the weld zone, FZ and HAZ, is protected by supplying a gas or gas mixture via a gas nozzle. The gas mixture is determined specifically to the material and the type of metal transfer mode.

Normally, for welding of aluminum, copper, magnesium inert gases/gas mixtures are used such as pure argon or argon helium mixtures. In welding of low carbon and mild steels, argon with CO<sub>2</sub> (5-20%) and sometimes some O<sub>2</sub> gas mixtures are the most popular ones. Argon is also used for stainless steels with the addition of small amounts (1-3%) of CO<sub>2</sub> or O<sub>2</sub>.

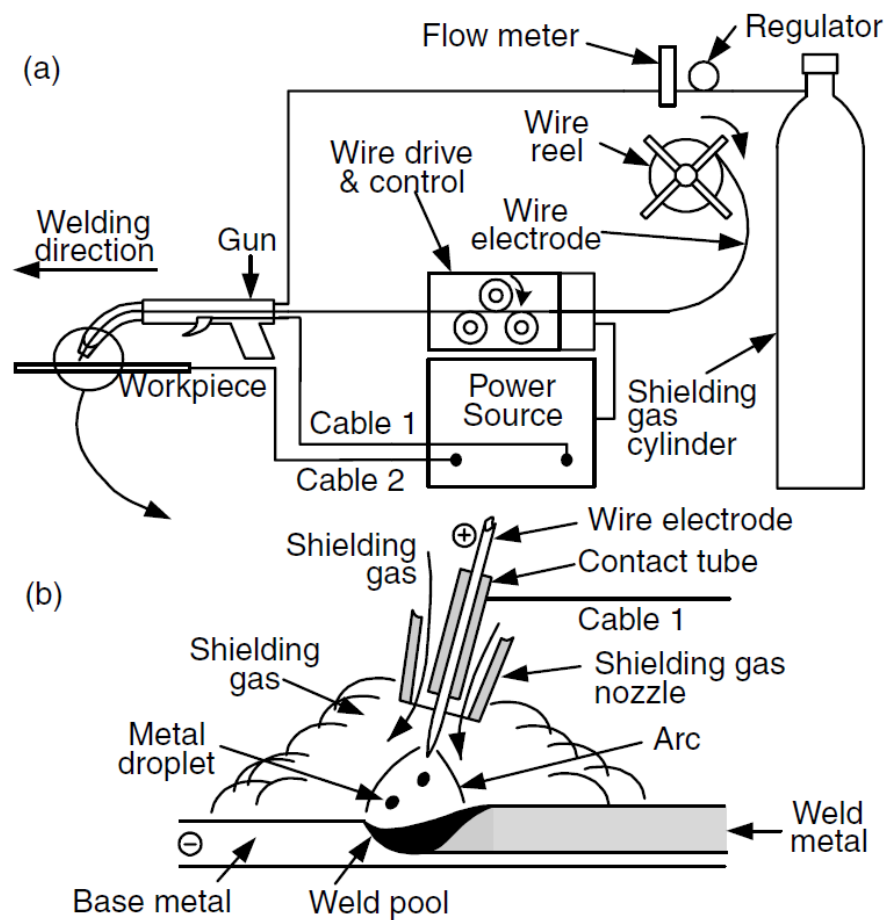


Figure 2.7. Gas-metal arc welding: (a) overall process; (b) welding area enlarged [13]

The gas mixture is determined specifically to the material and the type of metal transfer mode. Normally, for welding of nonferrous metals such as aluminum, copper, magnesium inert gases/gas mixtures are used such as pure argon, helium or their mixtures. Since Ar has lower thermal conductivity, the arc energy is less uniformly dispersed in an Ar arc than a He arc. As a result, Ar arc plasma has higher energy than He in the core and an outer mantle of lesser energy. This leads to a more stable, axial transfer of metal droplets through arc plasma. In welding of ferrous metals, pure He shielding may produce spatter and pure Ar shielding may cause undercutting at the FL. Argon with CO<sub>2</sub> (5-20%) and sometimes some O<sub>2</sub> gas mixtures are the most popular ones to overcome these problems. Argon is also used for stainless steels with the addition of small amounts (1-3%) of CO<sub>2</sub> or O<sub>2</sub>. Generally, CO<sub>2</sub> is used as a shielding gas in carbon and low-alloy steels because of its advantages on welding speed, penetration, and cost. When CO<sub>2</sub> is used as a shielding gas, it produces a high level of spatter, the electrode tip is actually below the base metal surface because a relatively low voltage is used to minimize spatter [13].

There are three basic metal transfer modes exist at the electrode tip when the molten metal is transferred to the weld pool:

- **Globular transfer:** Under the influence of gravity, discrete metal drops generally larger than the electrode diameter move across the arc gap. It produces spatter and it is not smooth generally. Figure 2.8a shows the globular transfer mode
- **Spray transfer:** Under the influence of electromagnetic forces, small discrete metal drops move across the arc gap at a higher frequency than globular transfer. It does not produce much spatter and metal transfer is much more stable than the globular mode. Figure 2.8b shows the spray transfer mode.
- **Short-circuiting transfer:** Transfer of the molten metal at the electrode tip is done when short-circuiting occurs i.e. when it touches to the weld pool

surface. The created weld pool is small and fast – freezing and therefore it is desirable to use it in the welding of thin sections.

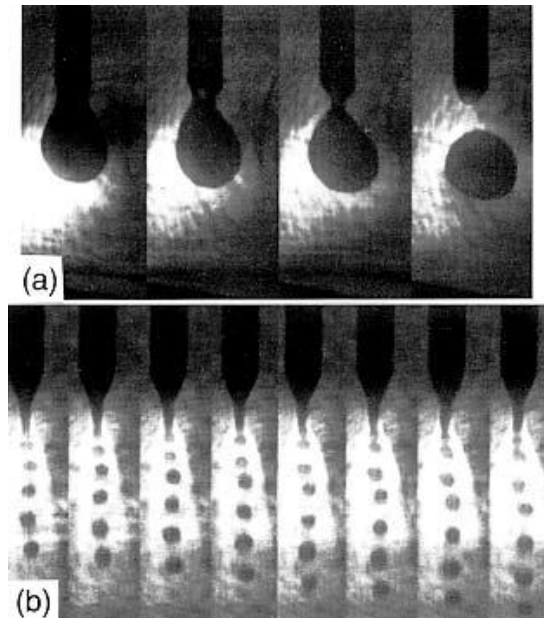


Figure 2.8. Metal transfer during GMAW of steel with Ar–2% O<sub>2</sub> shielding: (a) globular transfer at 180A and 29V shown at every  $3 \times 10^{-3}$  s; (b) spray transfer at 320A and 29V shown at every  $2.5 \times 10^{-4}$  s. Reprinted from Jones et al.[15]. Courtesy of American Welding Society

Flux-cored arc welding (FCAW), the schematic view can be seen in Figure 2.9, has similarities with GMAW. However, as the name implies, flux cored electrodes are used in FCAW rather than solids. The electrodes are in tubular structure with flux inside. These electrodes can be used with external shielding gases or they are self-shielded itself. In self-shielded electrodes, the flux decomposes and vaporizes in the arc and produce a shielding gas environment to protect the FZ and HAZ from atmospheric gases. An extensive slag coverage is obtained during welding and this slag slows down the cooling of the weld. However, this requires the removal of the slag after welding via a hammer or wire brush between the passes to keep the weld free from inclusions. Pre-heating of these self-shielding flux-cored electrodes

increases burn-off efficiency and deposit rate; and decreases penetration depth. These electrodes simplifies the welding operation since additional equipment such as big welding guns and shielding gas tubes are eliminated.

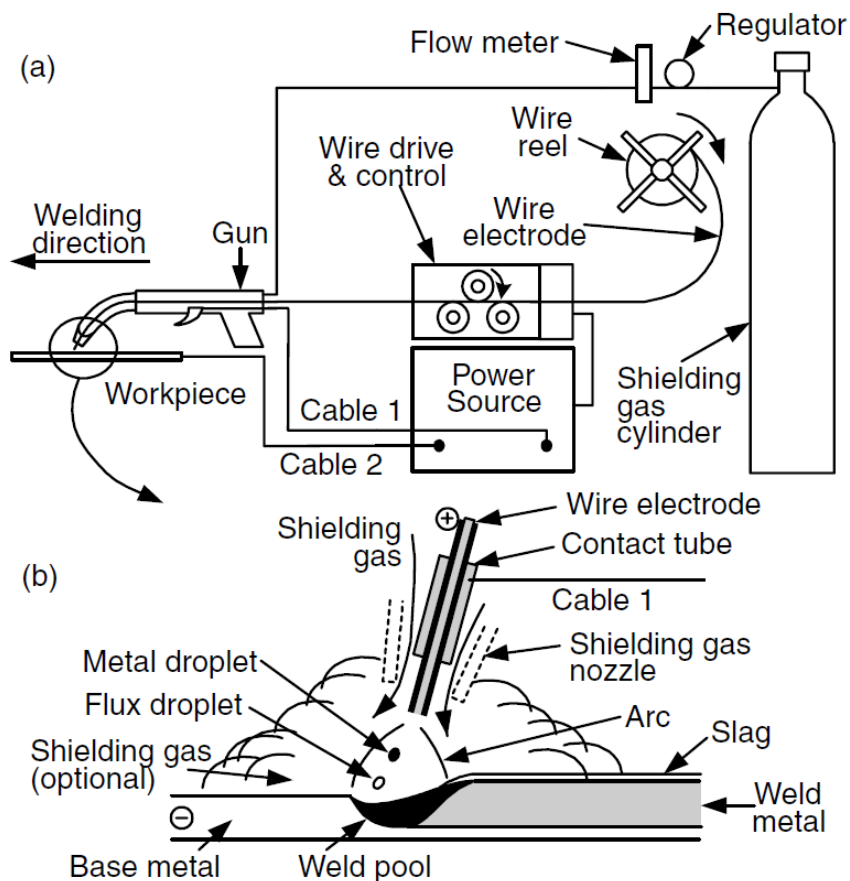


Figure 2.9. Schematic view of flux-cored arc welding (FCAW) (a) overall process (b) welding area enlarged

There are some disadvantages of self-shielding electrodes used in FCAW method. Precautions should be taken to a large amount of fumes which may affect the human health produced during welding. Self-shielding electrodes have detrimental effects on weld metal due to their contents which denitrifies and deoxidize the weld metal. For instance, even though it neutralizes the undesired effect of oxygen in the arc zone,

primary element aluminum inside the core lowers impact toughness and ductility of the weld metal in FZ. To overcome these effects, external shielding gases are used. CO<sub>2</sub> is the most widely used because of its low cost and benefits in deeper penetration. Depending on the material being welded, the CO<sub>2</sub> can act as either carburizing or decarburizing medium. In metals having higher C content more than 0.10%, decarburization may occur and CO can be trapped in the weld metal and can cause porosity [14].

Metal-Cored Arc Welding (MCAW) is another form of GMAW using metal cover and a core of powdered materials producing slag on the face of a weld bead. In this method, external shielding gas variations are wider and alloy compositions are more flexible than GMAW.

Gas-tungsten arc welding (GTAW) is a fusion welding process in which the arc is created between a non-consumable electrode, generally tungsten, and the workpiece. The arc melts the parent metal. The weld pool is protected by an inert gas supplied through welding torch via a nozzle and excludes atmospheric gases from the weld area. Because of the gases used, GTAW is also referred as tungsten *inert* gas (TIG) welding. GTAW can also be performed using filler materials in rod form.

Different polarities can be used in GTAW with respect to the application area (Figure 2.10):

- **Direct-Current Electrode Negative (DCEN)** This is the most common polarity used in GTAW and also called as straight polarity. The electrode is connected to the negative terminal of the power supply and electrons flow towards the base metal. Electrons are accelerated while traveling through the arc and strike the base metal at high velocity due to a potential difference. The

amount of energy required to emit an electron from the electrode is called work function and it is released when the electron hits the base metal surface. It is considered 66% of the total arc heat is located in the base metal and the rest is at the electrode end. This helps in melting of the base metal and yields a relatively narrow and deep weld.

- **Direct-Current Electrode Positive (DCEP)** The base metal is connected to the negative terminal of the power supply and this is also called the reverse polarity. Electrons are emitted from the base metal and flow toward the electrode. This time the heating effect is at electrode rather than the base metal. Therefore, a large diameter, water-cooled electrodes should be used in order to prevent the electrode from melting. During the avalanche of electrons from base metal, oxide films are knocked off and a clean weld surface is obtained.
- **Alternating Current (AC)** This polarity has moderate effects in terms of penetration and oxide cleaning. [15]

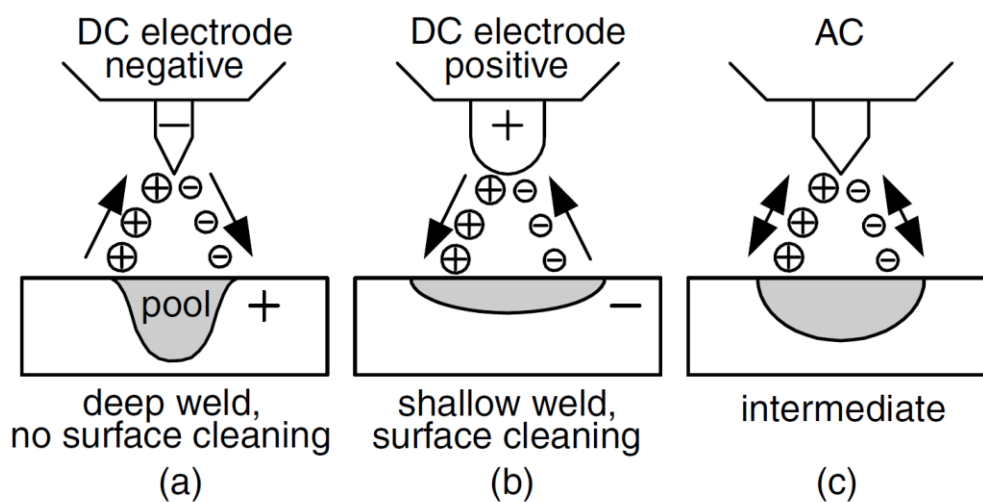


Figure 2.10. Different polarities in GTAW (a) DCEN (b) DCEP (c) AC [13]

GTAW has advantages such as stable arc and excellent control of the welding. It can be used for welding of stainless steel and copper and owing to its cleanliness it can be used in the welding of reactive metals such as titanium, zirconium, aluminum alloys, and magnesium alloys. It can be used in the welding of thin sheets without filler material. However, GTAW is applicable to thin materials, from about 0.5 mm up to 3 mm thickness and the deposition rate is very low when compared with other methods such as GMAW and SMAW. The deposition rate can be improved by using pre-heated electrodes. Moreover, the process is highly skill dependent and requires experienced and talented welding operators. Higher welding currents may cause the melting of the non-consumable tungsten electrode and may yield tungsten inclusions in the weld metal.

Heat source efficiency  $\eta$  can be defined as

$$\eta = \frac{Qt_{weld}}{Q_{nominal}t_{weld}} = \frac{Q}{Q_{nominal}} \quad (1)$$

where  $Q_{nominal}$  is the nominal power heat source and  $Q$  is the rate of transferred heat from the heat source to the workpiece.  $t_{weld}$  is the welding time. When the heat provided by heat source flows through the workpiece, some of the energy is transferred to the workpiece and the remaining is lost to the surroundings.  $Q$ , heat transfer rate, can easily be calculated from the Equation 2.

The arc efficiency can be expressed as

$$\eta = \frac{Qt_{weld}}{VIt_{weld}} = \frac{Q}{VI} \quad (2)$$

where  $V$  is the constant voltage and  $I$  is the constant current. In welding, the term heat input is often referred to  $Q_{nominal}$  or  $VI$  in the case of arc welding. The term heat input

per unit length can be calculated by including the efficiency to the expression  $Q_{nominal}/v$ , or  $VI/v$  where  $v$  is the welding speed [15]. The heat input formula for kJ/mm is given as

$$HI \text{ (Heat Input)} = \eta \times 60VI/1000v \quad (3)$$

where  $V$  in volts,  $I$  in amperes and  $v$  is in millimeters per minute.

Efficiencies of the welding techniques according to the EN 1011-1 are given in Table 2.6

Table 2.6. Efficiencies of different welding techniques [16]

Welding Technique	Efficiency ( $\eta$ )
Submerged Arc Welding (SAW)	1.0
Shielded Metal Arc Welding (SMAW)	0.8
Gas Metal Arc Welding (GMAW)	0.8
Flux-Cored Arc Welding (FCAW)	0.8
Gas Tungsten Arc Welding (GTAW)	0.6

Among the weld parameters such as weld metal type, shielding gas, weld speed, etc. heat input one of the most important welding parameters regardless of the welding method.

#### 2.4. Welding Metallurgy of HSLA steels

Figure 2.11 shows typical microstructures evolved between the fusion zone and base material after a single pass welding. Fusion zone is the regions that reach temperatures that are higher than the melting point of the material. The thinner section right next to

the fusion zone is named partially melted zone (PMZ) which represents the transition boundary between 100% solid and 100% liquid. Along the HAZ, different microstructures are seen due to the thermal cycles. The coarse-grained HAZ can be seen adjacent to the fusion line where overheating and slow cooling occurs. Grain size decreases and fine-grained HAZ is observed towards the base metal as the induced heat decreases. In this zone, the temperature is below the melting point and partial grain refinement occurs.

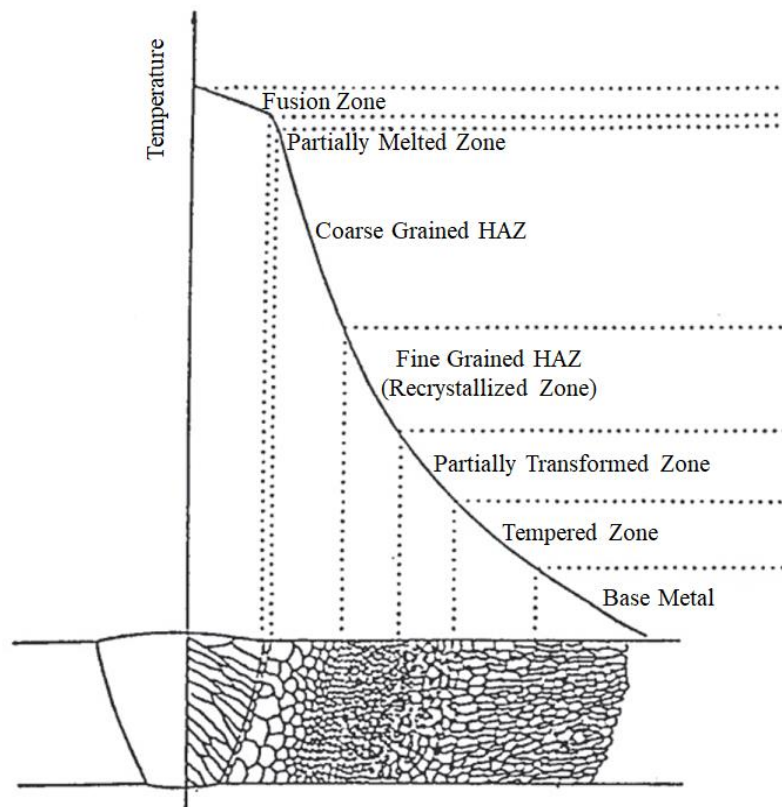


Figure 2.11. Typical microstructural features of a single pass welding [17]

HSLA steels are developed to be used in structural applications such as pipelines, offshore structures, bridges, buildings, etc. They have better material properties than the conventional C-Mn steels as stated before in Section 2.2 while weldability of these steels is considerably better than that of conventional steels. During the course of

welding, some new regions are formed, fusion zone (FZ), and some regions are changed, heat affected zone (HAZ), due to fusion and thermal effects. Since heating and cooling rates in welding are very high, multi thermal cycles which include these heating and cooling sequences are very effective in the formation of microstructure after multi-pass welding. Figure 2.12 shows the evolution of microstructure in HAZ via single and multi-pass welding.

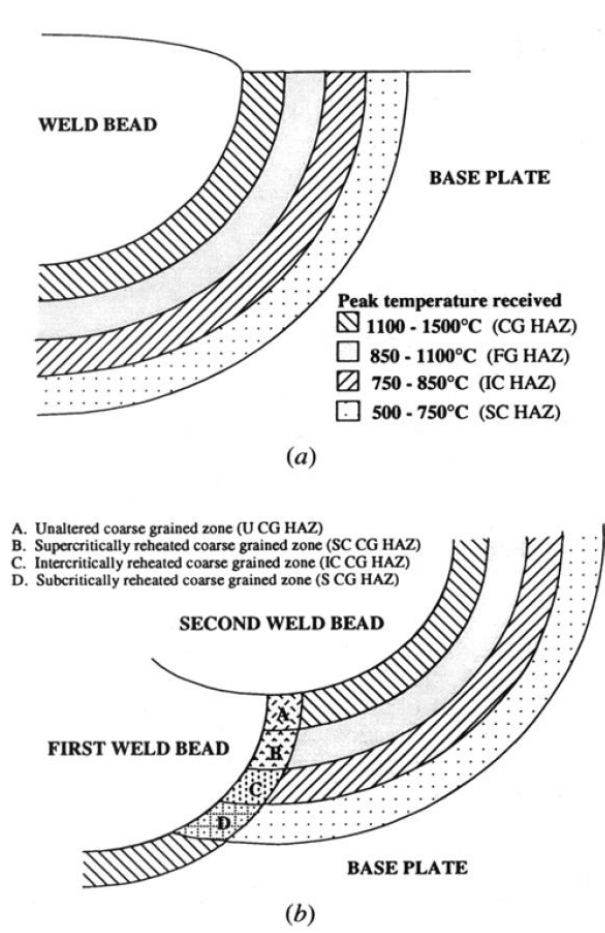


Figure 2.12. HAZ microstructure variations in single and multi-pass welding [18]

HAZ region is the weakest location of the welds and the success of the welding can be inspected by investigations on this region. Due to heat input and diffusion of

welding consumables alter the microstructure of the HAZ and the effectiveness of the strengthening mechanisms such as work hardening, precipitation hardening, and transformation hardening is reduced significantly. Cooling rates are inversely proportional with the amount of heat input if there is no external parameter or applications. In a metallurgical aspect, as the heat input increases cooling rate decreases and the grain sizes within the HAZ enlarge and the width of the HAZ increases. On the other hand, lower heat inputs, or higher cooling rates, yield smaller grain size.

In coarse-grained heat affected zone (CGHAZ) and intercritically reheated coarse-grained heat affected zone (IRCGHAZ), the deteriorating effect of heat can be seen explicitly. Enlarged grains in different morphological formations with different chemical and mechanical properties are seen in these regions. CGHAZ forms near the fusion line and exhibits the lowest toughness in single pass weldments [18]. In multi-pass welding, IRCGHAZ is known as the most weakened part [19], [20] in which local brittle zones (LBZ), which include martensite-austenite (M-A) islands composed of high carbon and retained austenite, formation occurs [21], [22]. Because of the brittle nature and crack susceptibility of martensite, the M-A phase formation plays a significant role in the toughness of the steels. It may suddenly decrease the toughness. Peak temperature ( $T_p$ ) and cooling time ( $\Delta t_{8/5}$ ) govern these microstructural alterations. In their work, Haugen et al. [23] showed that 5 or 10 s  $\Delta t_{8/5}$  caused M-A phase formation along the prior austenite grain boundaries (PAGB) in weld simulations where peak temperature of 1350 °C in the first cycle and 780 °C in the second cycle. The M-A phase formation occurs because of the enhanced local hardenability in austenite due to carbon diffusion [23]. Li et al. found the evidences of both cracking and debonding of the M-A phase and carbides and cracks were correlated with the consolidation of voids as a result of debonding [24]. The toughness decrease is not only correlated with the presence of M-A phase but is also related with morphology and distribution of the phase and the matrix. The M-A phase is found at

two distinct morphologies, blocky particles, or islands, in 3 to 5  $\mu\text{m}$  in diameter which form at the PAGB and elongated stringer-type particles which are formed between bainite-martensite laths 0.2 to 1  $\mu\text{m}$  in width and several microns in length[25].

Four possible mechanisms proposed for toughness decrease have been gathered together by Davis and King and they are shown schematically in Figure 2.13 [25]:

- The M-A phase is brittle in its nature and cracks readily
- There occurs transformation-induced residual stress in the surrounding ferrite matrix
- The M-A phase harder than the surrounding ferrite and cause stress concentration in the ferrite matrix
- A microcrack is formed between the M-A and ferrite matrix and initiates the cleavage fracture in the matrix

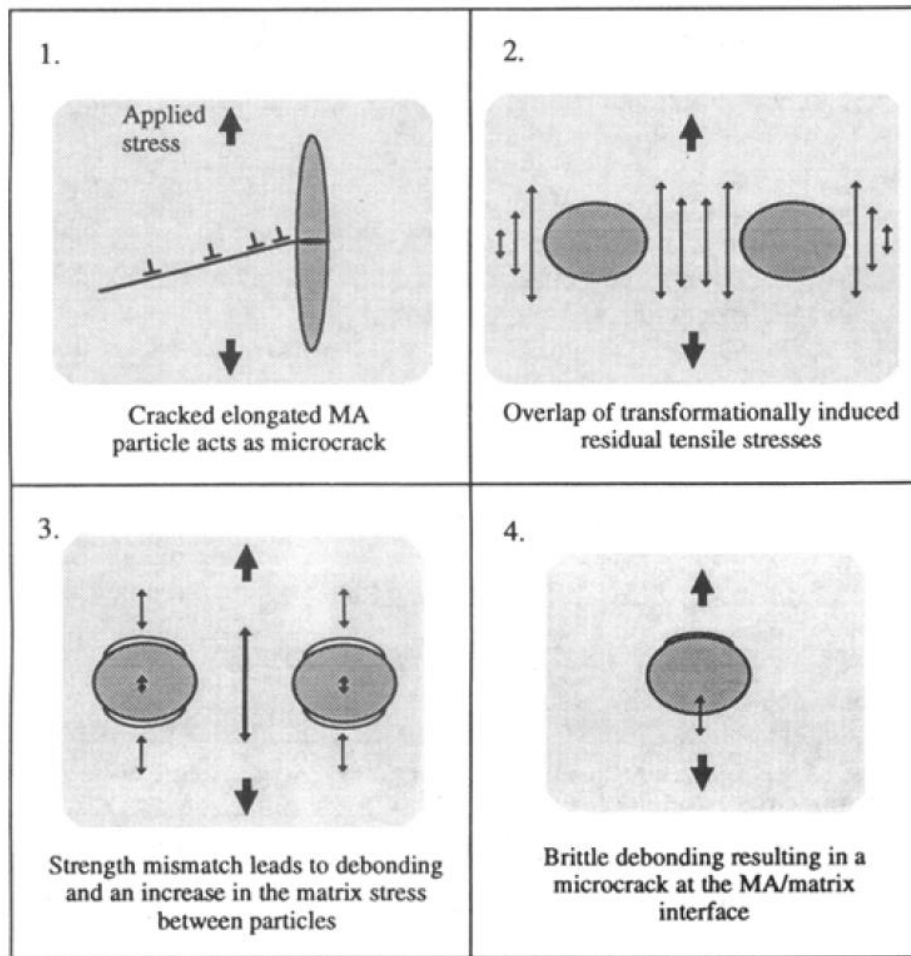


Figure 2.13. Representation of four proposed initiation mechanisms[25]

As discussed in 2.2. Parent Material microalloying elements such as Ni, V, Nb, and Ti, affect the number of phases and microstructure. Various kinds of austenitic phases would exist in CGHAZ and IRCGHAZ if the filler material has a high amount of austenite promoter elements and enough diffusion time is given. In HSLA steels, Nb, V, and Ti are strong carbide and nitride forming elements. Titanium nitride is the most stable one among the carbides and nitrides of Nb, V, and Ti. It has the smallest tendency to decompose and dissolve at elevated temperatures. Therefore, it is the most effective particle that limits the grain growth in welding [15]

The cooling rate affects the width of the HAZ. Lower cooling rates increase growth rate during solid-state diffusion in HAZ. The fine-grained structures move towards the base metal until the phases become stable. The partially transformed structure in HAZ can be changed based on the aforementioned parameters. Recrystallization and growth in the HAZ can make the region much vulnerable in terms of mechanical properties than that of base metal.

Fusion zone is the region in the weld where complete melting and re-solidification occurs during the process. Due to the solidification process, the fusion zone is different than HAZ and base metal distinctively. During welding, the base metal grains at the fusion line act as a substrate for nucleation. According to Turnbull's [26] formula,  $\Delta G$  for heterogeneous nucleation is:

$$\Delta G = \frac{4\pi\gamma_{LC}^3 T_m^2}{3(\Delta H_m \Delta T)} (2 - 3 \cos \theta + \cos^3 \theta) \quad (4)$$

where  $\gamma_{LC}$  is the surface energy in the liquid-crystal interface,  $T_m$  is the equilibrium melting temperature,  $\Delta H_m$  the latent heat of melting,  $\Delta T$  is the undercooling below  $T_m$  and the  $\theta$  is the contact angle. Figure 2.14 shows the nucleation of a crystal on a planar substrate. Since molten metal is in contact with the base metal, which is the substrate for nucleation, and it wets them completely, in other words, contact angle  $\theta$  equals to zero, crystals nucleate from liquid metal on substrate readily.

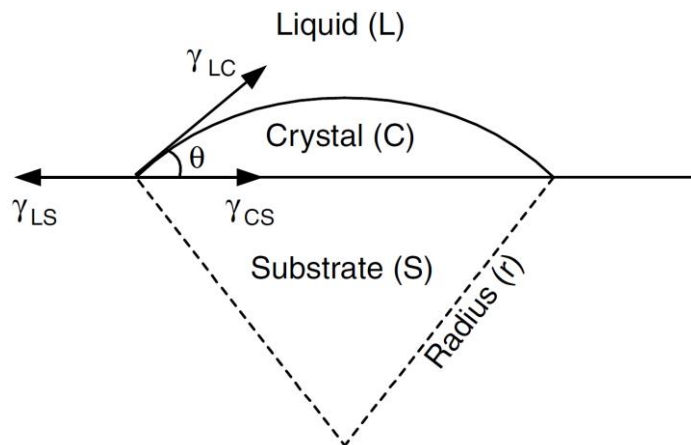


Figure 2.14. Nucleation of a crystal from a liquid on a planar substrate [13]

The growth can occur epitaxially in autonomous welding (welding without filler material). Nucleation occurs in the arrangement of atoms in one direction based on substrate crystallographic orientation without changing it. dendrites point one direction Savage et al. [27] confirmed that the crystallographic orientation continues along the fusion zone by using a back reflection X-ray technique. Weld metal crystal structure may differ from base metal in welding with a filler material since the metal compositions are different. In this case, epitaxial growth is no longer possible. In their work Nelson et al. [28] investigated the fusion boundary microstructure of dissimilar-metal welds by using a body-centered cubic (BCC) and a face-centered cubic (FCC) base metals, Type 409 stainless steel and 1080 pearlitic steel respectively, and an FCC filler material, Monel (70Ni-30Cu). In BCC base metal – FCC filler material system, no epitaxial nucleation, and growth are observed. Random grain boundary misorientations are observed between the weld metal and the HAZ as can be seen in Figure 2.15a. In FCC base metal – FCC weld metal system, normal epitaxial growth was observed at fusion boundary, the morphology of the weld metal is a result of the crystal structure of the grains along fusion zone which are the substrates of the nucleation, Figure 2.15b.

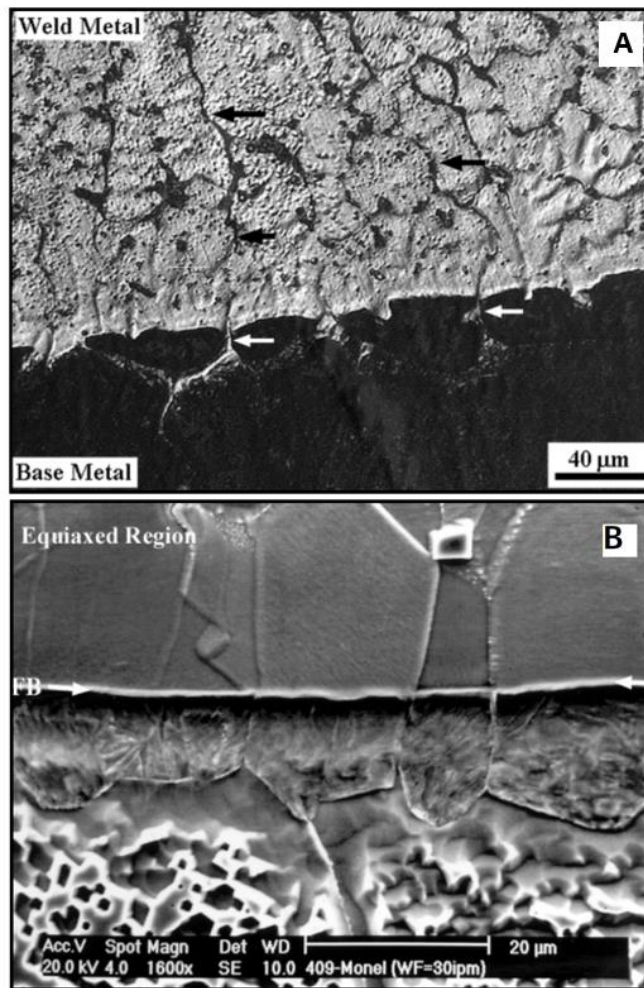


Figure 2.15. Fusion boundary microstructures a) Type 409/Monel base and weld metals b) 1080/Monel base and weld metals [27]

The weldability of the materials is affected by some factors mainly, material, purpose, weld design, and pre and post-processing. Material's microstructural features are phase transformations, grain formations, and segregations. Chemical composition of the material affects the hardenability, the aging and the convections in the weld pool. Physical characteristics of the material such as strength, thermal conductivity and expansion coefficient, and toughness are important for material characteristics. Purpose factor can be defined as mechanical, physical and chemical quality requirements. Weld design factor includes type, weld dimensions, level, strain rate,

and load distribution. Pre and post-processing includes welding method, filler material, heat input, consumables such as shielding gases and fluxes, joint type, pre-heating temperatures, and post-weld heat treatments.

## **2.5. Fitness-for-Service**

Pipelines used in industrial applications such as oil and gas transportation, water transportation are subjected to different loads and they are designed to bear service pressure. The pressure may be caused by internal or external factors. Gas transportation pipelines are categorized as intermediate pressure pipelines. Internal and external loads induced on pipes are generally similar. However, since they are built underground there could be some unexpected large scale loads due to an earthquake or movement of the earth such as landslides. Therefore, all these kind of existing and sudden loads should be taken into consideration and investigated to eliminate catastrophic failures.

Parts exposing different stress conditions and environments causing corrosion should maintain their strength, performance, and dimensions. Structural integrity is the competency of a part to work throughout its specified lifetime [29]. To guarantee the safe and useful working of product components; application of efficient inspection, examination and risk management techniques are required. Therefore, the structural integrity assessment is essential for giving not only design limitations and also preventing catastrophic failure. This assessment is named as Engineering Critical Assessment (ECA) and also as Fitness-For-Service (FFS) assessment for pipelines.

Conventional welding fabrication codes and standards specify weld's maximum tolerable flaw size and minimum Charpy energy-based qualified procedures and good workmanship. The good workmanship criteria is quite conservative and it should be. This conservatism is inevitable for manual welding applications and quality threshold

must be kept high since even the minimum requirements are met, there are many different workers in pipelines with different skill levels.

However, today girth welding of pipelines which are performed automatically or semi-automatically is higher than 80%. Because of that, welding parameters are in a limited range and this leads to consistent metallurgical and mechanical outputs. FFS analysis has been emerged to determine whether a given flaw is safe from failure, e.g. brittle fracture, fatigue, creep or plastic collapse, or not under working conditions. FFS analysis based on fracture mechanics and less conservative since it uses the accurate results of the fracture mechanics tests and stress analyses. This is advantageous for welding applications since unnecessary weld repairs in case of small flaws can do more harm than good, bring extra costs and risks may show up for personnel.

## **2.6. Fracture Mechanics**

Fracture mechanics is categorized into two categories mainly, linear-elastic fracture mechanics (LEFM) and elastic-plastic fracture mechanics (EPFM). LEFM is developed based on stress intensity factor ( $K$ ) and yielding at the crack tip is assumed as small and material is in plane strain condition. On the other hand, EPFM is based on non-linear behavior which cannot be investigated via LEFM. Materials which have high toughness and ductile, work under plane stress condition and slow loading rates. Figure 2.16 shows the yielding conditions based on these fracture mechanics approaches.

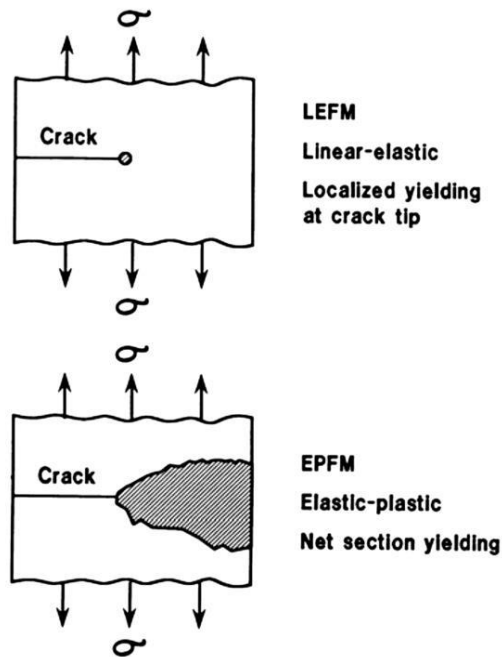


Figure 2.16. Yielding conditions based on LEFM and EPFM [30]

The experimental studies and standardizations of fracture toughness play an important role in the application of fracture mechanics in terms of fitness for service, damage tolerant designs, structural integrity assessments, residual strength analysis [31].

Some studies have been conducted on plastic zone existing at the tip of the advancing crack about the correction of K factor. To characterize the deformation before severe crack propagation the plastic zones are inspected. There are some conditions that affect the behavior around the crack tip. These conditions can be investigated by some EPFM parameters such as crack tip opening displacement, J-integral, crack opening angle, crack tip work, and crack tip force. The term fracture toughness is described as the resistance of materials to crack propagation [31]. Fracture behavior can be described using fracture toughness values as K, J and  $\delta$  values.

K, stress intensity factor, is proposed by Irwin in 1957 [32] and it is described the intensity of the elastic crack-tip fields. It is used when the singularity zone is larger than the plastic zone at the crack tip and it is strongly dependent to crack size and stress.  $K_{IC}$ , plain strain fracture toughness, can be measured when there is an only elastic region at the crack tip, no plastic-zone. To define  $K_{IC}$ , there should be a slow loading rate under linear elastic conditions. The stress distribution ( $\sigma_{ij}$ ) near the crack tip can be predicted with below equations (5) and (6), in polar coordinates ( $r, \theta$ ).

$$\sigma_{ij} = \frac{K_I}{\sqrt{2\pi r}} f_{ij}(\theta) \quad (5)$$

$$r_y = \frac{1}{2\pi} \left( \frac{K_I}{\sigma_{ij}} \right) \quad (6)$$

Generally, pipelines work under large scale axial plastic loads and these loads create plastic deformation at the crack tip. Consequently, welded and fabricated line pipes are needed to be characterized by using EPFM. This can be done with determining the fracture toughness via J-integral and CTOD methods.

The J-integral method was proposed by Rice in 1968 [33] and it is used in case of non-linear fracture behavior of the materials that there is a strong plastic deformation at the crack tip. The fracture toughness is determined with the help of plasticity theory. A new measurement method and the term J-integral is needed. The J-integral parameter is calculated by the equations (7) and (8),

$$J = \oint_r \left( W dy - T_i \frac{\partial u_i}{\partial x} ds \right) \quad (7)$$

where W is the strain energy density function and T is the surface traction vector.

$$J = \left[ \left( \frac{S}{W} \right) \frac{F}{(BB_N W)^{0.5}} g_1 \left( \frac{a_0}{W} \right) \right]^2 \left( \frac{1-\nu^2}{E} \right) + \left[ \frac{2U_p}{B_N(W-a_0)} \right] \left[ 1 - \left( \frac{\Delta a}{2(W-a_0)} \right) \right] \quad (8)$$

where  $S$  is the span length in the test,  $w$  is the width of the specimen,  $F$  is the applied force,  $B$  is specimen thickness,  $B_N$  is the specimen net thickness between side grooves,  $g_1(a_0/W)$  is stress intensity factor,  $a_0$  is initial crack length,  $\nu$  is Poisson's ratio,  $E$  is elastic modulus,  $U_p$  is plastic component of the area under load versus load-point displacement curve and the  $\Delta a$  is the stable crack extension including blunting.

In 1963, a new fracture mechanics parameter, CTOD, is proposed by Wells and it is represented as  $\delta$  [34]. It is used as  $K$  or  $J$  in practical applications. Initially, it is referred as crack opening displacement (COD), but after that, its name has been changed to CTOD to differ the quantity from the crack mouth opening displacement (CMOD) which is a physical crack opening displacement measured at the crack mouth at the specimen surface [31]. The CTOD approach is developed to broaden the LEFM to EPFM by implementing Irwin's plastic zone estimation and the elastic displacement solutions. The CTOD ( $\delta$ ) can be approximated according to the equation (9),

$$\delta = \frac{K_I^2}{E\sigma_{ys}} \quad (9)$$

for the center-cracked infinite plate in tension for far less applied stresses than the yield strength.

In the ASTM E1820-1 [35], CTOD is calculated according to the equation (10):

$$\delta = \frac{J}{m\sigma_Y} = \frac{1}{m\sigma_Y} \left[ \frac{K^2(1-\nu^2)}{E} + J_{pl} \right] \quad (10)$$

where  $K$  is stress intensity factor,  $J_{pl}$  is plastic component of  $J$  and  $m$  is:

$$m = A_0 - A_1 \left( \frac{\sigma_{ys}}{\sigma_{ts}} \right) + A_2 \left( \frac{\sigma_{ys}}{\sigma_{ts}} \right)^2 - A_3 \left( \frac{\sigma_{ys}}{\sigma_{ts}} \right)^3 \quad (11)$$

$$A_0 = 3.18 - 0.22 \left( \frac{a_0}{W} \right) \quad (12)$$

$$A_1 = 4.32 - 2.23 \left( \frac{a_0}{W} \right) \quad (13)$$

$$A_2 = 4.44 - 2.29 \left( \frac{a_0}{W} \right) \quad (14)$$

$$A_3 = 2.05 - 1.06 \left( \frac{a_0}{W} \right) \quad (15)$$

where  $\sigma_{ys}$  is the yield strength and  $\sigma_{ts}$  is the tensile strength.

There are several factors that fracture toughness depends on such as the material itself, fabrication route, environmental effects and loading rate. The most important factor among them is the material. Chemical composition, production method, microstructure and fabrication method of the material affects the fracture toughness significantly. During welding, the change of a parameter changes the microstructural evolution entirely. Heat input is the most effective parameter in welding that affects the fracture toughness since it is responsible for heating and cooling of the welding and consequently the final properties. For instance, lower heat inputs yield high cooling rates and reduce the average grain size and, generally, improves mechanical properties. However, high cooling rates may cause entrapping of some elements. If these entrapped elements are too strong compared with the surroundings they act as stress concentration regions and may cause local weak points in terms of fracture toughness, decreases toughness and ductility.

## CHAPTER 3

### EXPERIMENTAL

#### 3.1. Parent and Filler Metals

Parent material was an API grade pipeline steel with a thickness of 19.45mm. Material was obtained from one of the world's biggest steel producer POSCO(South Korea) (lot number SP48904) in plate form and by the HRB132860 qualification record, it is confirmed by the supplier as API 5L X70M PSL2 grade line pipe steel.

The plate was sectioned and subjected to material verification. The material's optical emission spectral analyses are found to be consistent with the certificate as per the standard EN 10204 type 3.1 (Table 2.2). The material was also verified with respect to the mechanical properties which are specified by the standard API 5L. The optical emission spectral analysis procedure is described in Section 3.3. The material also sectioned and machined to 12 mm thickness for welding fabrication.

A mild steel solid filler wire is used as a filler material while performing welding operations. Welding wires were taken from ESAB, which is worldwide welding equipment and consumable supplier. Welding wire used was 1.2mm diameter SFA/AWS A5.18 ER70S-6 (lot number PV534031289B) in GMAW operations. Chemical composition of the filler material is given in the Table 4.2.

The ductile-to-brittle transition (DBTT) behavior of the base material was previously investigated via Charpy impact test in a temperature range between -78°C and -32°C

[36]. The results can be seen in Figure 3.1. API 5L requirements for Charpy impact values were satisfied.

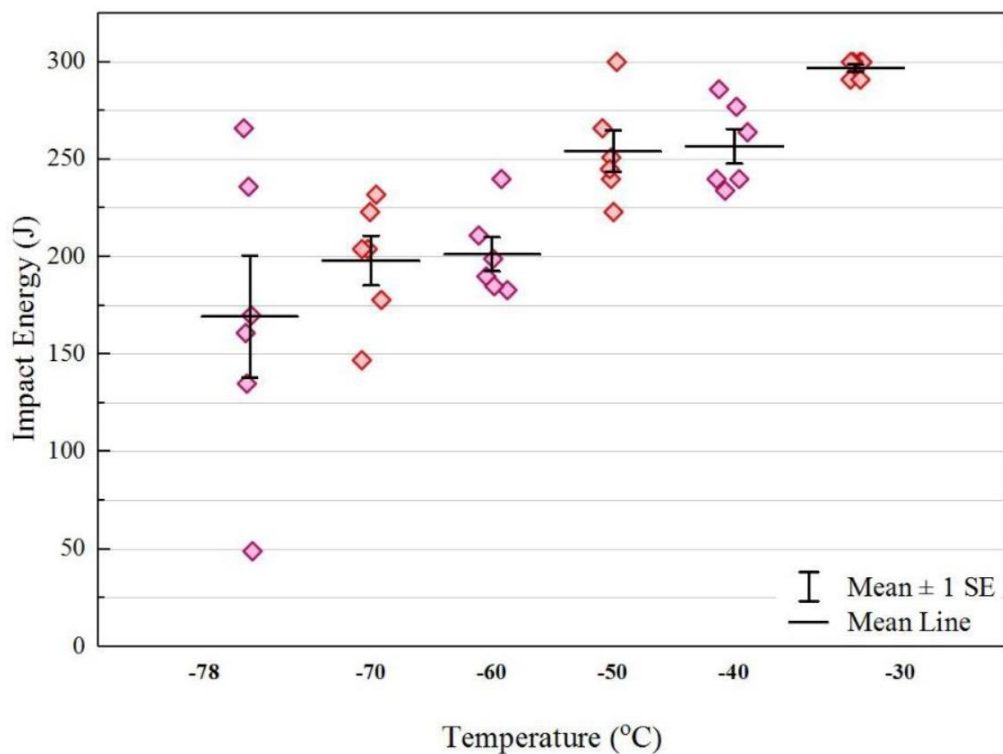


Figure 3.1. DBTT behavior of base metal API 5L X70M [8]

### 3.2. Welding Procedures

Construction of the pipelines in the field with girth welding is done automatically with mechanized welding machines (see Figure 3.2). This requires carefully designed pass sequences and bevel designs since the welding operation is done in different positions such as over-head, horizontal, and vertical during horizontal pipe fixed position weld. Typical heat input and pass sequences of a girth weld done in the field for 19.45 mm thick pipes are 0.60-0.65 kJ/mm and 8 to 10 passes.



Figure 3.2. CRC- Evans P-625 Computerized welding machine [37]

The plates going to be welded are positioned flat and then joined with GMAW via a welding robot. The plates were aligned on the platform of the welding robot and clamped by the aid of pneumatic cylinders. After that, the welding robot is programmed with respect to the welding route, i.e. the start and finish points of the weld, and linear welding speed. After setting up the robot, welding was performed. Welding setup can be seen in Figure 3.3.

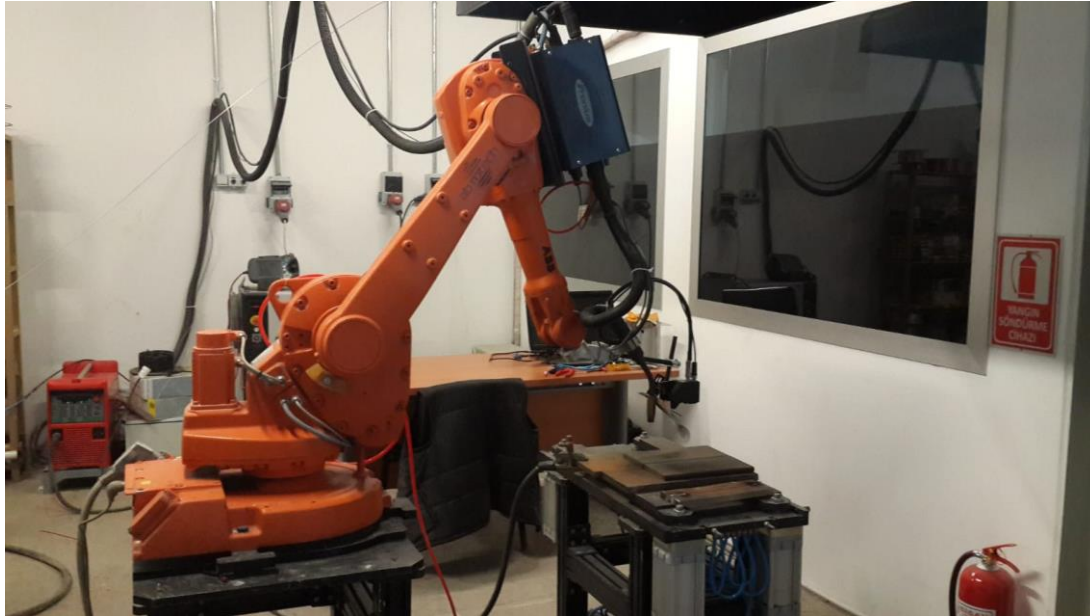


Figure 3.3. Welding robot setup for the GMAW and HPAW technique used in the thesis

A shielding gas mixture of Argon-18%CO<sub>2</sub> was used during the welding operations to protect the welding pool from the atmosphere. The shielding gas was supplied with a rate of 12 to 14 L/min.

The welds were done single-sided. 1.2mm diameter SFA/AWS A5.18 ER70S-6 welding wire is introduced to the 37.5 ° V-groove bevel to ensure the sidewall fusion. Three different heat input values were chosen. The first one was chosen as 0.65 kJ/mm, the lower limit of our study, to simulate field girth welding operations. Lower heat inputs can cause lack of fusion problem. The second one was chosen from a study done by our colleague Cagirici [36]. In that study, 12 mm thick plates were weldable in single pass and the minimum heat input to weld that thickness is 1.4 kJ/mm. So the second and the upper limit of our study was chosen as 1.4 kJ/mm. The last one was chosen as 1.1 kJ/mm as we want to observe how M-A changes as primary austenite grain sizes (PAGS) change with grain coarsening in CGHAZ. The 12 mm thick

weldments were completed with 6 and 10 passes with respect to the welding parameters and heat input. Welding parameters of the welds are given in Table 3.1 and Table 3.2.

Table 3.1. Welding parameters for the high heat input

Pass	1st Weld (6 passes)			
	Current (A)	Voltage (V)	LWS (mm/min)	Heat Input (kJ/mm)
Root	80	16	91	0.84
Hot	200	19	420	0.53
Fill (1-3)	220	21	197	1.42
Cap	230	24	312	1.05

Table 3.2. Welding parameters for the low heat input

Pass	2nd Weld (10 passes)			
	Current (A)	Voltage (V)	LWS (mm/min)	Heat Input (kJ/mm)
Root	80	16	100	0.78
Hot	190	19	525	0.4
Fill (1-6)	216	21	431	0.64
Cap (1-2)	230	22	467	0.66

To inspect the heating and cooling of the weldments, temperature measurements were done via bead-on-plate welding method. High-temperature thermocouples were used. To define the positions of the thermocouples, welding was performed and the width of the welds were noted. Then, thermocouples were spot-welded to the plates with 1 mm apart from the cap of the weld and measurements were done during welding operations with three different heat inputs with respect to the original welds. Welding parameters can be seen in Table 3.3, Table 3.4, and Table 3.5.

Table 3.3. Welding parameters simulating the heat input of 1.4 kJ/mm

Weld No.	Pass	Current (A)	Voltage (V)	LWS (mm/min)	Heat Input (kJ/mm)
1	1	286	24	240	1.37

Table 3.4. Welding parameters simulating the heat input of 1.15 kJ/mm

Weld No.	Pass	Current (A)	Voltage (V)	LWS (mm/min)	Heat Input (kJ/mm)
2	1	284	24	300	1.09
2	2	301	23.9	300	1.15

Table 3.5. Welding parameters simulating the heat input of 0.65 kJ/mm

Weld No.	Pass	Current (A)	Voltage (V)	LWS (mm/min)	Heat Input (kJ/mm)
3	1	293	24	540	0.63
3	2	309	23.9	540	0.66

### 3.3. Elemental Analysis

Generally, elemental analysis is done to ensure that the chemical composition of the metals comply with the specifications. In this study it was done by optical emission spectroscopy according to ASTM E415 [38] on both parent and weld metal. An electrical discharge forms between the material and the electrode, high voltage source, of the analyzer due to electrical potential between them. The discharge excites the atoms of the specimen which then emit characteristic optical emission lines. These characteristic lines are separated according to their wavelengths and a detector measures the intensity of each. Lastly, the computing unit processes the acquired data from the detectors and gives the element concentrations.

### **3.4. Confirming the Integrity of Weldment**

According to the requirements of the standards API 5L and API 1104 integrity confirmation assessments and procedure qualifications were done on the weldments. These requirements include both non-destructive testing (NDT) and destructive testing.

Visual inspections of the welds were done after the welding. To support these visual inspections and to examine the weld surface for possible defects, magnetic particle testing was applied. The radiographic inspection was applied to the weldments to confirm the integrity of the joints via X-ray and the images are recorded to radiographic films digitally. Phosphorus imaging plate (IP) has some advantages over conventional radiographic films such as image quality and reduces process times and due to its advantages, a phosphorus imaging plate (IP) was used for recording X-ray examinations. The tests were done according to ASTM E2007 [39] and ASTM E1742 [40], and evaluation of the radiographic films was done in terms of the requirements and the definitions of ASME BPV Code Section IX [41]. 2% quality level was employed for radiography (2-2T IQI).

Following the completion of the non-destructive tests, the weldments were sectioned and subjected to various tests.

Side bend tests, which is a very simple and easy method to evaluate the soundness of the weld, were done to the welded plates in order to check whether a linear defect exists or not. 180° bending specimens were prepared and tested according to ISO 5173 [42] as specified in API 1104 [1].

Cross weld (transverse) tensile tests were done according to ISO 4136 [43] and API 1104 [1] to determine the imperfections in the welded area which may cause a fracture.

Ultimate tensile strength and position of the fracture were noted for information only since there are different areas with dissimilar properties in the direction of tensile force, measurements such as yield strength, % elongation, and reduction of area are unreliable and inaccurate.

Macro examinations were done according to ISO 17639 [44] to see the general structure of the joints, i.e. weld metal, fusion zone, and base metal. Specimens were ground up to 1000 emery paper and then polished. 10% Nital was used as an etchant to reveal the weld macrostructure.

### **3.5. Microstructural Characterization**

Along with the macro hardness tests according to API 1104, microhardness tests were performed at specific locations at room temperature to examine the variations in the hardness and identify the LBZs. Macro hardness examinations were done with the Vickers indenter. HV10 method was used with an applied load of 10kgf. After macro examination, etched surface reveals HAZ, WM and BM regions of the weld and measurements were done with a distance of 0.5 mm between each indentation in HAZ region, at least 0.5mm in the WM and BM regions. Schematic representation of the hardness measurements can be seen in Figure 3.4. 45 indentations and hardness measurements were done for one specimen in total in 3 rows; two of them were near to the root and cap sides, one of them was at the mid-thickness. Root and cap side rows were 2 mm away from the flattened surface of the specimen.

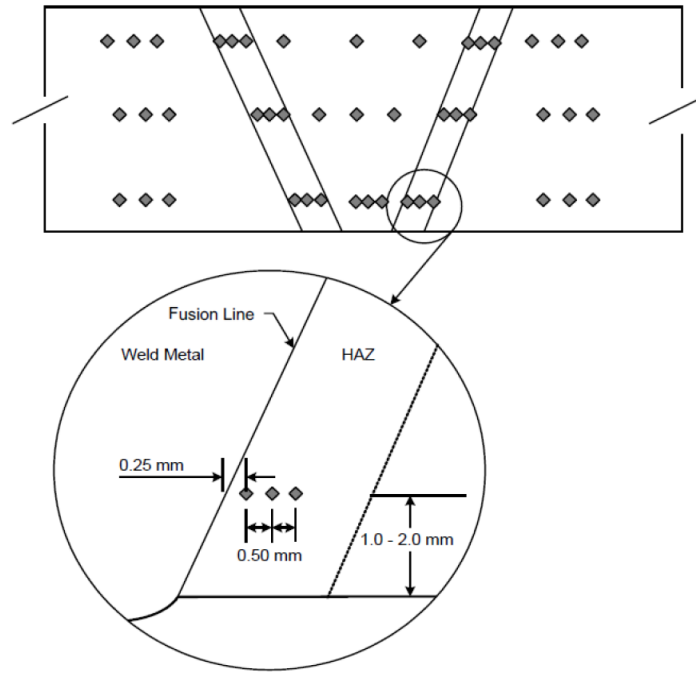


Figure 3.4. Schematic representation of hardness indentations [39]

Vickers hardness measurements are done with respect to the equation given below

$$HV = 0.102 \frac{2F \sin(136^\circ)}{d^2} = 0.1891 \frac{F}{d^2} \quad (16)$$

F is the test force in Newton (N), d is the arithmetic mean of the two diagonals of diamond-shaped indent in millimeters (mm).

Before micro-hardness measurements, specimens were prepared as before in macro-hardness specimens. They were ground, polished and etched. Additionally, specimens' flatness was measured with a coordinate measurement machine (CMM).

A region consists of WM, FZ, and HAZ was investigated. The load is chosen as 0.5 kgf (HV0.5) and indentation duration for the measurements was 10 seconds.

Microstructural constituents were characterized by metallography. Base metal, fusion zone, and weld metal were examined under LOM and SEM with different etchants. After sectioning, specimens were subjected to a preparation procedure starting with surface grinding to ensure the flatness of the specimen, small specimens were mounted in Bakelite for the same purpose. Then macro examination specimens were ground with SiC emery papers starting from 80 to 1200 and etched with 10% Nital solution to reveal the macrostructure. Micro examination specimens were further ground up to 2000 SiC emery paper and then polished with 6, 3 and 1  $\mu\text{m}$  Diamond colloidal. After that, the specimens were etched with 2% Nital solution. Further investigations were done with LePera [45] etchant application to the specimens. The specimens were prepared according to the above procedure and etched with 2% Nital to remove any disturbed metal.

In LOM and SEM, grain size measurements were done according to ASTM E112 [46] in BM and HAZ regions. Energy dispersive spectroscopy (EDS) was used in order to detect the elemental differences on different microstructural features at FZ and HAZ regions according to ASTM E1508 [47].

Nano-indentation is a valid instrument to understand the mechanical properties of materials such as elastic modulus, hardness, and dislocation motion which are very hard to inspect in nano and micro scales. The nano-indentation process is generally performed with a three-sided pyramidal Berkovich diamond indenter tip (see Figure 3.6). During the process, a load displacement curve is generated (see Figure 3.5) and the contact point is determined via this data. After contacting with the sample, force

is started to increase linearly until the maximum force is reached and then the specimen is unloaded. The stiffness is measured at the initial point of unloading and from the load displacement data, elastic modulus and hardness are measured.

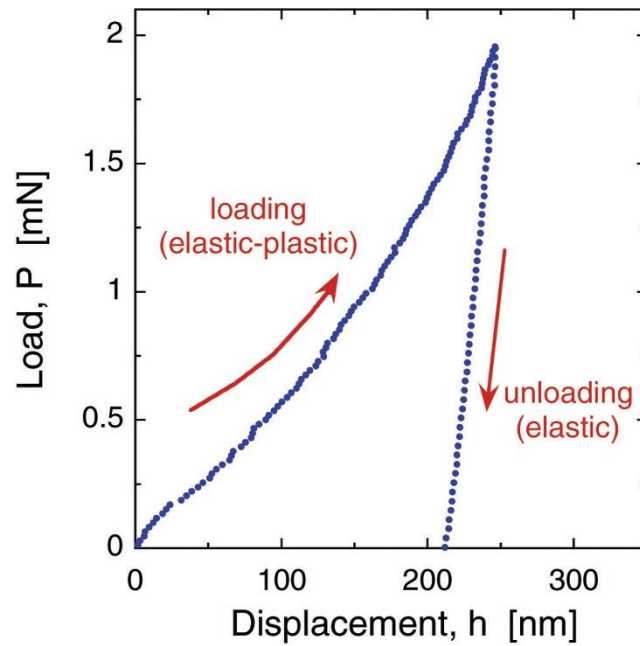


Figure 3.5. A representative load displacement curve of a nano-indentation process [48]

In this study, IRCGHAZ of the weldments were subjected to nano-indentations in order to investigate the M-A constituents. Since the indentation area is approximately seven times of the depth of the indentation 60 nm indentation depth was aimed according to the average size of the M-A constituents coming from LePera etched specimens and it was achieved with 5mN load. Nano-hardness measurements were also done before for a study conducted by our former research group member Cagirici [36]. Measurements were done on a weld in which hybrid plasma-arc welding (HPAW) technique was used with 1.4 kJ/mm heat input. Hardness variations between FZ and HAZ were investigated by a nano-indenter. In the base metal and HAZ, Berkovich nano indentations were applied using a sharp 3-sided indenter. Indentations

had at least  $10\mu\text{m}$  distance between them to measure micron-sized formations, i.e. M-A constituents [36].

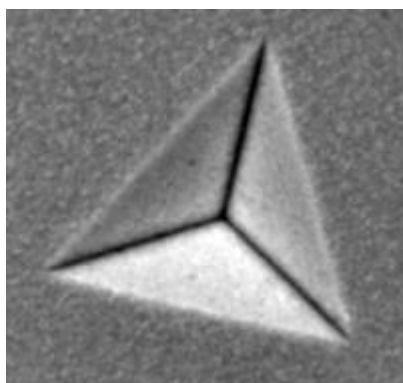


Figure 3.6. Berkovich nano-indenter trace after nano-indentation [49]

An indentation which is placed onto the M-A constituent, having steeper curve and low depth, can be seen in load vs. indentation depth diagram from Cagirici [36] (Figure 3.7).

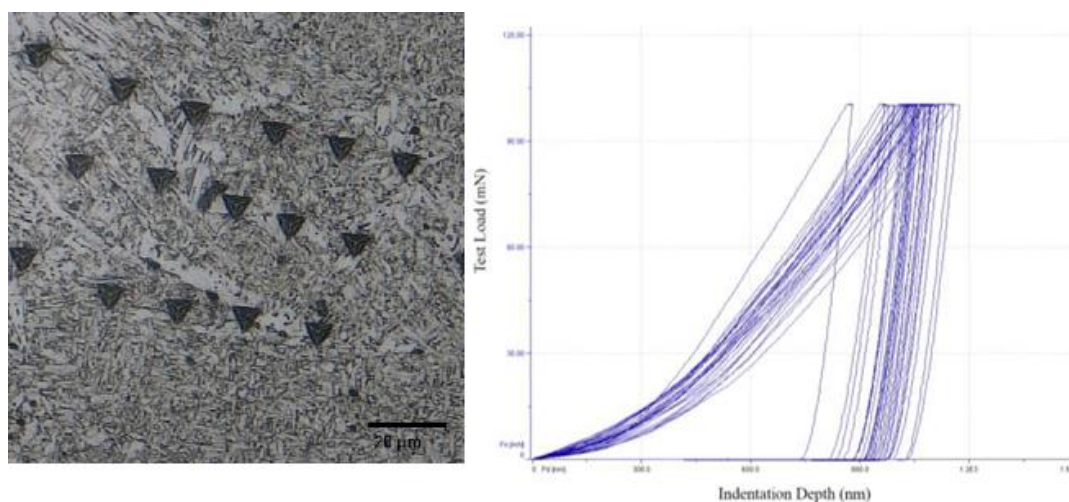


Figure 3.7. Nano indentations on specimen and load-indentation depth diagram [36]

### 3.6. Mechanical Characterization

The tensile test was performed with a Zwick/Roell Z250 universal test machine. The test speed was 0.6mm/min up to the yield point, and then, the speed was increased to 5 mm/min gradually.

All-weld tensile tests were done uniaxially to determine the strength and ductility of base metal and the weld metal. These tests were conducted at room temperature. ISO 6892-1 [50] was followed for the specimen geometry and the test procedure. Specimens had circumferential cross-section and dog-bone shaped. Tensile test specimen dimensions are given in Section 4.1. Reduced section diameter (d) was 6 mm and gauge distance ( $L_0$ ) was calculated from the formula below

$$L_0 = 5.65 \left( \frac{\pi d^2}{4} \right)^{1/2} \quad (17)$$

On the base metal, between -30°C to -78°C a DBTT survey was conducted by our group before. The specimen dimensions were 10mm×10mm×55mm. Charpy impact tests were conducted with 2mm V-notched specimens. Dimensions of the notch and the specimen were controlled by a micrometer and a Go / No Go gauge. Zwick/Roell RKP 450 impact testing machine was used for impact testing. Specimens were cooled in dry ice or in alcohol with the help of dry ice [36].

Apart from these all weld tensile and impact toughness tests, fracture toughness of the specimens were measured with elastic-plastic fracture toughness parameter,  $\delta$  (CTOD). The tests were conducted according to ISO 15653[51]. Since fracture toughness depends on different parameters such as the crack plane orientation, crack extension direction with respect to the rolling direction, grain flow, etc., the fracture toughness test samples can be extracted in different orientations with different crack

plane orientations. The standard has been developed a designation; N and P designate normal and parallel to weld direction, respectively and Q designates weld thickness direction. Figure 3.8 shows the crack plane orientations for fracture toughness specimens for weld metal.

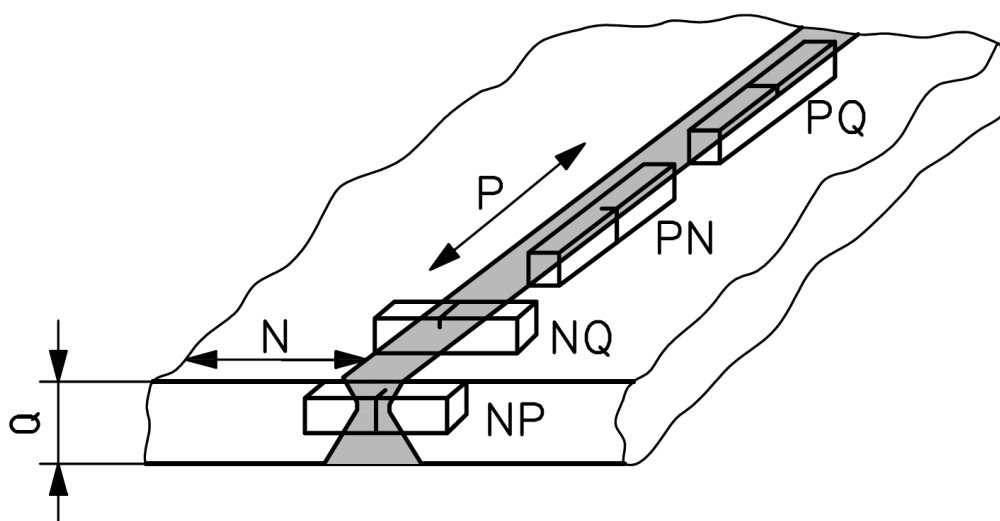


Figure 3.8. Crack plane orientation for fracture toughness specimens for weld metal [51]

Single Edge Notched Bend (SENB) specimens were extracted from the welds in NP orientation. The first letter of the designation indicates the direction normal to the crack plane and the second letter of the designation indicates the expected direction of crack propagation. Two sets of specimens, including three specimens per set, were extracted from the 1<sup>st</sup> and the 2<sup>nd</sup> weldments and machined down to 10mm×20mm×100mm (B-2B specimens) dimensions. Notch locations were selected as FL and the test temperature was -10°C. The notch locations were determined after an etching process with 10% Nital etchant on the specimen surface. Determined locations were marked and photographed. Integral type knife-edged (see Figure 3.9)



Specimens were then tested in accordance with the aforementioned related standards. Cross-head displacement speed was 0.7 mm/min in the tests in three-point bending test setup which can be seen in Figure 3.10. Span length was  $4W$  as stated in the figure. Crack opening displacement (COD) was recorded via a gauge placed on the notch and acquired load vs. COD graph was monitored. The tests were terminated when the load passed the highest peak or when there was a pop-in.

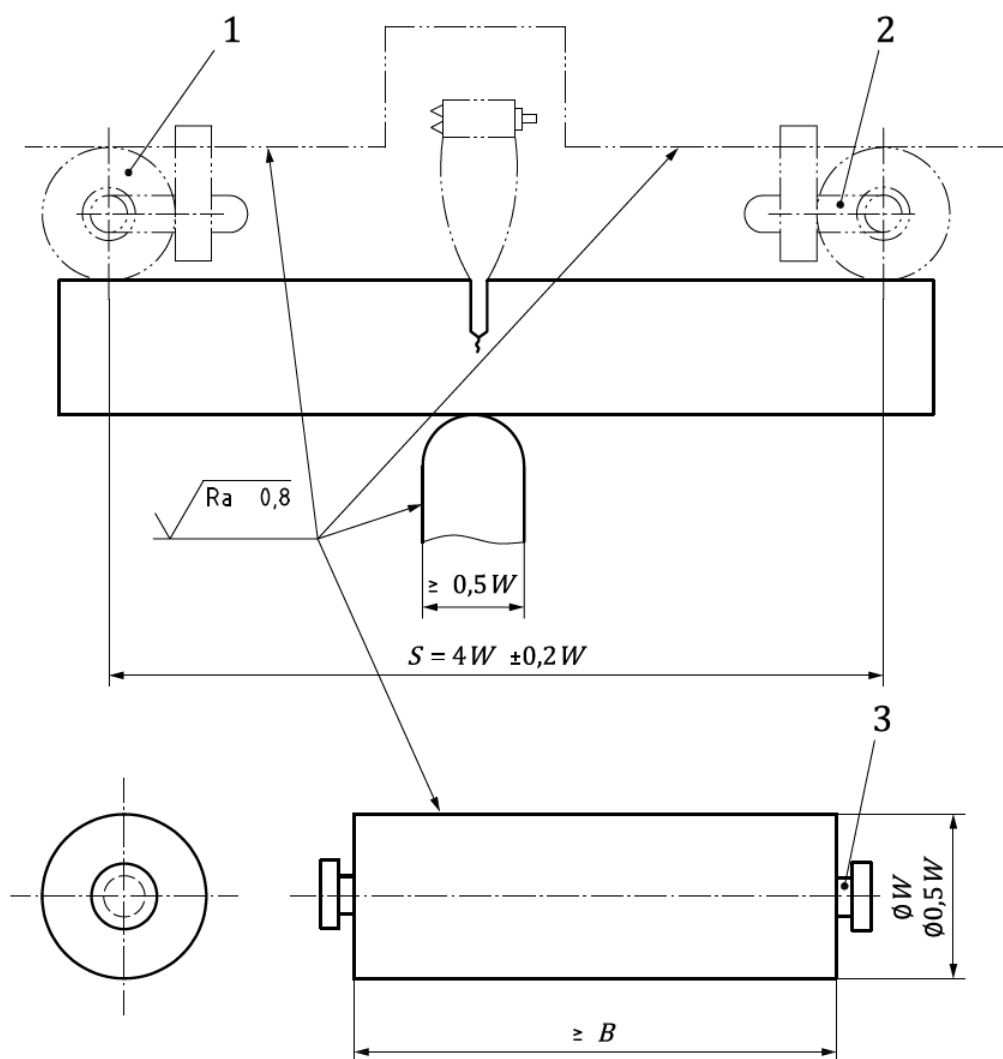


Figure 3.10. Three-point bending test setup [52]

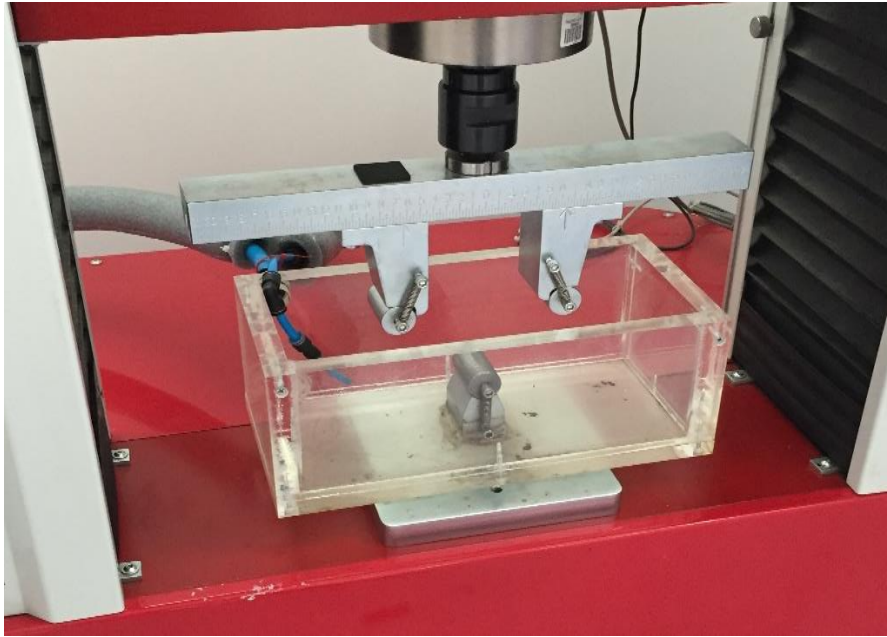


Figure 3.11. Experimental set-up for fracture toughness test

### 3.7. Post-Test Metallography and Fractography

After the CTOD tests, post-test metallography specimens were prepared according to the notch orientation to ensure the notches were located at FL. These specimens were mounted into Bakelite, and then ground, polished, and etched with 2% Nital solution. These specimens were further investigated via SEM.

Specimens were sectioned from the shiny fracture surfaces for fractographic investigation. To investigate the reasons behind the toughness variations, fractography was employed.

After the CTOD tests, the specimens were broken open with the aid of liquid nitrogen, below their DBTT, and its fracture surface examined to determine the original crack length and stable crack extension  $\Delta a$  that occurred during the test. Illustration of the

crack surface can be seen in Figure 3.12. Initial crack length,  $a_0$ , and  $\Delta a$  measurements were done according to the nine-point average method using the equation (18):

$$a = \frac{1}{8} \left( \frac{a_1 + a_9}{2} + \sum_{i=2}^8 a_i \right) \quad (18)$$

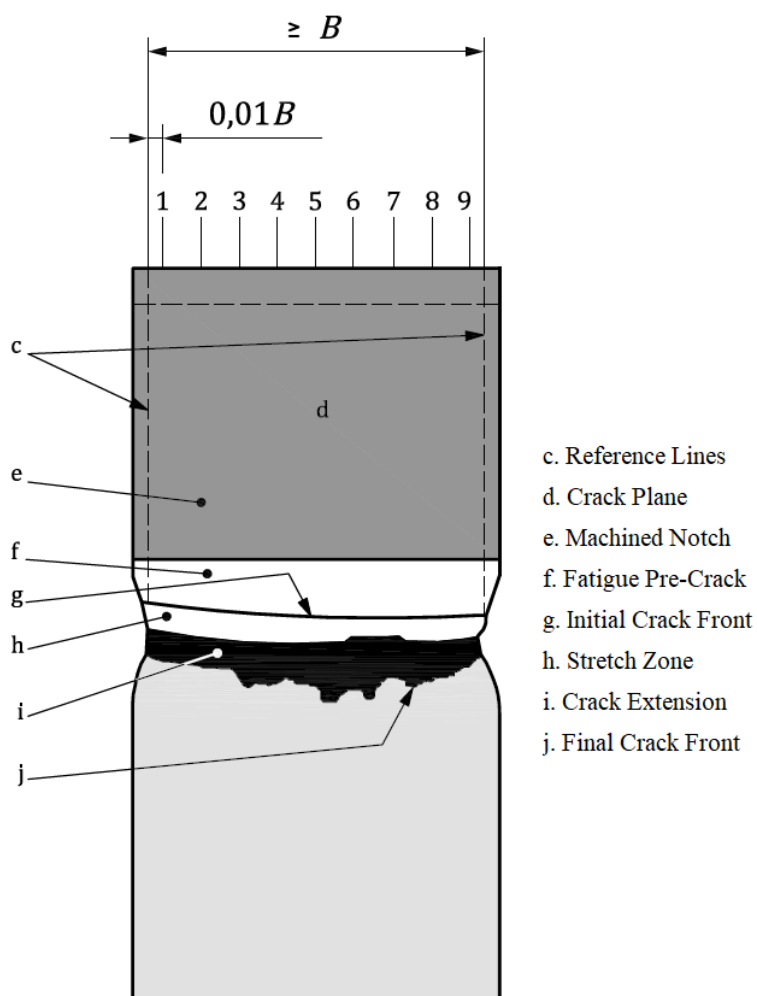


Figure 3.12. Schematic view of the specimen surface and measurements of crack lengths on specimens [51]

### 3.8. $\delta$ (CTOD) Parameter Calculations

Single parameter fracture toughness values in terms of CTOD was determined for FL specimens via CTOD testing. These values are sufficient in the assessment of fracture resistance to a located flaw, given in equation (19).

$$\delta_0 = \left[ \frac{S}{W} \cdot \frac{F}{(BB_N W)^{0.5}} \cdot g_1 \left( \frac{a_0}{W} \right) \right]^2 \cdot \frac{1-\nu^2}{2R_{p0,2}E} + \frac{0.4(W-a_0)}{0.6a_0+0.4W+z} \cdot V_p \quad (19)$$

$F$  and  $V$  are taken at the points depending on the test record types given in Figure 3.13. In types 1, 2, and 4, at fracture, in types 3 and 5, at the earliest pop-in prior to fracture, and in 6, when the test record exhibits a maximum force plateau, at maximum force.

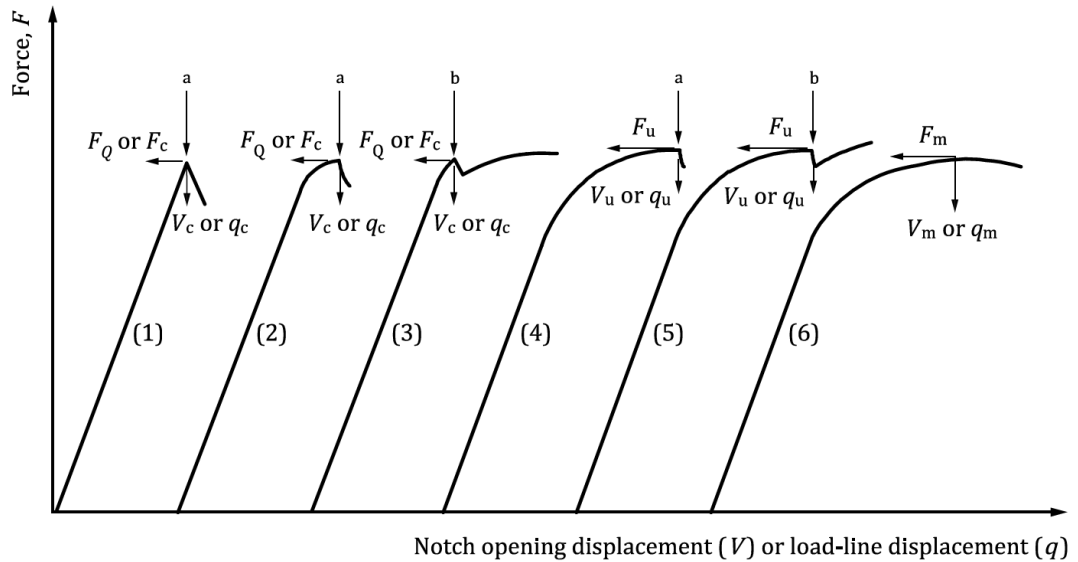


Figure 3.13. Different types of Force vs CMOD recordings [52]

$a_o$  was determined from the formula:

$$a_o = \frac{1}{8} \left( \frac{a_1 + a_9}{2} + \sum_{j=2}^{j=8} a_j \right) \quad (20)$$

In three-point bend specimens stress intensity factor  $g_1 \left( \frac{a_o}{W} \right)$  is calculated according to the equation (21).

$$g_1 \left( \frac{a_o}{W} \right) = \frac{3 \left( \frac{a_o}{W} \right)^{0.5} \left[ 1.99 - \frac{a_o}{W} \left( 1 - \frac{a_o}{W} \right) \left( 2.15 - \frac{3.93 a_o}{W} + \frac{2.7 a_o^2}{W^2} \right) \right]}{2 \left( 1 + \frac{2 a_o}{W} \right) \left( 1 - \frac{a_o}{W} \right)^{1.5}} \quad (21)$$

For all design of specimens,  $a/W$  ratio shall be in the 0.45 and 0.7 range for  $\delta$  determination and  $g_1 \left( \frac{a_o}{W} \right)$  values change between 2.29 and 5.85 with respect to the ratio. Some  $a/W$  ratios and corresponding  $g_1 \left( \frac{a_o}{W} \right)$  values are given in the Table 3.6.

Table 3.6.  $g_1 \left( \frac{a_o}{W} \right)$  values for three-point bend specimens

$\frac{a}{W}$	$g_1 \left( \frac{a_o}{W} \right)$
0.45	2.29
0.50	2.66
0.55	3.14
0.60	3.77
0.65	4.63
0.70	5.85

The plastic component of notch opening displacement,  $V_p$  was determined using a computer technique or manually according to Figure 3.14.

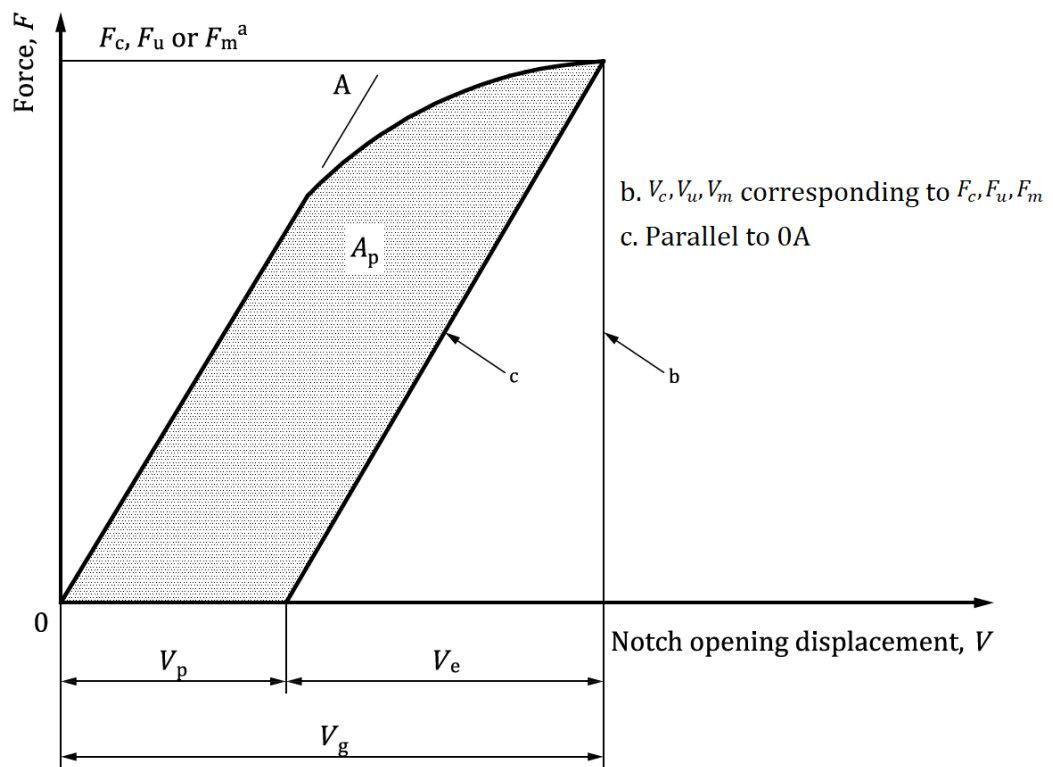


Figure 3.14. Definition of  $V_p$  (for determination of  $\delta$ ) [52]



## CHAPTER 4

### RESULTS AND DISCUSSION

Non-Destructive tests were applied to the welds and no major indication was observed i.e. welded joints has no flaws or the existing flaws are below NDT range. Some sputtering problems, pores and lack of fusion were seen as minor indications. Radiographic inspection results of the joints can be seen in Figure 4.1.

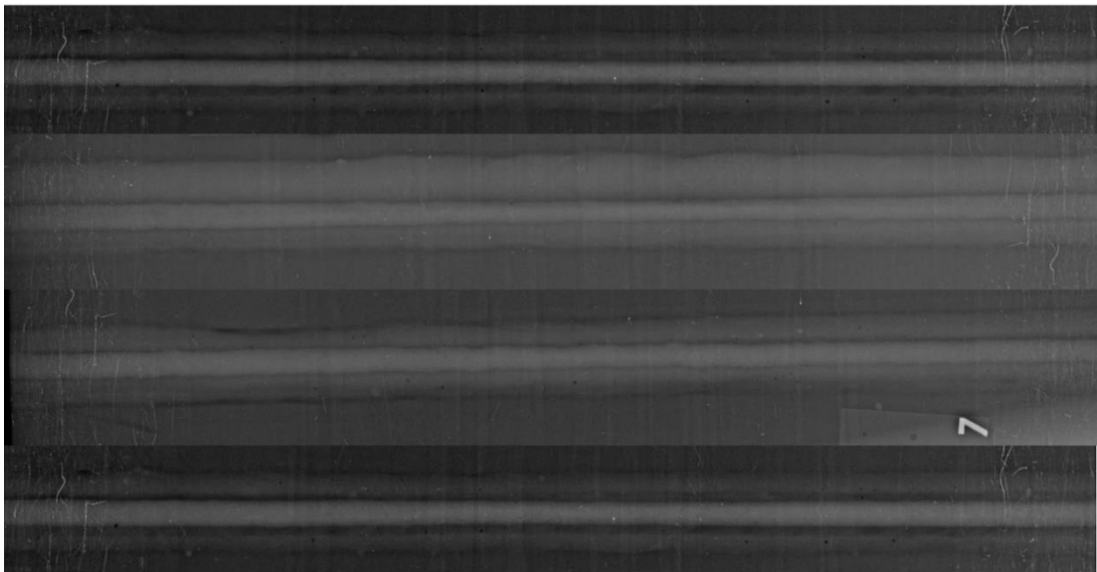


Figure 4.1. Radiographic inspection of welded joints

Destructive tests were done after NDT inspections. Cross-weld tensile test specimens prepared according to API 1104 [1] for weldments were tested to ensure the soundness of weldments. No imperfections were detected and they all failed from base metal

which means that the fusion zone, the most critical region of the weldments, has higher yield strength than the base metal. Additionally, side bend test specimens were prepared and tested to reveal internal defects. There were no major imperfections with respect to API 1104 [1].

The macrographs of the specimens can be seen in Figure 4.2, Figure 4.3. Figure 4.4. is taken from HPAW weldment that was done by Cagirici [36]. All of these welds were welded by single side welding procedures. Welds having 0.65 kJ/mm and 1.1 kJ/mm were welded in multiple passes after a hot pass on the root section. It needs to 10 successive weld passes to complete welding in 0.65 kJ/mm weld and 6 passes to complete 1.1 kJ/mm weld. The number and size of the passes are reasonable in both weldments with respect to their heat inputs. On the other hand, weld having 1.4 kJ/mm was welded in one pass with HPAW method. According to Ohm relation, decreasing arc length and increasing wire feeding rate give rise to current amplitude. An increase in current amplitude improves through thickness penetration and side wall diffusion. There is no lack of weld penetration and side wall diffusion in macro examinations. Even in the lowest heat input there is no trace of lack of fusion.

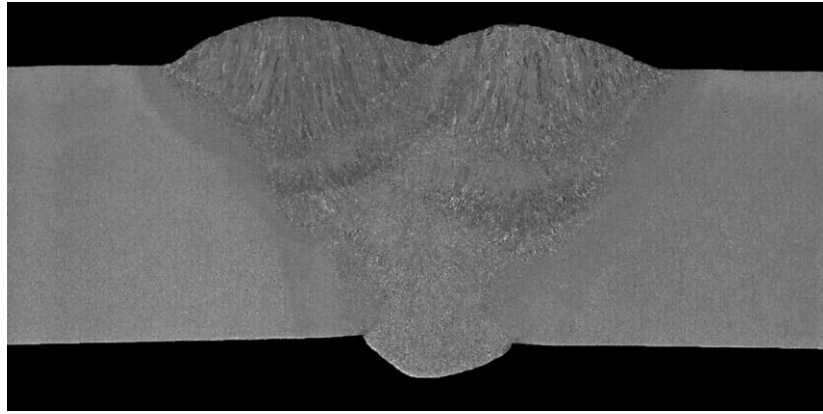


Figure 4.2. Macrograph of the weldment (1.1kJ/mm heat input)

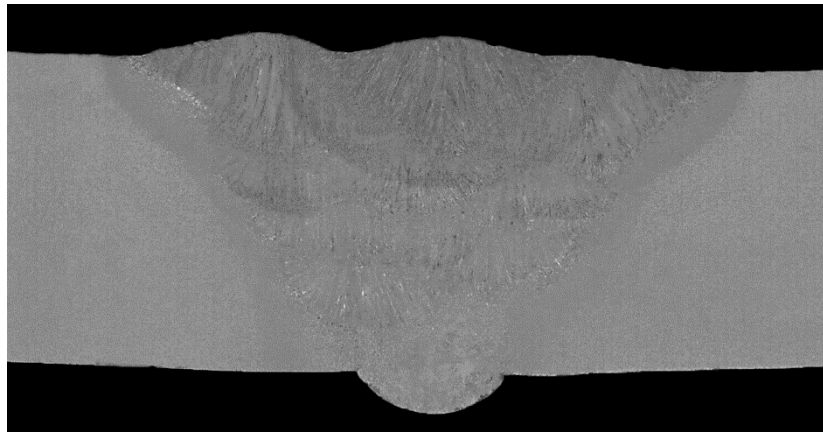


Figure 4.3. Macrograph of the weldment (0.65 kJ/mm heat input)

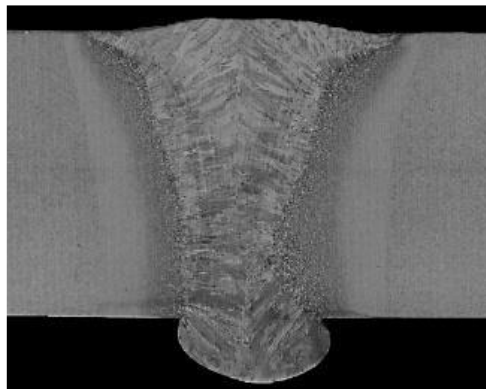


Figure 4.4. Macrograph of the weldment (1.4 kJ/mm heat input)

#### 4.1. Parent and Filler Metal Characteristics

Chemical composition of the base metal was inspected by optical emission spectroscopy and the results of the spectral analysis and values given in the standard are presented in Table 4.1. The results of the analysis seem to be compatible with the requirements of the standard and the certification document.

Table 4.1. API 5L X70M composition

		Weight Percent (%wt)										
X70M	Element	C	Si	Mn	P	S	Cr	Ni	Mo	Ti	Nb	V
	Std<	0.12	0.45	1.70	0.025	0.015	0.50	0.50	0.50	<0.15		
	Lab	0.07	0.38	1.63	0.006	0.003	0.23	0.02	0.11	0.02		

Table 4.2. Filler material composition

		Weight Percent (%wt)										
ER70S -6	Element	C	Si	Mn	P	S	Cr	Ni	Mo	Ti	Nb	V
	Std	0.07	0.95	1.68	0.025	0.035	0.15	0.15	0.15			
	Cert.	0.08	0.83	1.47	0.006	0.007	0.02	0.02	<0.001			
	Lab	0.08	0.90	1.51	0.014	0.014	0.07	0.02	0.02	0.01	0.02	0.01

In Table 2.3, frequently used microalloying elements and their effects were given. Titanium, Niobium, Vanadium and their compounds alters the microstructure of the steel, strengthen the ferrite matrix, and so do mechanical properties of it [4][53][54]. Lower V contents such as contents given in Table 4.1 and Table 4.2, promotes second phase particle and M-A constituent formations [55]. Acicular ferrite structure was expected because of the addition of these ferrite strengthener alloying elements. Lan et al. [10] states that in their work on Nb-Ti microalloyed pipeline steels, lower finish

rolling temperatures and the cooling stop temperatures leads the microstructure to change quasi-polygonal ferrite to acicular ferrite. This results in higher strength and higher toughness in material.

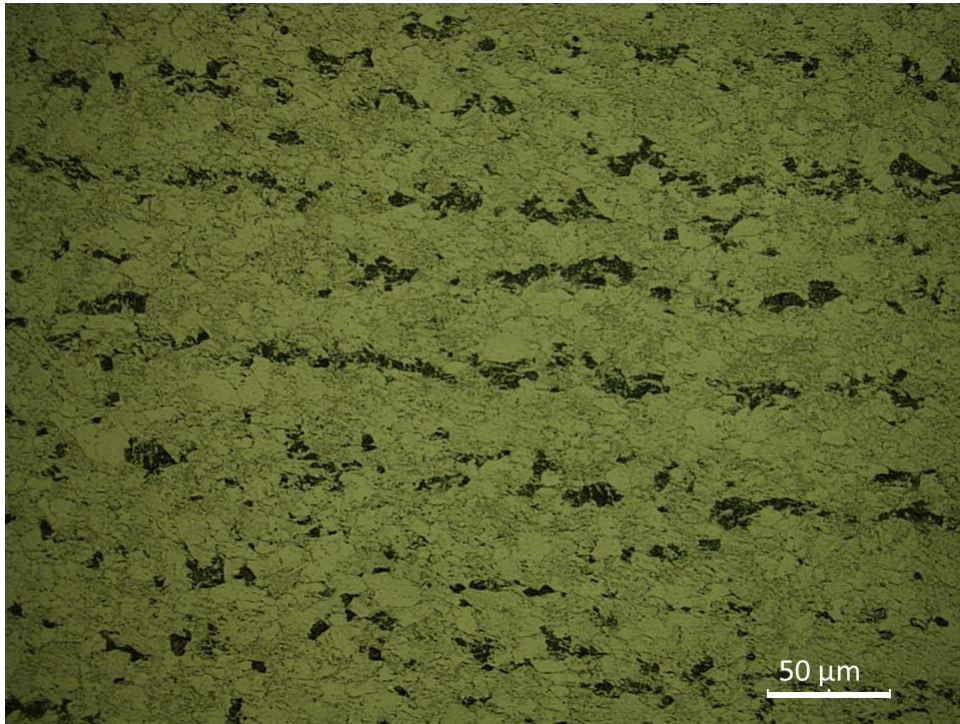


Figure 4.5. Banded structure of the base metal (2% Nital etched)

The base material has different microstructural features as a consequence of its alloying elements and manufacturing route. Banded structure exists and due to production method of the base metal.

The tensile test results of the base metal and all-weld tensile test results of the weldments are tabulated in Table 4.3. Weld metals have higher strength levels than base material which is a requirement of API 1104 standard.

Table 4.3. Tensile test results of base material and weldments

Specimen	Base Material	Weldments	
		High Heat Input	Low Heat Input
E (GPa)	205	205	207
Rp0.2 (MPa)	582	619	602
Rm	662	703	672
At (%)	21	18	23
RA (%)	63	43	52

Yield strength mismatch between the base metal and the weld metal is as 6.4% higher in high heat input weldment. On the other hand, the difference in yield strength is only 3.4% in low heat input weldment. Higher difference between the base metal and filler wire caused strong overmatching with respect to strength and ductility. This strength mismatch is done intentionally and optimized to give advantage to the fusion zone. This optimization process is called as strength over-matching. On the other hand, this mismatch generally cause a decrease in toughness in fusion zone and it has to be taken into consideration.

The strength of the base metal, weld metal and fusion zone influences the fracture toughness of the joint. Different notch depths and final crack tip locations, different  $a/W$  ratio, yield different CTOD values for the same material since mechanical properties are different in different weld regions and strain distribution around the crack tip is affected by it. In their work on CGHAZ of the weld Minami et al. [56] states that the actual CGHAZ toughness affects the fracture behavior of the weld. Brittle CGHAZ leads lower CTOD values because of promotion of local stresses in the CGHAZ due to limiting effect of overmatched WM and CGHAZ having moderate toughness produces higher CTOD values due to deviation of the crack growth path to the base metal. Since the CGHAZ has the lowest toughness across the fusion zone and

the tendency of crack propagation is away from the weld metal, a notch location close to the weld metal side represents the best condition for the initiation of an unstable fracture. Cracks' tendency to propagate through the CGHAZ promotes the participation of M-A constituents' brittleness to the fracture so do the deteriorative effect of them to the system.

#### **4.2. The Microstructure of HAZ**

Due to Nb, Ti and V contents of the steel the recrystallization temperature of carbides, nitrides, and carbonitrides of these elements changes. In their work, Zhou et al. [57], investigated Nb-Ti microalloyed steels having different amounts of Ti and N with respect to precipitation evolution during solidification. They impede cooling by quenching at different temperatures in austenite region. It was found that carbonitride precipitates were not exist in ingots having less than 0.011 wt% Ti down to 1100 °C, on the other hand Nb rich precipitates were present at 800 °C in mold-cooled ingots. For multi-pass welding, there exist heating and cooling cycles. During these cycles and according to temperatures reached the precipitation of carbides, nitrides and carbonitrides have importance. Hong et al. [58] investigated the evolution of Nb, Ti and V precipitates in HSLA steels during reheating. It is observed that dendritic Nb-rich carbonitrides exist in as-cast structure, which are stable below 1000 °C, and during reheating these particles experience a dissolution and re-precipitated to two different carbonitrides Ti and N-rich and Ti and C-rich. Ti and N-rich titanium and niobium carbonitride particles, (Ti,Nb)(C,N), precipitates along austenite grain boundaries primarily and then precipitation of Ti and C-rich (Ti,Nb)(C,N) particles occur within the austenite grains.

Single-pass welding operation results in different zones in the joint area (see Figure 4.6 and Figure 4.7):

- The fusion zone (FZ), where the mixing of both base metal and filler metal occurs. The temperature for this region is usually 1500 – 1600 °C.
- The partially melted zone (PMZ). In this region, the parent metal is melted partially. The corresponding temperatures in this area is between peritectic temperature and liquidus temperature.
- The coarse grained heat affected zone (CGHAZ) where peak temperature reaches temperatures not as high as to melt the metal but high enough to completely austenize the structure and growth of grains during the welding operation. The peak temperature is greater than 1100 °C for this region.
- The fine grained heat affected zone (FGHAZ). In this region the peak temperature is enough to austenize the region as in CGHAZ. However, the temperature is not enough for grain growth. This temperature is generally between  $A_{c3}$  and 1100 °C.
- The intercritical heat affected zone (ICHAZ). In this region, the temperature is in between  $A_{c1}$  and  $A_{c3}$ . As a result of it, the structure is transformed to austenite moderately.
- The tempered zone (TZ). In this region, temperature is below  $A_1$  and no transformation occurs. A tempering effect is observed.

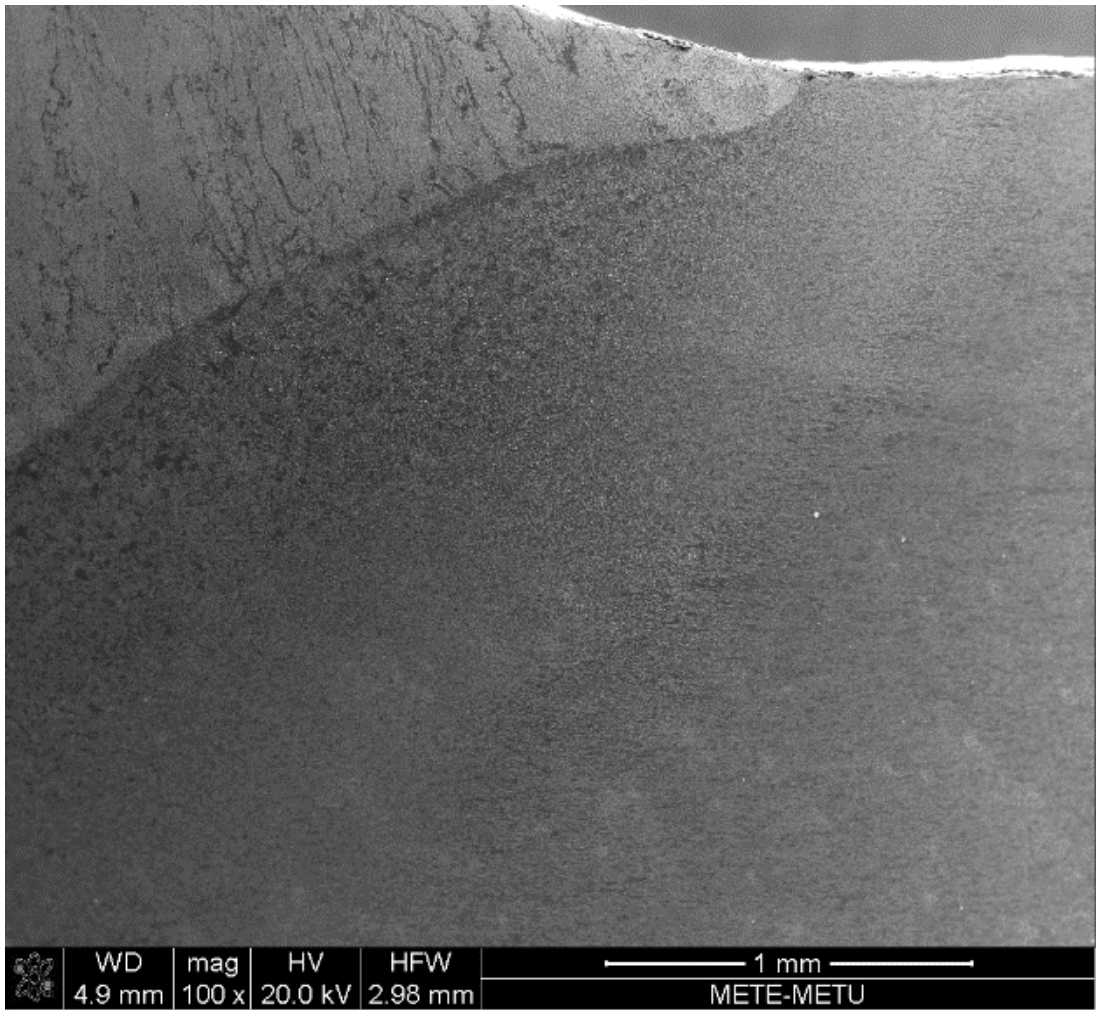


Figure 4.6. An overview to different zones formed during one pass welding

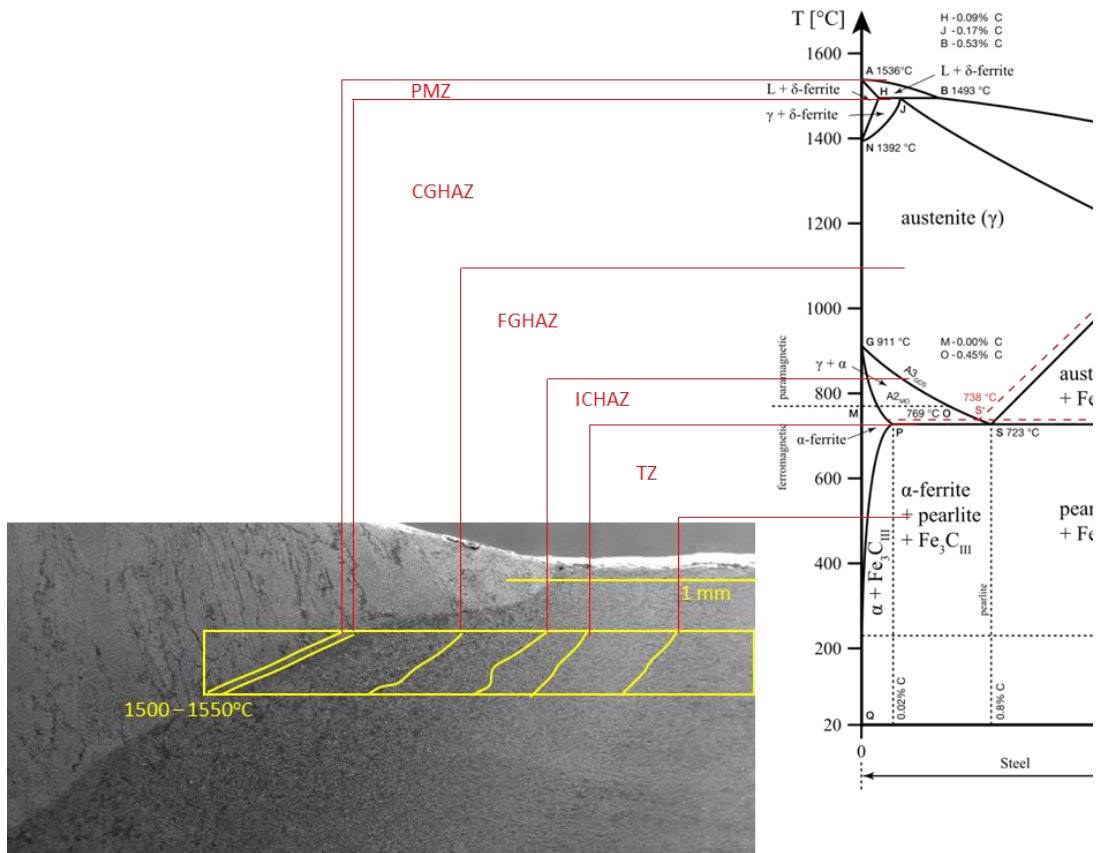


Figure 4.7. The HAZ regions of a welded joint, corresponding temperature ranges and relevant parts of Fe-C phase diagram

Altered microstructure of the base metal in single pass welding is shown for different locations in Figure 4.8 with micrographs. The microstructure changes with respect to induced heat and temperatures attained during welding operation. The changes in microstructure is more dramatic in fusion line and in the HAZ region where the temperatures reaches higher than  $A_{c1}$ .

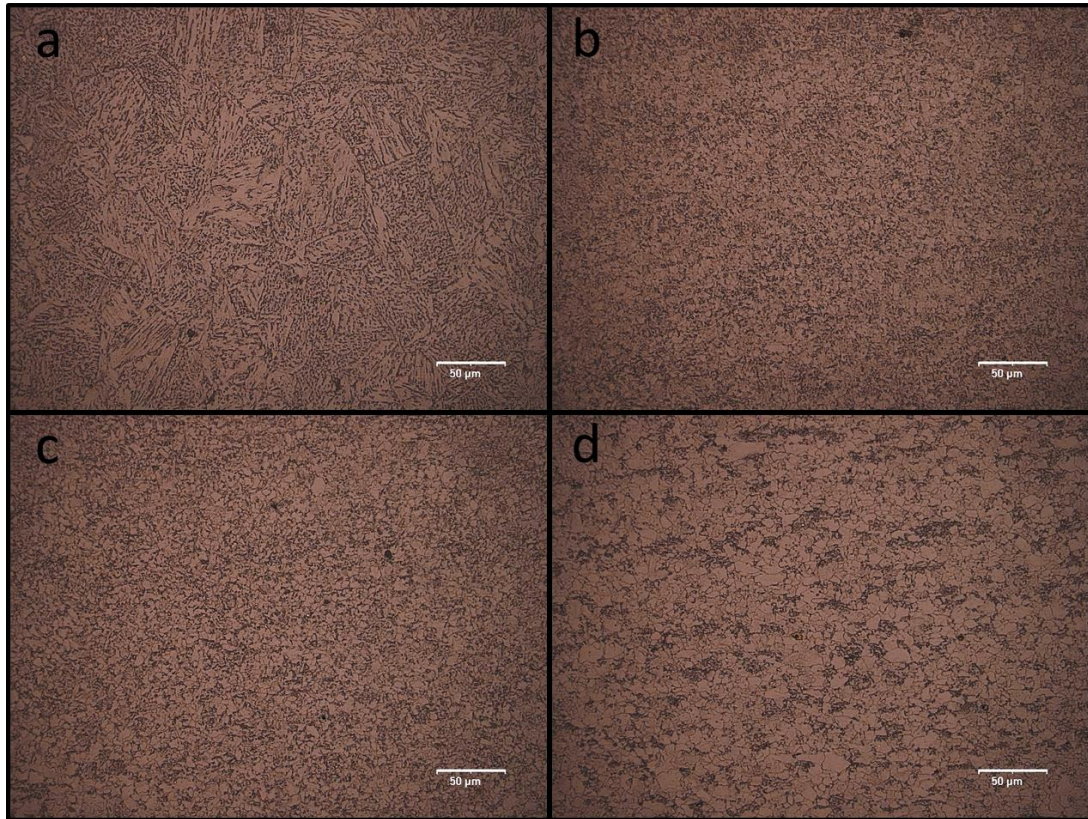
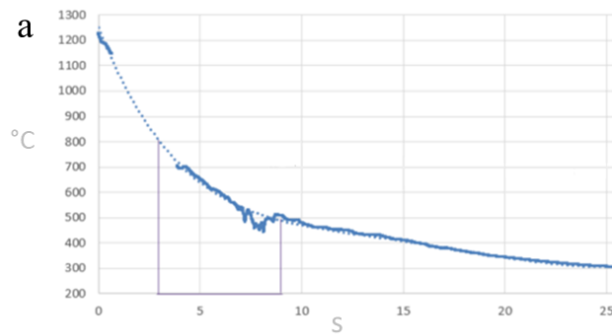


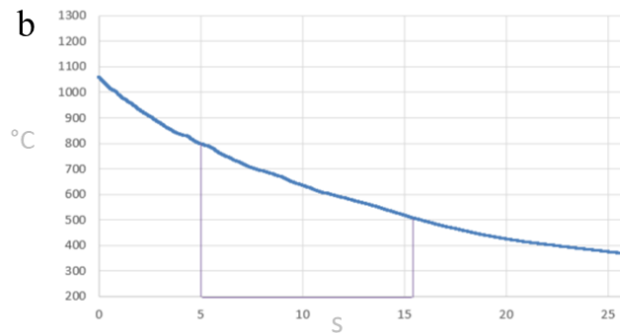
Figure 4.8. Different weld zone micrographs of 1.4kJ/mm heat input weld in 1000x magnification (etched by 2% nital) (a) Coarse grained heat affected zone (CGHAZ) (b) Fine grained heat affected zone (FGHAZ) (c) Intercritical heat affected zone (ICHAZ) (d) Tempered zone (TZ)

Figure 4.9 show the cooling curves of CGHAZ, FGHAZ and ICHAZ regions during welding. When both microstructure and cooling curves are investigated together the some correlations can be established. As it can be seen CGHAZ region (Figure 4.8a) reaches temperatures above  $A_{c1}$  and there is also enough time for grain growth a coarser grain structure is formed. FGHAZ cooling curve (see Figure 4.9b) implies the temperature is above austenitization temperature but there is not enough time for grain growth and this results in CGHAZ-like but finer microstructure (Figure 4.8b). The temperature attained in ICHAZ, between  $A_{c3}$  and  $A_{c1}$ , and the cooling regime (see

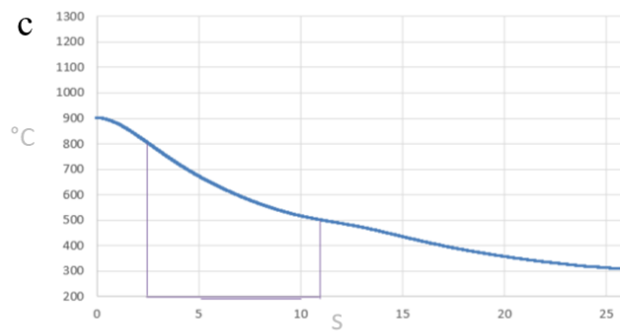
Figure 4.9c) result in moderately austenized structure (Figure 4.8c). In TZ (Figure 4.8d), the banded structure of the base metal is changed and a slight tempering occurs.



$T_p = 1225^\circ\text{C}$  (1100 – 1400°C)  
 $\Delta t_{8/5} = 11.9$  s



$T_p = 1057^\circ\text{C}$  ( $A_3 - 1100^\circ\text{C}$ )  
 $\Delta t_{8/5} = 10.2$  s



$T_p = 900^\circ\text{C}$  ( $A_1 - A_3$ )  
 $\Delta t_{8/5} = 8.4$  s

Figure 4.9. Cooling curves of different regions of weld obtained with thermocouples (TC) (a) CGHAZ region of one-pass weld (TC 0.2 mm away from FL) (b) FGHAZ region of one-pass weld (TC 1.2 mm away from FL) (c) ICHAZ region of one-pass weld (TC 1.7 mm away from FL)

The microstructure and properties of the HAZ is strongly affected by the austenite grain size and austenite grain sizes are affected by heat input in welds. Higher heat

inputs yield wider CGHAZ regions and coarser grain sizes and larger primary austenite grains decreases relative acicular ferrite ratio and results in harder microstructure [59]. Grain coarsening due to high heat input and wider HAZ region have detrimental effects on toughness. Primary austenite grain sizes measurements done according to ASTM E112 [46] in CGHAZ regions of different heat inputs are given in Table 4.4.

Table 4.4. Primary austenite grain sizes (PAGS) in CGHAZ region of welds having different heat inputs

Heat Input	Mean ( $\mu\text{m}$ )	ASTM Grain Size #	Standard Deviation ( $\sigma$ )	95 percent confidence Interval (95 % CI)	Percent Relative Accuracy (% RA)
1.4kJ. $\text{mm}^{-1}$	49.8	5.4	0.003	0.004	7.1
1.1kJ. $\text{mm}^{-1}$	21.4	7.8	0.002	0.002	11.3
0.65 kJ. $\text{mm}^{-1}$	15.0	8.8	0.001	0.001	9.3

Grain size measurements on CGHAZ shows that larger grain sizes are obtained for higher heat input. The largest CGHAZ grain size around 50  $\mu\text{m}$  corresponds to 1.4kJ/mm heat input. The 1.1kJ/mm heat input and 0.65 kJ/mm heat input yields the average grain sizes of 21  $\mu\text{m}$  and 15  $\mu\text{m}$  respectively.

Several factors affect development of the different microstructural features in the weld zone, fusion zone, and heat affected zone during welding. Among them, one of the most important parameter is the heating and cooling of the work piece. Heat flow in the welding is an important issue since phase transformations and the microstructure is strongly affected by it, so do the final properties of the weld.

Cooling rate is important on formation of microstructure in weld zone since diffusion is a temperature and time dependent phenomenon. As microstructure changes with cooling rate, the mechanical properties changes significantly [60]. Cooling rate between 800°C and 500°C ( $t_{8/5}$ ) is a determining factor on distribution and morphologies of primary and secondary phases in HAZ. Heat transfer conditions are governed by the heat input of the welding process and the pre-heat temperature as well. The cooling rates of the bead-on plate studies are given with respect to heat inputs in Table 4.5. Effect of heat input can be seen in Figure 4.12, as the given heat input increases, the cooling rate decreases [61].

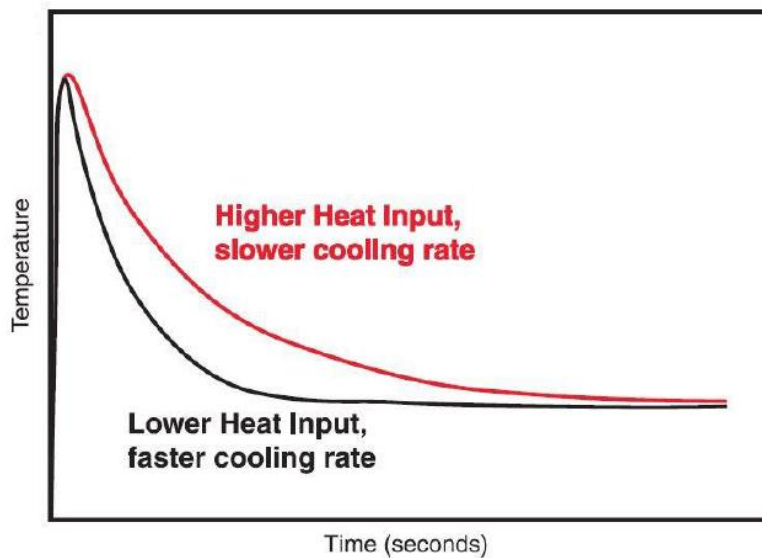


Figure 4.10. Effect of heat input on cooling rate [61]

Table 4.5. Cooling rates with respect to weld heat input (obtained from bead-on plate studies' temperature measurements)

HI, kJ mm <sup>-1</sup>	t <sub>8/5</sub> , °C s <sup>-1</sup>		PAGS	
	1 <sup>st</sup> pass	2 <sup>nd</sup> pass	µm	ASTM #
0.65	73	51	15.02	8.82
1.15	42	33	21.35	7.80
1.45	21	NA	49.78	5.36

When it is compared with literature, measured cooling rates are coherent in general. Different heat input and cooling rates obtained from literature are tabulated in Table 4.6. The difference between cooling rates are due to differences in the size of base metals used. However, in general, higher heat input values yields lower cooling rates.

Table 4.6. Heat input and cooling rates in literature

HI (kJ/mm)	<i>Cooling rate</i> °C		<i>Source</i>
		s <sup>-1</sup>	
0.9		60	Li et al. [62]
1		30	Shome et al. [63]
1		30	Andia et al. [64]
1		15	Poole et al. [65]
1.5		15	Zhao et al. [66]
2.35		7.79	Zhu et al. [22]
2.5		23	Kiran et al. [67]
2.5		5.35	Zhao et al. [66]
2.6		15	Hu et al. [68]

According to PAGES of the CGHAZ, continuous cooling transformation diagrams given in Figure 4.11, Figure 4.12 and Figure 4.13 were generated via software JMatPro [69]. Cooling curves of welds having 1.4kJ/mm, 1.1 kJ/mm and 0.65 kJ/mm were drawn with respect to the cooling rates (indicated with red lines).

Considering these cooling curves of the welds, higher martensite formation and retained austenite is expected in CGHAZ in welds having lower heat inputs. All of the welds crosses bainite start curves of the CCT diagrams. However, in terms of amount of the bainite phase in CGHAZ, higher input weld is one step ahead from the relatively low heat input ones. In CGHAZ, additional phase transformations such as upper bainite formation and M-A constituent formation occur with grain coarsening and weak points are formed during cooling.

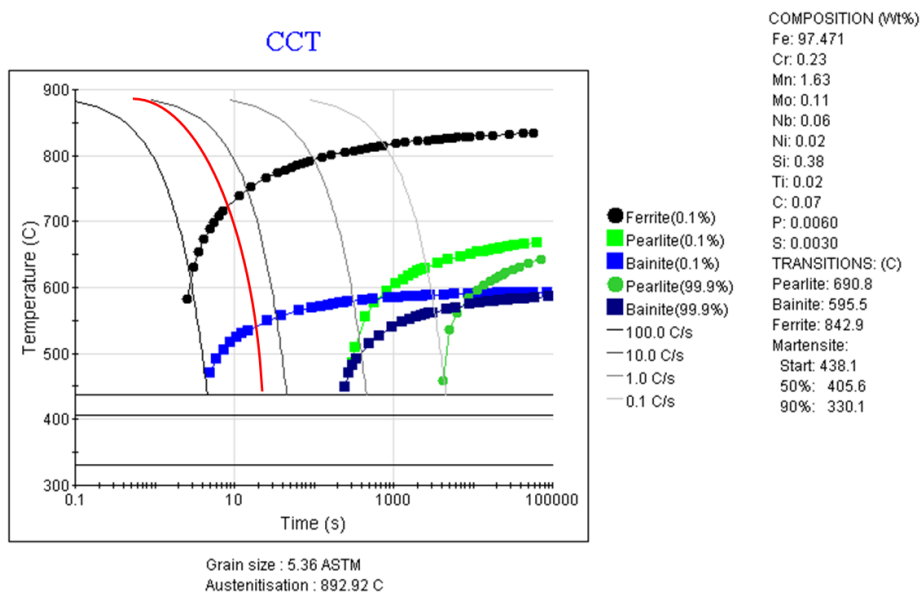


Figure 4.11. Continuous cooling transformation (CCT) diagram of weld having 1.4 kJ/mm heat input

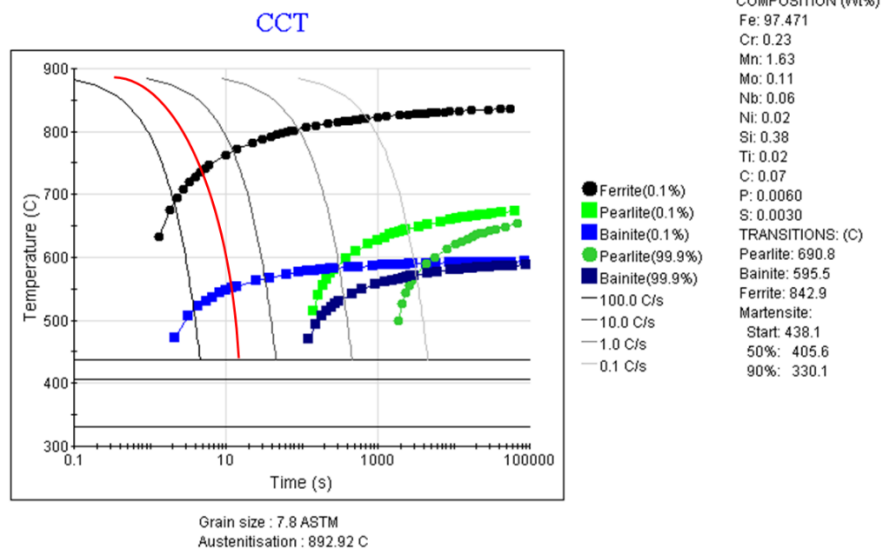


Figure 4.12. Continuous cooling transformation (CCT) diagram of weld having 1.1 kJ/mm heat input

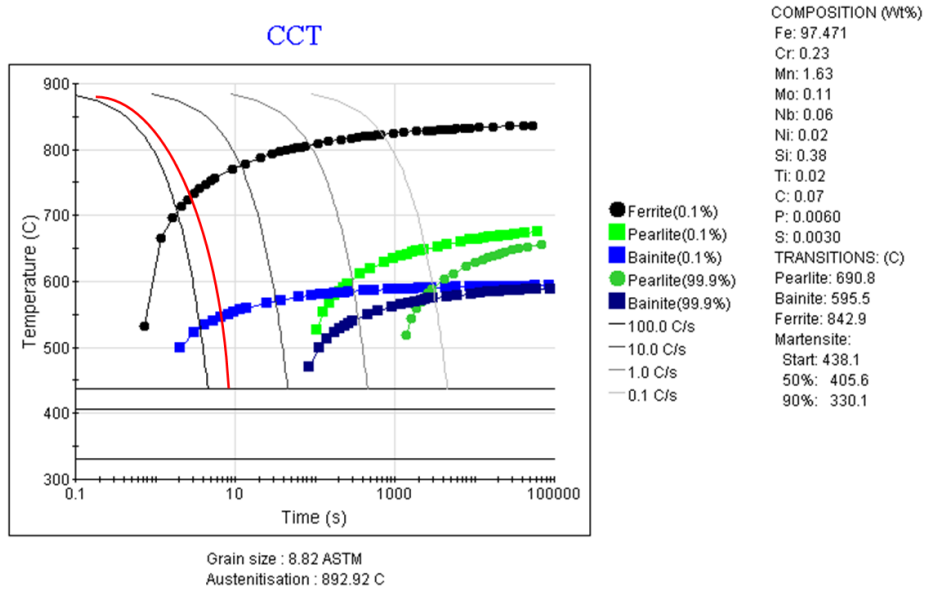


Figure 4.13. Continuous cooling transformation (CCT) diagram of weld having 0.65 kJ/mm heat input

A SEM image taken from CGHAZ region is given in Figure 4.14. As it is clearly seen, the microstructure and morphology is greatly different from base metal. The

microstructure is acicular ferrite along with a small amount of bainite, martensite-like, and carbides. During the formation of bainite the transformation is time dependent and diffusion controlled. On the other hand, martensite forms as a result of instantaneous shear of the austenite to a BCT lattice. The microstructure changes as the heat input and cooling time changes. In their work on X90 steel, Zhao et al.[66] states that, specimen having lower heat input and higher cooling rate has a microstructure consists of lower bainite and small amount of globular bainite and specimen having higher heat input and lower cooling rate has polygonal ferrite and some globular bainite in its structure. Li et al. [70] observed that microalloying elements such as Ti, Nb, and B restricts grain growth in CGHAZ while preventing the pearlite formation and large grain carbides at the grain boundaries. In the same heat input and cooling regime, addition of these microalloying elements results in bainite, polygonal ferrite and carbide having microstructure.

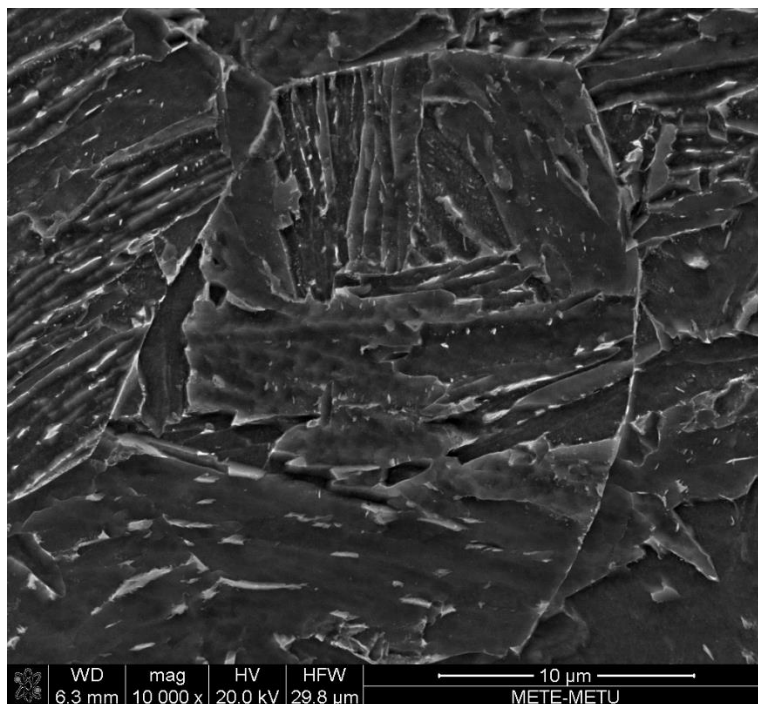


Figure 4.14. An SEM micrograph of CGHAZ

When considering multi-pass welding, additional CGHAZ-related regions can be defined:

- The unaltered coarse grained heat affected zone (U CGHAZ): the region in which the CGHAZ is reheated to a temperature above 1100 °C.
- The supercritically reheated coarse grained heat affected zone (SC CGHAZ): the region where the temperature reaches between  $A_{c3}$  and 1100 °C during reheating.
- The intercritically reheated coarse grained heat affected zone (IR CGHAZ) in which the temperature reaches between  $A_{c1}$  and  $A_{c3}$  during reheating.
- The subcritically reheated coarse grained heat affected zone (S CGHAZ) in which the temperatures reaches below  $A_{c1}$  during reheating.

These extra zones given in Figure 4.15 were illustrated by Machida et al. [71] in . Local brittle zones (LBZ) are referred as weak links in welds. These LBZ with lower toughness are most probably placed in IR CGHAZ next to fusion line [71]. The heat treatment after the first pass caused M-A constituent formation in IR CGHAZ which have detrimental effects on toughness of the material [19]. LBZs having these retained austenite and high C containing structures have a brittle nature and crack susceptible due to martensite [21]. Other researchers also stated that M-A containing LBZs are formed at HAZ, especially in IR CGHAZ [72].

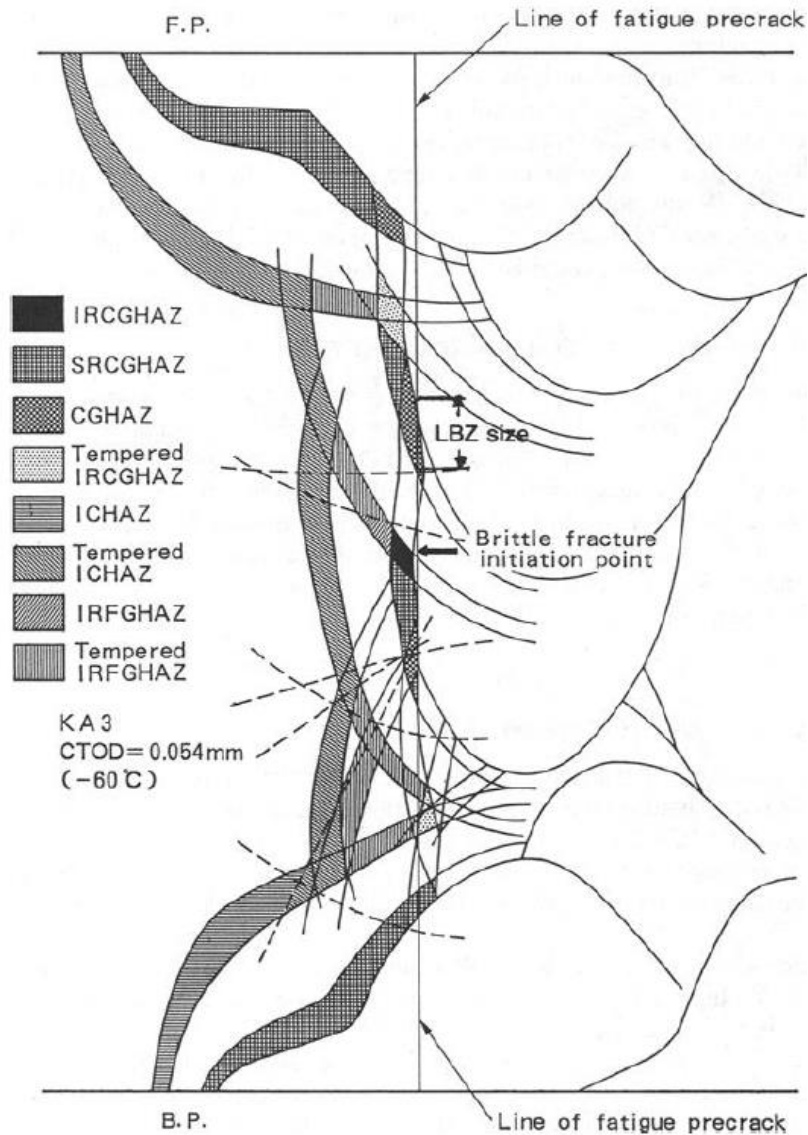


Figure 4.15. Additional CGHAZ regions formed in multi-pass welding [71]

The LBZs can be identified with the help of micro hardness measurements on welds since the indentations in macro hardness testing is too large to detect these zones. A high resolution micro hardness scanning with HV 0.5 conducted by Tosun [73] in a real line pipe multi-pass welding shows that hardened brittle regions are located at reheated IR CGHAZ regions (Figure 4.16).

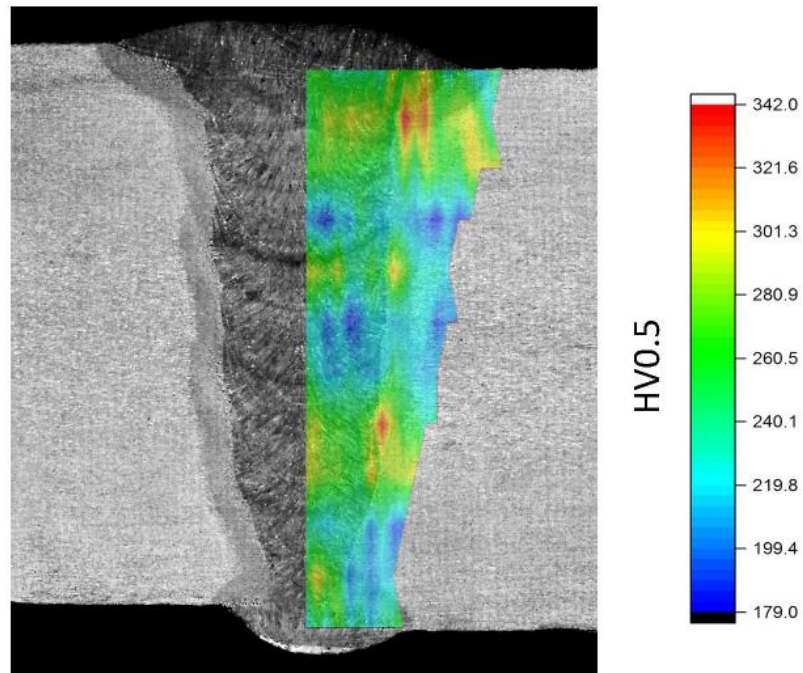


Figure 4.16. Hardness variations in multi-pass welding [73]

In this study, plates welded by the bead-on-plate method were subjected to hardness measurements to investigate the IRCGHAZ region. Since it is not possible to detect LBZs with large indentations and high interspacing of macro hardness, microhardness measurements were done with 0.5kgf (HV0.5). The 0.4mm interspacing and 0.5kgf yields higher resolution and helps to identify locally hard regions. Total of 570 measurements were recorded per specimens within an area of 7.2mm×11.6mm. The micro hardness values are given in the form of contour map in Figure 4.17, Figure 4.18 and Figure 4.19. Weld having one-pass 1.4 kJ/mm heat input shows homogeneous structure and hardness along HAZ region with a maximum of around 238 HV. However, plates having lower heat inputs which are welded by 2 successive weld passes shows hardening in reheated zones and hardness reaches 261 HV.

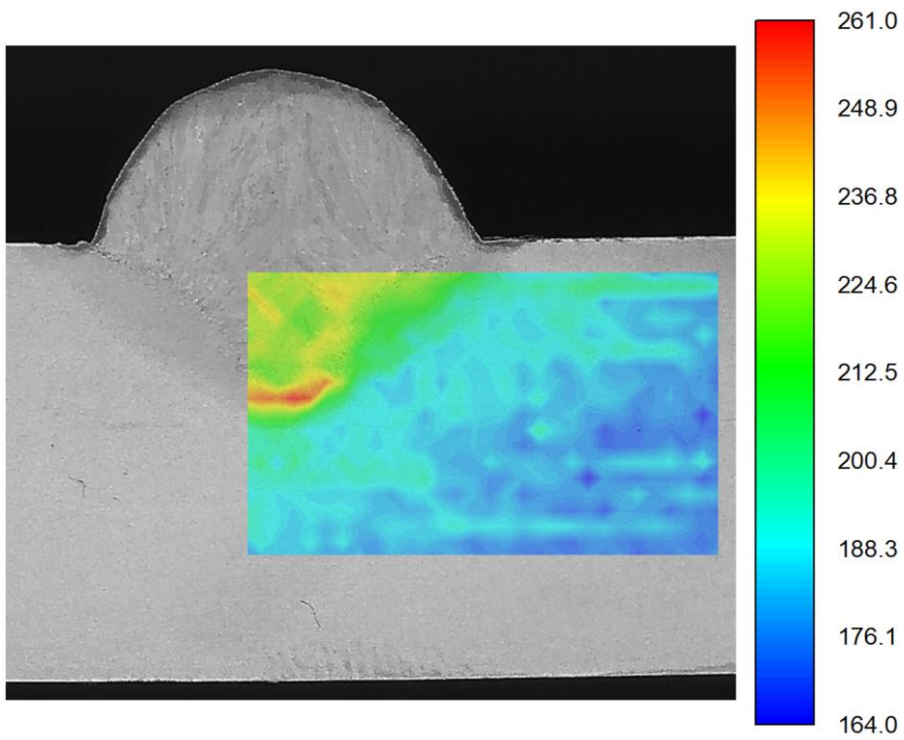


Figure 4.17. HV0.5 hardness contour map of weld having 0.65kJ/mm heat input

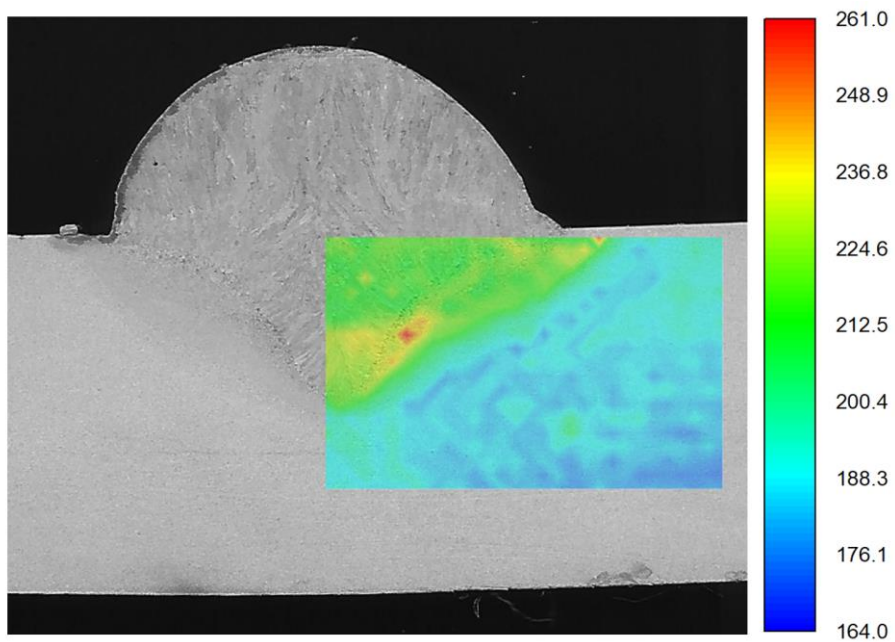


Figure 4.18. HV0.5 hardness contour map of weld having 1.1 kJ/mm heat input

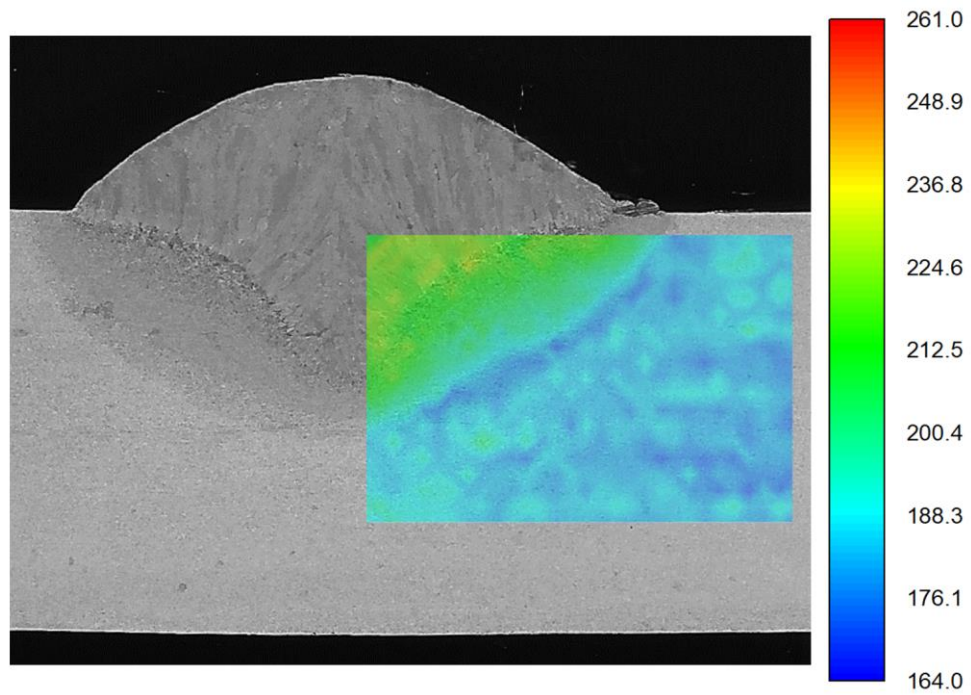


Figure 4.19. HV0.5 hardness contour map of weld having 1.4 kJ/mm heat input

Vickers macro hardness tests were conducted on multi-pass welded joints according to ASTM E384 [74] with the specimens that were prepared for macro examinations. The schematic representation of the hardness locations is given in Section 3.5.

Macro hardness values (HV10) are tabulated in Table 4.7.

Table 4.7. Macro hardness measurement results (HV10)

Specimen	Row	Base Metal			HAZ			Weld Metal			HAZ			Base Metal		
		1	2	3	4	5	6	7	8	9	10	11	12	13	14	15
1.1 kJ/mm	1	182	188	187	215	209	213	205	171	194	212	209	192	180	180	182
	2	182	179	186	198	211	216	209	176	195	250	225	215	176	177	183
	3	173	179	189	215	220	237	187	168	170	196	191	181	181	178	176
0.65 kJ/mm	1	181	186	186	206	222	221	224	215	230	221	219	210	188	192	193
	2	178	178	181	217	239	226	213	204	206	244	219	198	176	172	177
	3	186	186	183	217	227	238	213	191	185	204	202	189	189	191	192

Table 4.8. Comparison of micro and macro hardness values in the CGHAZ region

Heat Input	Hardness in CGHAZ		Hardness in IRCGAZ	
	Macro (HV10)	Micro (HV0.5)	Macro (HV10)	Micro (HV0.5)
1.1 kJ/mm	213	220	250	261
0.65 kJ/mm	222	254	244	225

The maximum hardness recorded at the untempered HAZ of the first weld pass with the heat input of 0.65 kJ mm<sup>-1</sup> because it corresponds to the shortest cooling period. However, the mean hardness of the reheated (tempered) part of HAZ of this bead is between 225 and 230 HV1. The higher secondary cooling temperatures that is close to the A<sub>C3</sub> during multi-pass welding, the hardenability and hence overall hardness decreases [75].

On the one hand, higher heat input ( $1.1 \text{ kJ mm}^{-1}$ ) provided longer cooling durations that limits martensite formation and consequently the mean hardness in CGHAZ (220-230 HV1). On the other hand, the successive thermal treatment of CGHAZ yielded LBZs with high hardness. LBZ usually contain untampered martensite embedded in carbon-enriched retained austenite (M-A) constituents [76]. Improper cooling rates may preclude the bainite transformation and promote formation of the M-A constituent [77]. The contribution of M-A constituent to the embrittlement of as-welded material depends principally on its shape, size, distribution and carbon concentration.

### **4.3. The Local Brittle Zones**

In micro hardness scanning of weld zones, regions giving peak hardness values are named as local brittle zones (LBZ). The term is first described in mid 1980s after different grades of microalloyed steels were subjected to CTOD testing from which unexpectedly low values have been observed in HAZ region. These zones are small, hard and brittle phase regions which form in heat affected zones (HAZ) of multi-pass welds [76]. These LBZs become more problematic as the low temperature toughness is decreased significantly because of the presence of undesired microstructural features such as large PAGS, upper bainite, microalloying elements' precipitates, and martensitic islands [78]. The M-A islands, or constituents, formed in CGHAZ of the weld have the most deteriorative effect on toughness of the material among these features [79]. During the second thermal cycle of CGHAZ formed during the previous weld run, some partial transformation to austenite takes place at the intercritically reheated spot of the zone (IR CGHAZ). This partial transformation to austenite occurs preferentially at the previous austenite grain (PAG) boundaries. This reverted austenite has relatively high C content as compared to the remaining matrix. Rapid cooling after the welding operation, together with the high C content, may yield

retained austenite, as well as the partial transformation to martensite. The spots that contain a mixture of martensite and retained austenite are called martensitic-austenitic (M-A) constituents.

The IR CGHAZ micrographs of 1.4 kJ/mm, 1.1 kJ/mm and 0.65 kJ/mm weldments are shown in Figure 4.23, Figure 4.24 and Figure 4.25, respectively. To investigate the M-A constituents whose volume fraction and size are the key factors for the toughness decrease [80] LePera etchant [45] was used. Thus M-A constituents are seen as white, PFs as light brown and GBs as light brown with white tiny M-A islands with the grains.

The matrix of the structure consists of in the weld with the highest heat input, the M-A constituents grown along the austenite grains are very small, but they are nearly connected, i.e. necklace type M-A constituent [81], when compared with the others (Figure 4.20). Weld having 1.1 kJ/mm heat input has small blocky and lath type M-A at the grain boundaries (Figure 4.21). On the other hand, 0.65 kJ/mm weld has bigger and generally blocky M-A along the prior austenite grain boundaries (Figure 4.22).

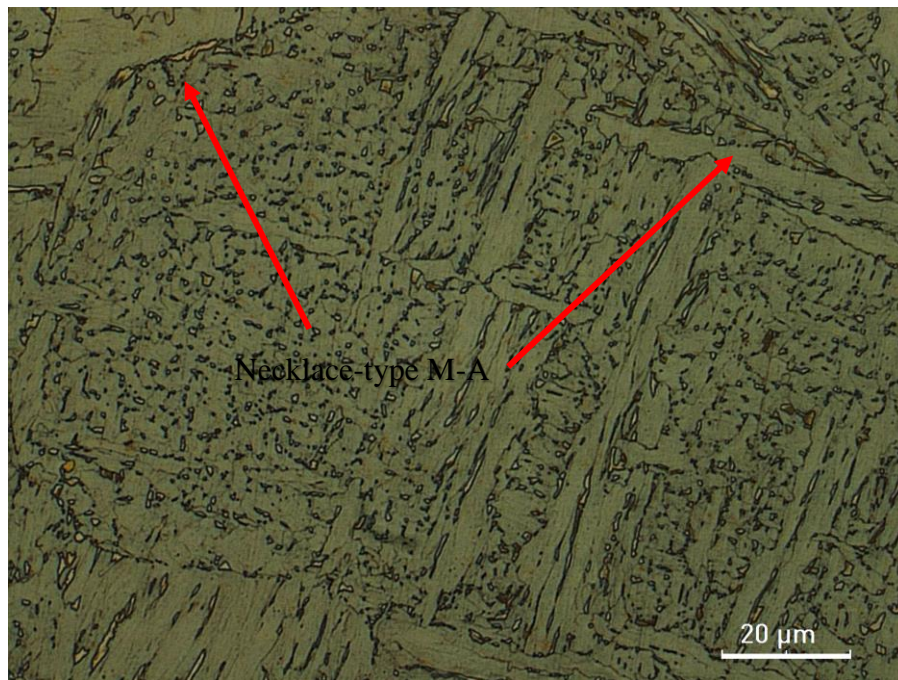


Figure 4.20. Micrograph of the CGHAZ region of 1.4 kJ/mm weldment (etched by LePera, 1000x)

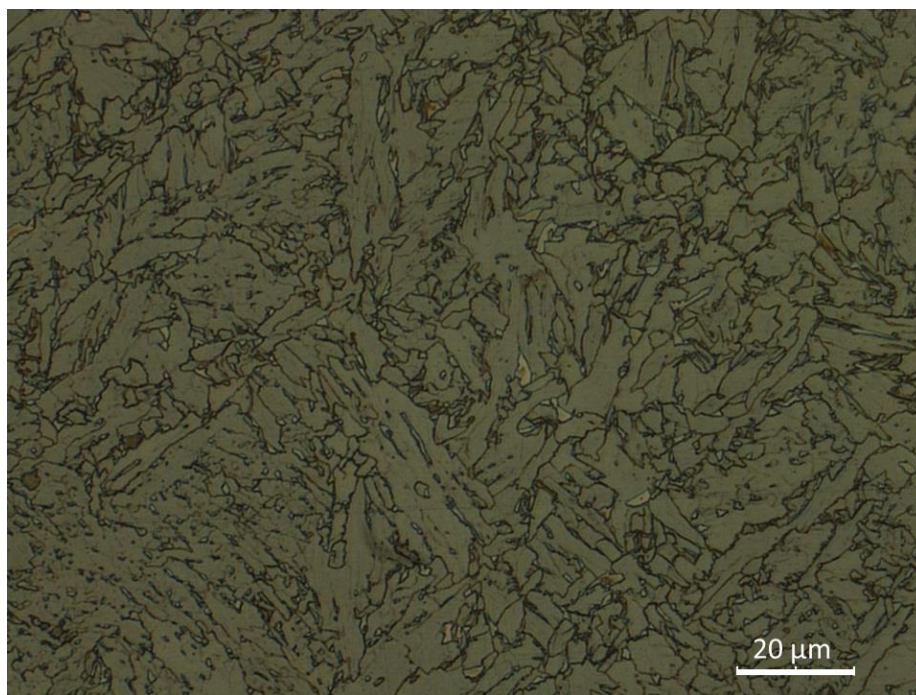


Figure 4.21. Micrograph of the IRCGAZ region of 1.1 kJ/mm weldment (etched by LePera, 1000x)

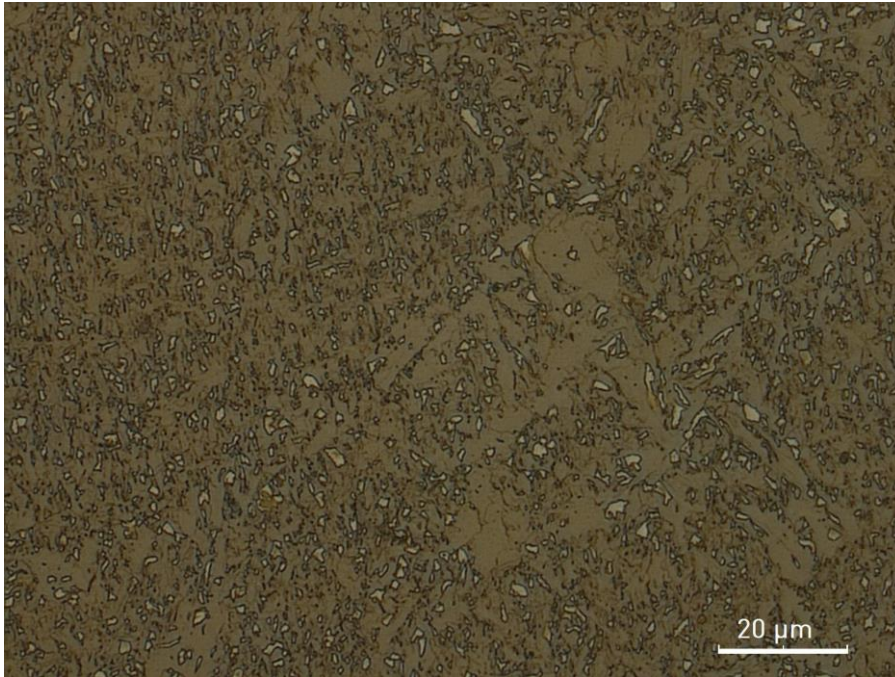


Figure 4.22. Micrograph of the IRCGHAZ region of 0.65 kJ/mm weldment (etched by LePera)

M-A constituents are hard and brittle due to martensite and the high C content of the retained austenite. Generally, as the indentation area was bigger than the sizes of M-A constituents, the micro hardness measurements were less trustworthy to inspect these hard M-A particles. Lower Vickers hardness values were measured than actual M-A constituent's hardness. Since the depth of the indentation was also an issue in this process the uncertainty is in two dimensions. The Berkovich nano-indentations give more reliable values for the hardness of the M-A constituents as the indentations are far smaller than the micro hardness indentations and the depth of indent is shallower.

Nano indentation measurements on the specimens for 1.15 kJ/mm and 0.65 kJ/mm yielded different results. The distribution of the hardness values are given in Figure 4.23.

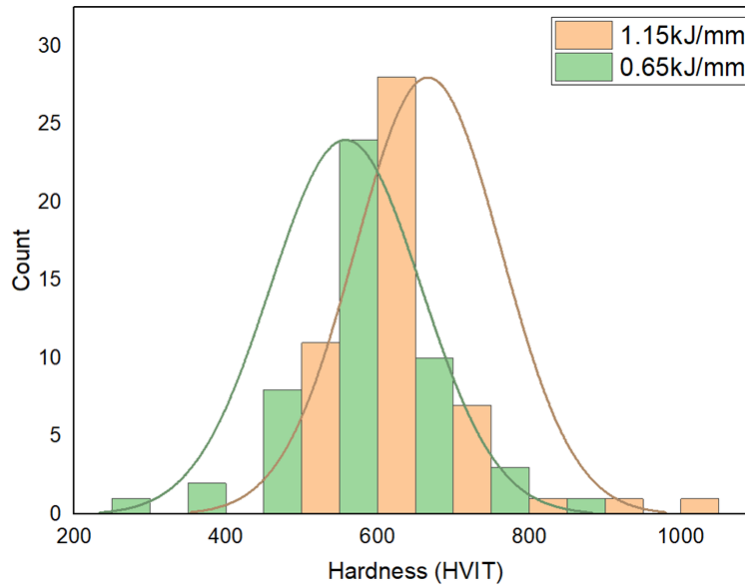


Figure 4.23. Nano indentation hardness distribution

Mohseni et al [82] suggest that the hardness of M-A constituents is related to its C content, which was determined to be in between 0.6 and 1.1 wt.% with a cooling rate of 20 °C/s. Li et al. [83] acquired similarly an average C content of 0.8 wt.% at cooling rates 15.3 and 6.8 °C/s for the successive thermal cycles.

#### 4.4. M-A Formation

When the peak temperature is between A1 and A3, the M-A constituent is considered to be transformed from the C-enriched austenite region, which was re-austenized in the second thermal cycle. M-A constituents are generally classified in terms of their morphology, namely massive (blocky) and elongated (stringer or slender). These constituents may be isolated or connected (necklace-type). TEM studies by Li et al. [86] indicated that both blocky-type and slender-type M-A constituent preferred to

form lath structure (Figure 4.24). Dark field TEM images [19] indicate that the adjacent laths may have large crystallographic misorientations.

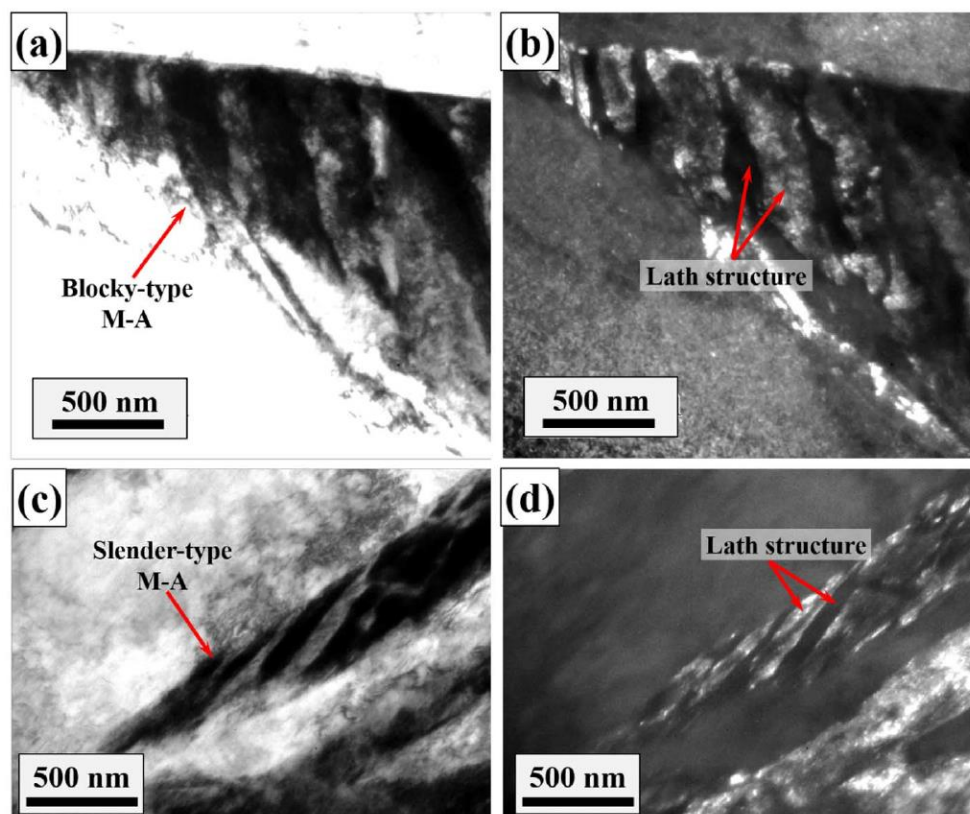


Figure 4.24. TEM micrographs of the M-A constituent in the IR CGHAZ. (a, c) bright field and (b, d) dark field micrographs [19]

The higher PAGES promotes formation of acicular ferrite due to high density of intragranular nucleation sites, such as inclusions. Whereas, the smaller PAGES, containing a relatively high density of grain boundary nucleation sites, leads to a microstructure that consists predominantly of bainite. The bainite nucleates at PAG boundaries and grows as laths that have similar crystallographic orientation and a high uniform dislocation density[87]. The length of laths is limited by impingement with other laths, and C-enriched interlath austenite transforms to M-A constituents. On the

contrary, acicular ferrite grows as randomly oriented laths where M-A constituents are usually formed as discrete particles. A crack has to be extended through a more tortuous path in a microstructure where acicular ferrites exist, thereby leading to an improvement in toughness [88]. Austenite grain size affects the transformation of martensite and so does the formation of M-A constituents. Yang and Bhadeshia [89] show the relationship between austenite grain size and the amount of transformation as below:

$$M_s - T = \frac{1}{b} \left[ \ln \frac{1}{aV_\gamma} \left\{ \exp \left( -\frac{\ln(1-f)}{m} \right) - 1 \right\} + 1 \right] \quad (21)$$

where a and b are fitting parameters for the steel, f is martensite fraction, m is aspect ratio of martensite plates and  $V_\gamma$  is average austenite volume.

Additionally, Andrews[90] estimates the  $M_s$  temperature of the steel with respect to the alloying elements' weight percent as:

$$M_s = 539 - 453C + 15Cr - 16.9Ni - 9.5Mo + 217C^2 - 715CMn - 67.6CCr \quad (22)$$

As PAGS becomes larger, the transformation from austenite to martensite increases. As transformation increases probability of retained austenite decreases. This theory supports the case that lower amount of retained austenite and thus M-A constituent in the 1.15kJ/mm weldment, which have larger PAGS than the 0.65 kJ/mm weldment. On the other hand, due to higher C migration, an increment in local C concentration occurs. This promotes the decrease of  $M_s$  temperature and retained austenite in the structure.

The formation of M-A constituents in the IR CGHAZ depends on the CGHAZ microstructure and the cooling rate. The cooling rate of the second thermal cycle determines the bainitic transformation from austenite; either lower or upper bainite. As the cooling rate increases, the transformed product becomes more lower bainite. The lower bainite consists of sheaves of elongated ferrite crystals with low misorientations and a high dislocation density, containing quasi-equiaxed M-A constituents. Whereas, upper bainite consists of parallel ferrite plates separated by low angle boundaries, and containing both very high dislocation densities and M-A constituents retained between the plates [25]. Nonetheless, Ikawa et al. [91] and Matsuda et al. [77] experienced M-A constituents increased rapidly when  $\Delta t_{8/5}$  became longer than 10-20 secs achieving maximum values and then decreasing due to decomposition into carbides in ferrite that began after 50 secs.

Not only the fraction, distribution and morphology of M-A particles are important in terms of the fracture toughness, but also C content of the constituent. C migrate to  $\gamma$  through  $\gamma/\alpha$  interface due to the lower C solubility in  $\alpha$ . The M-A constituents in HSLA steels content from 0.6 up to 2.2% whatever the C content in the matrix is. As an increase in carbon content results in an increase of the hardness of the martensite, hardness measurements from M-A constituents having different morphology differs; 800 to 1200 HV for massive and 600 to 800 HV for elongated [92] [93].

Erian [94] found that the strain and the residual stress in as-welded steel grade X70 with the aid of magnetic Barkhausen noise (MBN) and deflection angle versus number of passes graphs. The number of weld passes, so the heat input of each pass, showed correlation between each other (Figure 4.25). As the total number of weld passes increases the magnitude of strain and the residual stress gets lower. The strain in the multi-phase field increases the total area of the interface of phases, consequently the rate of C diffusion during the phase transformation increases [95]. Besides, the plastic

strain of austenite influences the kinetics of ferrite formation; A3 increases [96]. Both processes promote the C-enrichment in the remaining austenite during cooling after welding operation.

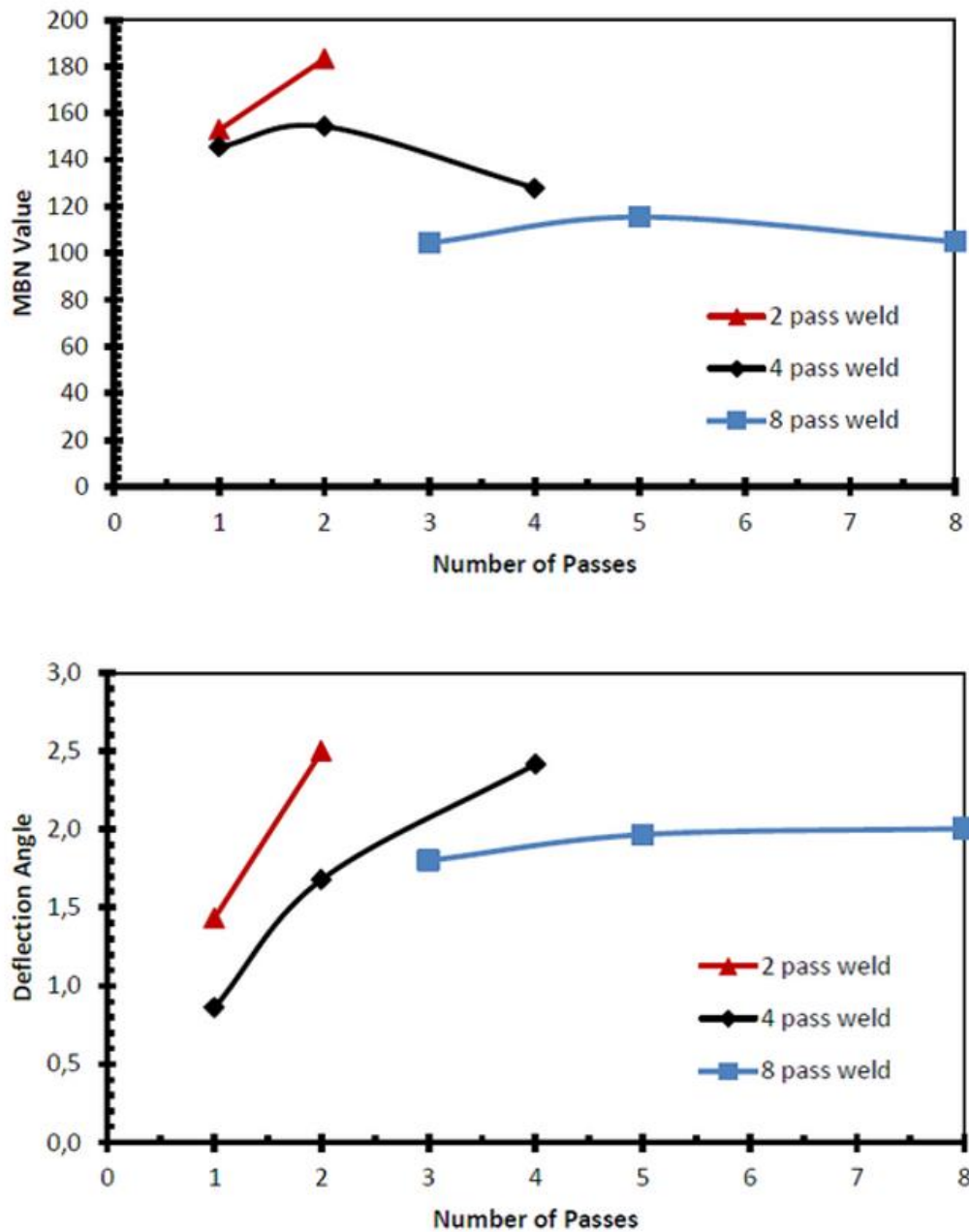


Figure 4.25. Relationship between number of weld passes and residual strain [94]

#### 4.5. Fracture Toughness of CGHAZ

The resistance against the crack initiation under static loads were determined with single value parameter.

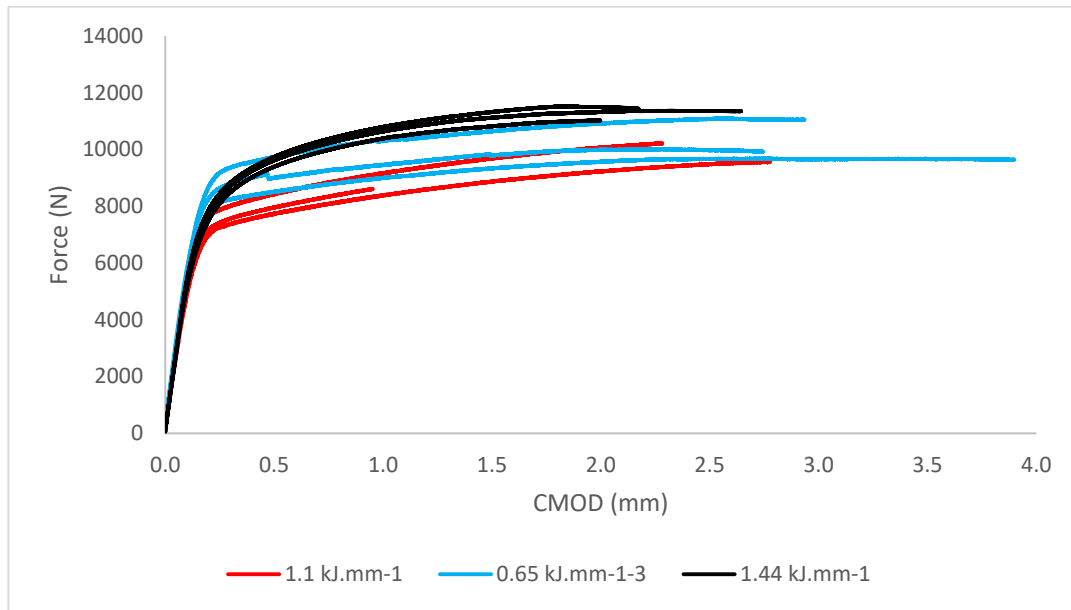


Figure 4.26. Force vs. CMOD graph of the specimens

Single  $\delta$  parameters are presented in Table 4.7. All of the specimens were notched from fusion line (FL).

Table 4.7. Minimum Single  $\delta$  (CTOD) values

Specimen	HPAW <sub>1.45kJ/mm</sub>	GMAW <sub>1.15kJ/mm</sub>	GMAW <sub>0.65kJ/mm</sub>
a0 (mm)	10.09	10.12	10.76
$\Delta a$ (mm)	0.46	1.11	0.98
$\delta$ (mm)	0.209	0.229	0.627
$\delta_{\text{average}}$ (mm)	0.471	0.516	0.696

There are differences between the CTOD values of the two higher heat input weldments. This may be a result of homogeneous distribution and matching microstructure. However, these tests were terminated with the occurrence of sudden force drop, pop-in failure. This phenomenon may be caused by different reasons such as, initiation of a brittle crack in local brittle zones, M-A constituents in the material, formation of delaminations on the plane which is perpendicular to the fatigue pre-crack plane. The fracture surfaces of the materials may help to identify the cause of the failure (Figure 4.27).

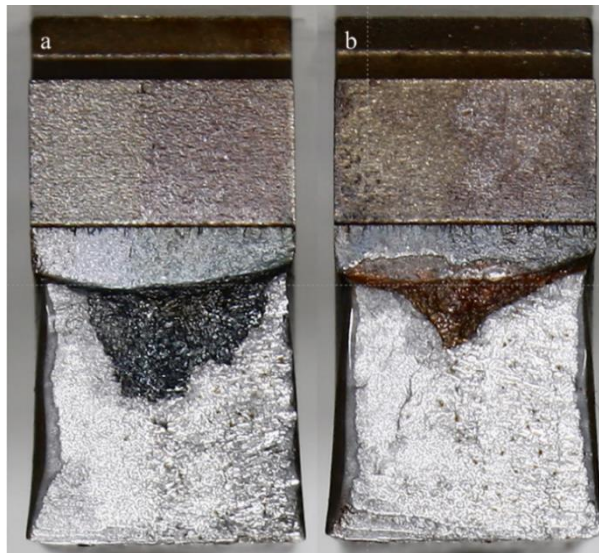


Figure 4.27. Representative fracture surfaces of CTOD tests of  
(a) 1.15 kJ/mm weldment (b) 0.65 kJ/mm weldment

The microstructure of the material changes in the course of welding with respect to the heat input. New phases and precipitates are formed, such as M-A constituents, and coarsening of grains occur. These will be discussed in Section 4.6.

#### 4.6. Effect of M-A Constituents on the Crack Extension Resistance

The toughness of the IR CGHAZ strongly depends on the distribution, fraction, morphology and connectivity of grain boundaries of M-A constituents and the surrounding microstructure [25]. Comparing with the CGHAZ, the toughness of the IR CGHAZ is readily lower [22]. Lambert-Perlade et al. [97] suggested both M-A constituents and coarse upper bainite deteriorate the toughness. The mechanism by which M-A constituents decrease toughness in IR CGHAZ appear to be due to cleavage cracking resulting from debonding of M-A constituents or between two closely separated M-A constituents[98]. Whereas, a limited volume fraction of M-A constituents, which are uniformly distributed and relatively small, together with acicular ferrites around are known to provide reasonable strength-toughness performances, even may be effective as a strengthening mechanism.

Lan et al. [99] suggested that higher heat input leads to larger M-A constituents and consequently more deterioration in toughness due to debonding mechanism. Hu et al. [68] support this suggestion. At the stretch zone (i.e. lower stresses) decohesion of stringer M-A constituents were observed. Whereas at high stresses, cracking of blocky M-A constituents was observed on fracture surfaces. This variation in the cracking mechanisms were also observed by Li and Baker [24].

Fracture surfaces of the specimens of single-pass weldments with the heat input of  $1.40 \text{ kJ mm}^{-1}$  and multi-pass weldments with the heat input of  $1.15 \text{ kJ mm}^{-1}$  revealed a number of initiation sites, which were close to the stretch zone (in front of the fatigue pre-crack), from the grains with M-A constituents that were near connected grain boundary network within the high-angle boundaries (Figure 4.28). Plateau-metallography efforts provided additional evidence for the interfacial decohesion that

lead formation of micro-cracks at the necklace-type M-A constituents and the surrounding matrix (Figure 4.29).

M-A constituents may be regarded as microstructural discontinuities in the CGHAZ and IR CGHAZ. The critical size of a linear discontinuity can be evaluated using the equation (23) proposed by Griffith.

$$\sigma_c = \left\{ \frac{\pi E \gamma_p}{(1-\nu^2)d} \right\}^{1/2} \quad (23)$$

where  $\gamma_p$  is the effective surface energy of the discontinuity,  $\nu$  stands for the Poisson's ratio,  $E$  is the elastic modulus and  $d$  is the length of the discontinuity, which can be regarded as the maximum width of a necklace-type cluster of M-A constituents.  $E$  and  $\nu$  can be taken 210 GPa and 0.3 according to the tensile tests of the fusion zone and the parent metal.  $\gamma_p$  may be assumed as 8 – 14 J m<sup>-2</sup> according to Lan et al [10]. Consequently, the calculated  $\sigma_c$  would be between 1.4 and 2.4  $\mu\text{m}$ . The mean M-A size at low heat input multi-pass weldment is less than the calculated  $\sigma_c$  but, the mean M-A sizes at high heat input single- and multi-pass weldments are well above it. M-A particles in the multi-pass 0.65 kJ mm<sup>-1</sup> heat input weldments are still detrimental to fracture toughness but not to the severe extent as in the other weldments. Debonded M-A particles were still observed on the cleavage facets (Figure 4.30), however initiation spots were complicated and without a clear initiation site.

Post-test metallographic and fractographic observations suggest that the mechanism by which the M-A distribution/morphology of deteriorates toughness appears to arise from debonding due to strength and hardness mismatch that reduces cracking resistivity of the system.

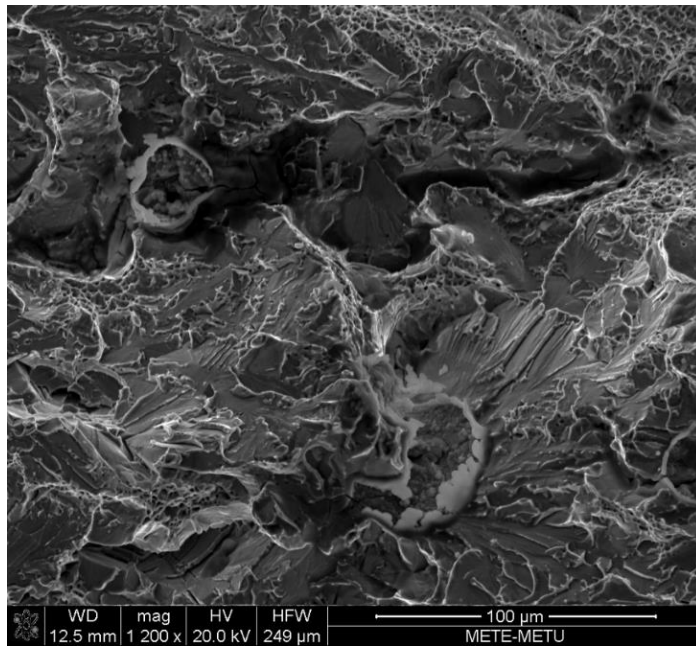


Figure 4.28. Fracture surface of the *CTOD* specimen (1.15 kJ/mm weldment)

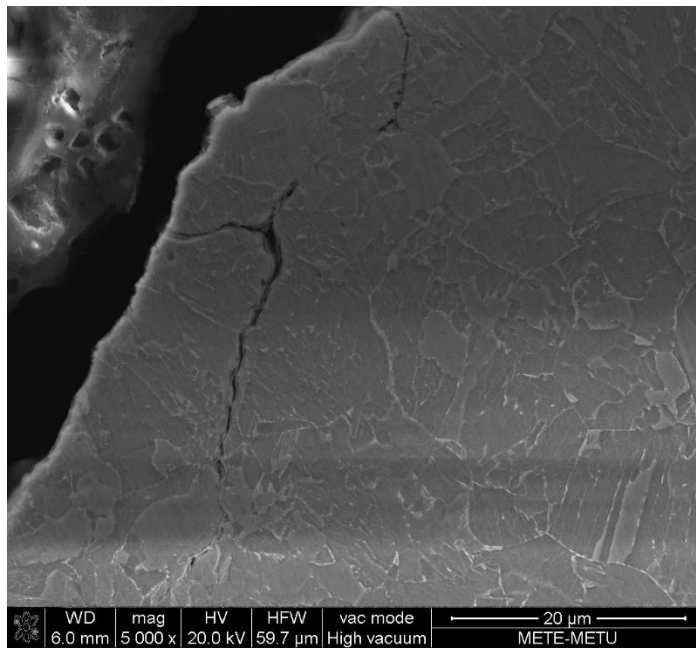


Figure 4.29. Plateau metallography micrograph of the *CTOD* specimen (1.15 kJ/mm weldment)

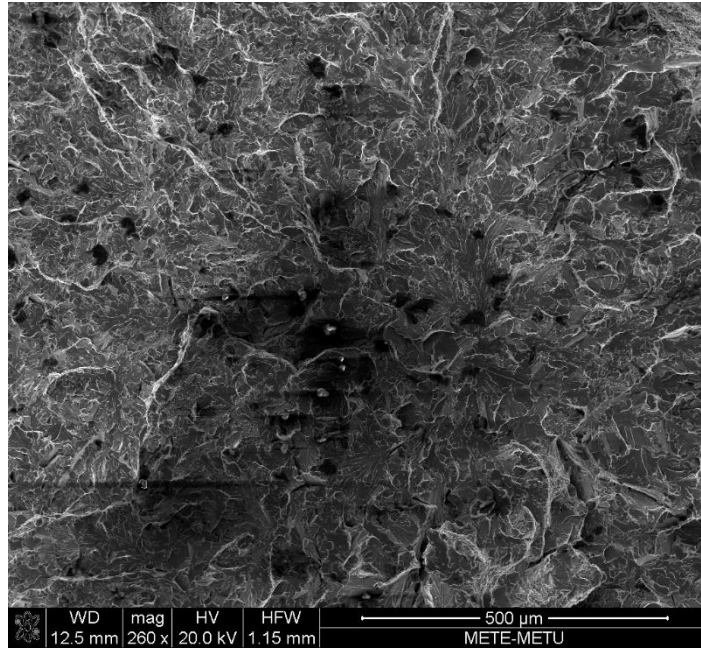


Figure 4.30. Fracture surface of the CTOD specimen (0.65 kJ/mm weldment)



## CHAPTER 5

### CONCLUSIONS

Thermal cycles of a welding operation alter the microstructure at the proximity of joint, namely at HAZ. LBZs formed in HAZ of the weldment deteriorate the toughness. The lowest toughness is expected in CGHAZ for a single-pass welding operation, whereas the most degraded spots generally exist in IR CGHAZ. It is widely acknowledged that M-A constituents in LBZs are responsible from this deterioration in the toughness.

In this study, the effects of heat input and number of thermal cycles induced during gas metal arc welding (GMAW) on fracture toughness of pipeline steel grade API 5L X70M were investigated. Mechanical tests and microstructural examinations were performed to gain a better understanding of the correlation between the heat input and formation of local brittle zones.

For heat inputs of 0.65, 1.15 and 1.40 kJ mm<sup>-1</sup>, different peak temperatures and cooling rates were obtained at CGHAZ. Different thermal routes lead to different CGHAZ and IR CGHAZ microstructures in terms of morphology and distribution of the M-A constituents, as well as principal primary phases. Formation of microstructural features was addressed to prior austenite grains (PAGS) and the time interval for diffusion-assisted transformations.

Distribution, type and C-content of M-A constituents along PAGs control the fracture behavior of IR CGHAZ, and negatively affect the local crack extension resistance.

The amount of heat introduced by a welding operation has a contradictory effect on the formation of M-A constituents. The following conclusions can be drawn from this particular study:

- There exists formation of local brittle zones (LBZ) occurs during multi-pass welding which are the weakest points of HAZ.
- The amount of heat introduced by a welding operation has a contradictory effect on the formation of M-A constituents.
- The high heat input induces less retained austenite at the CGHAZ in single-pass welding operations. However, it gives the worst results in terms of CTOD values.
- In multi-pass welding operations, the high heat input leads to less retained austenite and M-A constituent due to the relatively large PAGs.
- M-A constituents control the fracture behavior of IR CGHAZ and affect negatively the crack extension resistance of the material locally.
- The CTOD test results show that, the type and distribution of the M-A is more effective than the amount of M-A.
- The more M-A containing low heat input weldment gives the best results when compared with the higher heat inputs.
- The lower in amount but in the form of necklace and lath type M-A constituents in 1.4 and 1.15 kJ/mm heat input weldments affects the CTOD values more drastically.

For the future, EBSD analyses and Berkovich nano-indentation surveys should be conducted in detail within IR CGHAZ region to understand the effect of M-A constituent better.

## REFERENCES

- [1] “API Standard 1104 Welding of Pipelines and Related Facilities,” *21st Ed.*, 2013.
- [2] “API 5L Specification for Line Pipe.” API Publishing Services: 1220 L Street, NW, Washington, DC 20005.
- [3] F. B. Pickering, “High Strength Low Alloy Steels,” *Mater. Sci. Technol.*, vol. 45, no. 4, pp. 295–301, 2006.
- [4] S. Vervynckt, K. Verbeken, B. Lopez, and J. J. Jonas, “Modern HSLA steels and role of non-recrystallisation temperature,” *Int. Mater. Rev.*, vol. 57, no. 4, pp. 187–207, 2012.
- [5] D. T. Llewellyn, R. C. Hudd, D. T. Llewellyn, and R. C. Hudd, “2 – Low-carbon structural steels,” *Steels*, pp. 137–198, 1998.
- [6] Y. Kikuta, T. Araki, A. Hirose, and E. Kyo, “The Effect of Center Segregation of TMCP Steels with Continuous Casting Process on Weld Cold Cracking,” *Q. J. Japan Weld. Soc.*, vol. 2, no. 3, pp. 383–389, 1984.
- [7] L. J. Cuddy, “Microstructures developed during thermomechanical treatment of HSLA steels,” *Metall. Trans. A*, vol. 12, no. 7, pp. 1313–1320, 1981.
- [8] G. Krauss and S. W. Thompson, “Ferritic Microstructures in Continuously Cooled Low- and Ultralow-carbon Steels,” *ISI J Int.*, vol. 35, no. 8, pp. 937–945, 1995.
- [9] T. Araki, I. Kozasu, H. Tankechi, K. Shibata, and M. Enomoto, “Atlas for Bainitic microstructures,” *ISIJ, Tokyo, Japan*, vol. 1, 1992.
- [10] L. Y. Lan, C. L. Qiu, D. W. Zhao, and X. H. Gao, “Microstructural Evolution and Mechanical Properties of Nb-Ti Microalloyed Pipeline Steel,” *J. Iron Steel Res. Int.*, vol. 18, no. 2, pp. 57–63, 2011.
- [11] H. Zhao and E. J. Palmiere, “Effect of austenite grain size on acicular ferrite transformation in a HSLA steel,” *Mater. Charact.*, vol. 145, no. June, pp. 479–489, 2018.
- [12] L. Resource, *Basic Manual Metal Arc Welding (MMAW) Learning Resource Metals and Engineering ENG722*. 2016.
- [13] Weld J., “Fact Sheet - Choosing Shielding for GMA Welding.” p. 79: 18, 2000.
- [14] R. Singh, “Welding and Joining Processes,” *American Society of Mechanical Engineers, Production Engineering Division (Publication) PED*, vol. 51.

- Butterworth-Heinemann, pp. 163–195, 01-Jan-1991.
- [15] S. Kou, *Welding Metallurgy*, Second., vol. 822, no. 1–3. John Wiley & Sons, Inc., 2003.
  - [16] BSI, “EN 1011-2 Welding - Recommendations for welding of metallic materials - Part 2: Arc welding of ferritic steels,” 2004.
  - [17] J. E. Ramirez, S. Mishael, and R. Shockley, “Properties and sulfide stress cracking resistance of coarse-grained heat-affected zones in V-microalloyed X60 steel pipe,” *Weld. J.*, vol. 84, no. 7, pp. 113s-123s, 2005.
  - [18] J. Moon, S. J. Kim, and C. Lee, “Effect of thermo-mechanical cycling on the microstructure and strength of lath martensite in the weld CGHAZ of HSLA steel,” *Mater. Sci. Eng. A*, vol. 528, no. 25–26, pp. 7658–7662, 2011.
  - [19] Y. You, C. Shang, L. Chen, and S. Subramanian, “Investigation on the crystallography of the transformation products of reverted austenite in intercritically reheated coarse grained heat affected zone,” *Mater. Des.*, vol. 43, pp. 485–491, 2013.
  - [20] X. Li, Y. Fan, X. Ma, S. V. Subramanian, and C. Shang, “Influence of Martensite-Austenite constituents formed at different intercritical temperatures on toughness,” *Mater. Des.*, vol. 67, pp. 457–463, 2015.
  - [21] M. Eroglu and M. Aksoy, “Effect of initial grain size on microstructure and toughness of intercritical heat-affected zone of a low carbon steel,” *Mater. Sci. Eng. A*, 2000.
  - [22] Z. Zhu, L. Kuzmikova, H. Li, and F. Barbaro, “The effect of chemical composition on microstructure and properties of intercritically reheated coarse-grained heat-affected zone in X70 steels,” *Metall. Mater. Trans. B Process Metall. Mater. Process. Sci.*, vol. 45, no. 1, pp. 229–235, 2014.
  - [23] V. G. Haugen, B. R. S. Rogne, O. M. Akselsen, C. Thaulow, and E. Østby, “Local mechanical properties of intercritically reheated coarse grained heat affected zone in low alloy steel,” *Mater. Des.*, vol. 59, pp. 135–140, 2014.
  - [24] Y. Li and T. N. Baker, “Effect of morphology of martensite–austenite phase on fracture of weld heat affected zone in vanadium and niobium microalloyed steels,” *Mater. Sci. Technol.*, vol. 26, no. 9, pp. 1029–1040, 2010.
  - [25] C. L. Davis and J. E. King, “Cleavage initiation in the intercritically reheated coarse-grained heat-affected zone: Part I. Fractographic evidence,” *Metall. Mater. Trans. A*, vol. 25, no. 3, pp. 563–573, 1994.
  - [26] D. Turnbull, “Kinetics of Heterogeneous Nucleation,” *J. Chem. Phys.*, vol. 18, no. 2, pp. 198–203, Feb. 1950.
  - [27] W. F. Savage, C. D. Lundin, and A. H. Aronson, “Weld Metal Solidification

- Mechanics,” *Weld J.*, vol. 44, no. April, pp. 175-s, 1965.
- [28] T. W. Nelson, J. C. Lippold, and M. J. Mills, “Nature and Evolution of the Fusion Boundary in Ferritic-Austenitic Dissimilar Weld Metals , Part 1 Nucleation and Growth A model for heterogeneous nucleation along the fusion boundary is proposed,” *Weld. Journal-New York-*, vol. 78, no. October, pp. 329-s, 1999.
- [29] I. Milne, R. O. Ritchie, and B. Karihaloo, *Comprehensive structural integrity*, no. 9. c. Elsevier, 2003.
- [30] S. W. Leon, “Basics of Fracture Mechanics as Applied to Structural Integrity of RPVs,” no. November, 2009.
- [31] X. K. Zhu and J. A. Joyce, “Review of fracture toughness (G, K, J, CTOD, CTOA) testing and standardization,” *Eng. Fract. Mech.*, vol. 85, pp. 1–46, 2012.
- [32] G. R. Irwin, *Analysis of stresses and strains near the end of a crack traversing a plate. J Appl Mech Trans ASME 24: 361-364*, vol. 24. 1957.
- [33] J. R. Rice, “A path independent integral and the approximate analysis of strain concentration by notches and cracks,” vol. 35, pp. 379–386, 1968.
- [34] A. A. Wells, *Application of fracture mechanics at and beyond general yield*, vol. 10. 1963.
- [35] “ASTM E1820-18ae1 Standard Test Method for Measurement of Fracture Toughness,” *ASTM Standards*. ASTM International, West Conshohocken, PA, p. E 1820 – 01, 2018.
- [36] M. Cagirici, “Investigation of Key-Hole Weldability of Line Pipe Steel Grade X70M in Terms of Fracture Toughness,” Middle East Technical University, 2017.
- [37] CRC-Evans, “P-625 Computerized Welding Machine.” [Online]. Available: [https://www.crc-evans.com/sites/crcevans.com/files/pdfs/P-625\\_Specification\\_Brochure\\_v18.pdf](https://www.crc-evans.com/sites/crcevans.com/files/pdfs/P-625_Specification_Brochure_v18.pdf). [Accessed: 19-Nov-2019].
- [38] “ASTM E 415, Standard Test Method for Analysis of Carbon and Low-Alloy Steel by Spark Atomic Emission Spectrometry,” *ASTM Int.*, pp. 1–11, 2017.
- [39] “ASTM E2007-10 Standard Guide for Computed Radiography.” 2016.
- [40] “ASTM E1742/E1742M-18 Standard Practice for Radiographic Examination.” 2018.
- [41] ASME Boiler and Pressure Vessel Committee on Welding Brazing and Fusion Qualification, “ASME Section IX-2015 Welding, Brazing, and Fusing Qualifications,” *Qualif. Stand. Welding, Brazing, Fusing Proced. Welders*;

*Brazers; Welding, Brazing, Fusing Oper.*, p. 434, 2015.

- [42] “ISO 5173:2009 Destructive tests on welds in metallic materials — Bend tests,” 2009.
- [43] “ISO 4136:2012 Destructive tests on welds in metallic materials — Transverse tensile test,” 2018.
- [44] “ISO 17639:2003 Destructive tests on welds in metallic materials — Macroscopic and microscopic examination of welds,” 2003.
- [45] F. S. LePera, “Improved etching technique for the determination of percent martensite in high-strength dual-phase steels,” *Metallography*, vol. 12, no. 3, pp. 263–268, 1979.
- [46] “ASTM E112-13 Standard Test Methods for Determining Average Grain Size,” 2013.
- [47] “ASTM E1508-12a Standard Guide for Quantitative Analysis by Energy-Dispersive Spectroscopy,” 2019.
- [48] C. A. Schuh, “Nanoindentation studies of materials,” *Mater. Today*, vol. 9, no. 5, pp. 32–40, May 2006.
- [49] “NanoScience Instruments,” 2019. [Online]. Available: <https://www.nanoscience.com/techniques/mechanical-testing/#how>. [Accessed: 15-Oct-2019].
- [50] “ISO 6892-1:2016 Metallic materials — Tensile testing — Part 1: Method of test at room temperature,” p. 79, 2016.
- [51] “ISO 15653:2018 Metallic materials — Method of test for the determination of quasistatic fracture toughness of welds,” 2018.
- [52] “ISO 12135:2016 Metallic materials — Unified method of test for the determination of quasistatic fracture toughness,” 2016.
- [53] H. L. Andrade, M. G. Akben, and J. J. Jonas, “Effect of molybdenum, niobium, and vanadium on static recovery and recrystallization and on solute strengthening in microalloyed steels,” *Metall. Trans. A*, vol. 14, no. 10, pp. 1967–1977, 1983.
- [54] M. Charleux, W. J. Poole, M. Militzer, and A. Deschamps, “Precipitation behavior and its effect on strengthening of an HSLA-Nb/Ti steel,” *Metall. Mater. Trans. A Phys. Metall. Mater. Sci.*, vol. 32, no. 7, pp. 1635–1647, 2001.
- [55] B. K. Show, R. Veerababu, R. Balamuralikrishnan, and G. Malakondaiah, “Effect of vanadium and titanium modification on the microstructure and mechanical properties of a microalloyed HSLA steel,” *Mater. Sci. Eng. A*, vol. 527, no. 6, pp. 1595–1604, Mar. 2010.

- [56] F. Minami *et al.*, “Fracture toughness evaluation of multipass weld haz considering the strength mismatch effect,” *Weld. Int.*, vol. 9, no. 7, pp. 546–553, 1995.
- [57] C. Zhou and R. Priestner, “The evolution of precipitates in Nb-Ti microalloyed steels during solidification and post-solidification cooling,” *ISIJ Int.*, vol. 36, no. 11, pp. 1397–1406, 1996.
- [58] S. G. Hong, H. J. Jun, K. B. Kang, and C. G. Park, “Evolution of precipitates in the Nb-Ti-V microalloyed HSLA steels during reheating,” *Scr. Mater.*, vol. 48, no. 8, pp. 1201–1206, 2003.
- [59] M. Shome, “Effect of heat-input on austenite grain size in the heat-affected zone of HSLA-100 steel,” *Mater. Sci. Eng. A*, vol. 445–446, pp. 454–460, Feb. 2007.
- [60] M. Lord, “Effect of interpass temperature on properties of high-strength weld metals,” *Svetsaren, a Weld. Rev.*, vol. 54, no. 1, pp. 53–58, 1999.
- [61] R. S. Funderburk, “A look at heat input,” *Weld. Innov. Q.*, vol. 16, no. 1, pp. 8–11, 1999.
- [62] C. Li, Y. Wang, and Y. Chen, “Influence of peak temperature during in-service welding of API X70 pipeline steels on microstructure and fracture energy of the reheated coarse grain heat-affected zones,” *J. Mater. Sci.*, vol. 46, no. 19, pp. 6424–6431, 2011.
- [63] M. Shome, O. P. Gupta, and O. N. Mohanty, “Effect of simulated thermal cycles on the microstructure of the heat-affected zone in HSLA-80 and HSLA-100 steel plates,” *Metall. Mater. Trans. A*, vol. 35, no. 3, pp. 985–996, 2004.
- [64] J. L. M. Andia, L. F. G. de Souza, and I. de S. Bott, “Microstructural and Mechanical Properties of the Intercritically Reheated Coarse Grained Heat Affected Zone (ICCGHAZ) of an API 5L X80 Pipeline Steel,” *Mater. Sci. Forum*, vol. 783–786, pp. 657–662, 2014.
- [65] W. J. Poole, M. Militzer, and T. Garcin, “An Integrated Model to Predict Microstructure and Mechanical Properties in the Heat Affected Zone for X80 Linepipe.” pp. 301–306, 24-Sep-2012.
- [66] W. Zhao, W. Wang, S. Chen, and J. Qu, “Effect of simulated welding thermal cycle on microstructure and mechanical properties of X90 pipeline steel,” *Mater. Sci. Eng. A*, vol. 528, no. 24, pp. 7417–7422, 2011.
- [67] D. V. Kiran, D.-W. Cho, H.-K. Lee, C. Y. Kang, and S.-J. Na, “A study on the quality of two-wire tandem submerged arc welds under iso-heat input conditions,” *Int. J. Adv. Manuf. Technol.*, vol. 78, no. 1, pp. 53–62, 2015.
- [68] J. Hu, L.-X. Du, J.-J. Wang, H. Xie, C.-R. Gao, and R. D. K. Misra, “High

- toughness in the intercritically reheated coarse-grained (ICRCG) heat-affected zone (HAZ) of low carbon microalloyed steel,” *Mater. Sci. Eng. A*, vol. 590, pp. 323–328, Jan. 2014.
- [69] Sente Software Ltd., “JMatPro the Materials Property Simulation Package.” United Kingdom.
- [70] D. Li, K. Wu, H. Dong, O. Isayev, and O. Hress, “Coarse grained heat-affected zone microstructure and brittleness of Ti-Nb-B microalloyed high toughness and wear resistant steel,” *Metals (Basel)*, vol. 9, no. 3, 2019.
- [71] S. Machida, H. Yoshinari, and Y. Suzuki, “Statistical study on the effect of local brittle zones (LBZs) on the fracture toughness (crack tip opening displacement) of multipass welded joints,” *ASTM Spec. Tech. Publ.*, no. 1207, pp. 264–290, 1995.
- [72] M. Toyoda, “Crack tip opening displacement (CTOD) testing method for heat-affected zone (HAZ) toughness of steel welds with particular reference to local inhomogeneity,” *ASTM Spec. Tech. Publ.*, no. 1207, pp. 291–307, 1995.
- [73] U. Tosun, “Investigating The Fracture Behaviour of X70m Linepipe Steel Girth Weldments via Single Edge Notched Tension and Bend Tests,” Middle East Technical University, 2018.
- [74] “ASTM E384-17 Standard Test Method for Microindentation Hardness of Materials,” 2017.
- [75] S. Lu, H. Fujii, and K. Nogi, “Marangoni Convection and Gas Tungsten Arc Weld Shape Variations on Pure Iron Plates,” *ISIJ Int.*, vol. 46, no. 2, pp. 276–280, 2006.
- [76] D. P. Fairchild, “Local brittle zones in structural welds,” *Metall. Soc.*, pp. 303–318, 1987.
- [77] S. S. Fukuhisa Matsuda, Yasuto Fukada, Hitoshi Okada, Chiaki Shiga, Kenji Ikeuchi, Yukuhiko Horii, Toyoaki Shiwaku, “Review of mechanical and metallurgical investigations of martensite-austenite constituent in welded joints in Japan,” *Weld. World*, vol. 37, no. 3, pp. 134–154, 1996.
- [78] B. C. Kim, S. Lee, N. J. Kim, and D. Y. Lee, “Microstructure and local brittle zone phenomena in high-strength low-alloy steel welds,” *Metall. Trans. A*, vol. 22, no. 1, pp. 139–149, 1991.
- [79] J. Y. Koo, “Welding Metallurgy of Structural Steels,” *Jom*, vol. 39, no. 6, pp. 31–35, 1987.
- [80] X. J. Di, X. An, F. J. Cheng, D. P. Wang, X. J. Guo, and Z. K. Xue, “Effect of martensite–austenite constituent on toughness of simulated inter-critically reheated coarse-grained heat-affected zone in X70 pipeline steel,” *Sci. Technol.*

*Weld. Join.*, vol. 21, no. 5, pp. 366–373, 2016.

- [81] X. Li, C. Shang, C. Han, Y. Fan, and J. Sun, “Influence of necklace-type M-A constituent on impact toughness and fracture mechanism in the heat affected zone of x100 pipeline steel,” vol. 52, pp. 1025–1035, Sep. 2016.
- [82] P. Mohseni, J. K. Solberg, M. Karlsen, O. M. Akselsen, and E. Østby, “Investigation of mechanism of cleavage fracture initiation in intercritically coarse grained heat affected zone of HSLA steel,” *Mater. Sci. Technol. (United Kingdom)*, vol. 28, no. 11, pp. 1261–1268, 2012.
- [83] X. Li, X. Ma, S. V. Subramanian, C. Shang, and R. D. K. Misra, “Influence of prior austenite grain size on martensite-austenite constituent and toughness in the heat affected zone of 700MPa high strength linepipe steel,” *Mater. Sci. Eng. A*, vol. 616, pp. 141–147, 2014.
- [84] H. Bhadeshia and R. Honeycombe, “Formation of Martensite,” in *Steels: Microstructure and Properties*, Butterworth-Heinemann, 2017, pp. 135–177.
- [85] E. C. Bain and N. Y. Dunkirk, “The Nature of Martensite,” *Trans. AIME*, vol. 70, no. 1, pp. 25–47, 1924.
- [86] X. Li, C. Shang, X. Ma, S. V. Subramanian, R. D. K. Misra, and J. Sun, “Structure and crystallography of martensite–austenite constituent in the intercritically reheated coarse-grained heat affected zone of a high strength pipeline steel,” *Mater. Charact.*, vol. 138, pp. 107–112, Apr. 2018.
- [87] R. Y. Zhang and J. D. Boyd, “Bainite Transformation in Deformed Austenite,” *Metall. Mater. Trans. A*, vol. 41, no. 6, pp. 1448–1459, 2010.
- [88] C. H. Lee, H. K. D. H. Bhadeshia, and H.-C. Lee, “Effect of plastic deformation on the formation of acicular ferrite,” *Mater. Sci. Eng. A*, vol. 360, no. 1–2, pp. 249–257, Nov. 2003.
- [89] H. S. Yang and H. K. D. H. Bhadeshia, “Austenite grain size and the martensite-start temperature,” *Scr. Mater.*, vol. 60, no. 7, pp. 493–495, 2009.
- [90] K. W. Andrews, “Empirical formulae for the calculation of some transformation temperature,” *J. Iron Steel Inst.*, vol. 203, pp. 721–727, 1965.
- [91] H. Ikawa, H. Oshige, and T. Tanoe, “Effect of martensite-austenite constituent on HAZ toughness of high strength steel,” *Trans. Japan Weld. Soc.*, no. 3, pp. 3–12, 1980.
- [92] M. Vladimír, L. Zhonglin, O. Hitoshi, and M. Fukuhisa, “Microstructural Investigations on Decomposition Behaviour of M-A Constituent and Recovery of Ductility due to PWHT in Simulated HAZ of HSLA Steels,” in *Materials, Metallurgy & Weldability*, 1991.
- [93] I. Hrivnak, F. Matsuda, and K. Ikeuchi, “Investigation of M-A Constituent in

- High Strength Steel Welds,” *Trans. JWRI*, vol. 21, no. 2, pp. 149–171.
- [94] G. Erian, “Non-destructive evaluation of residual stresses in the multi-pass steel weldments,” METU.
- [95] J. E. Garcia-Gonzalez, “Fundamental study of the austenite formation and decomposition in low-Si, Al added TRIP steels,” University of Pittsburgh, 2005.
- [96] B. Eghbali and A. Abdollah-Zadeh, “Deformation-induced ferrite transformation in a low carbon Nb–Ti microalloyed steel,” *Mater. Des.*, vol. 28, no. 3, pp. 1021–1026, Jan. 2007.
- [97] A. Lambert-Perlade, T. Sturel, A. F. Gourgues, J. Besson, and A. Pineau, “Mechanisms and modeling of cleavage fracture in simulated heat-affected zone microstructures of a high-strength low alloy steel,” *Metall. Mater. Trans. A*, vol. 35, no. 3, pp. 1039–1053, 2004.
- [98] P. Mohseni, J. Solberg, M. Karlsen, O. Akselsen, and E. Østby, “Cleavage Fracture Initiation at M–A Constituents in Intercritically Coarse-Grained Heat-Affected Zone of a HSLA Steel,” *Metall. Mater. Trans. A*, vol. 45, Jan. 2014.
- [99] L. Lan, C. Qiu, H. Song, and D. Zhao, “Correlation of martensite–austenite constituent and cleavage crack initiation in welding heat affected zone of low carbon bainitic steel,” *Mater. Lett.*, vol. 125, pp. 86–88, Jun. 2014.

